

# Measurements of the Electromagnetic Far-Fields Produced by a Portable Transmitter (Principal Planes)

J.E. Roy, W.R. Lauber, J.M. Bertrand

Electromagnetics and Compatibility Group

CRC-RP-98-002  
Ottawa, February 1998

IC

LKC  
TK  
5102.5  
.C673e02  
#98-002  
c.2

**CRC** Communications  
Research Centre  
Centre de recherches  
sur les communications



Tk  
S102.5  
G673e  
#98-002  
C.b  
S-Gen

MEASUREMENTS OF THE  
ELECTROMAGNETIC FAR-FIELDS  
PRODUCED BY A PORTABLE TRANSMITTER  
(PRINCIPAL PLANES)

CRC REPORT written by:

J.E. Roy  
W.R. Lauber  
J.M. Bertrand



Communications Research Centre  
3701 Carling Ave., P.O. Box 11490, Station H  
Ottawa, Ontario, Canada, K2H 8S2

CRC LIBRARY  
-05-29 1998  
BIBLIOTHEQUE



## Objective

This document presents the procedure for, and the results from, measuring the electromagnetic far-field produced by a portable transmitter in three principal planes ( $\theta = 90^\circ$  or vertical orientation,  $\phi = 0^\circ$  or flat orientation, and  $\phi = 90^\circ$  or edge orientation) for two different arrangements:

1. the transmitter by itself;
2. a styrofoam assembly that held the transmitter near a simulated head. This simulated head consisted of either:
  - (a) free space;
  - (b) a plexiglass box filled with simulated-brain fluid;
  - (c) a plexiglass sphere filled with simulated-brain fluid.

These two different tests were performed in the same chamber but at two different periods. Throughout this document, the "first test" refers to the test for the transmitter by itself, and the "second test" refers to the test for the styrofoam assembly holding the transmitter and a simulated head in a known position and orientation relative to one another. This document presents also the results obtained by comparing the measured data with the predicted data derived by computer simulations from models that were built from the drawings (see Appendix D) for the transmitter, the simulated heads and the styrofoam assembly.

## Acknowledgments

The authors wish to thank Mr. Joe Seregelyi for sharing with us his results on the permittivity measurement of the simulated-brain fluid, and Mr. Claude DesOrmeaux for his expertise in the laboratory.

# Table of Contents

Objective	i
Acknowledgments	ii
Table of Contents	iii
List of Tables	v
List of Figures	vi
Chapter 1. Test Setup	1
1.1 Anechoic chamber setup . . . . .	1
1.2 Equipment setup . . . . .	13
1.3 Mechanical setup . . . . .	17
1.4 Experiment setup . . . . .	36
Chapter 2. Results	41
2.1 Generalities . . . . .	41

2.2 Plots . . . . .	44
2.3 Discussion . . . . .	57
<b>Chapter 3. Comparison Between Predicted and Measured Data</b>	<b>61</b>
3.1 Generalities . . . . .	61
3.2 Plots . . . . .	63
3.3 Discussion . . . . .	82
<b>Chapter 4. Conclusion</b>	<b>83</b>
<b>REFERENCES</b>	<b>84</b>
<b>Appendix A. Gain Measurement of the Receive Horn</b>	<b>85</b>
<b>Appendix B. Transmitter Gain</b>	<b>89</b>
<b>Appendix C. Transformation due to a Change of Origin</b>	<b>91</b>
<b>Appendix D. Drawings</b>	<b>93</b>

## List of Tables

1.1	Mapping between measured and spherical coordinate angular values. .	18
2.1	DC voltages of the battery packs for the first test. . . . .	41
2.2	DC voltages of the battery packs for the second test. . . . .	42
2.3	RF Power level from the oscillator in function of DC supply voltage, for the oscillator working into a 50 Ohm resistive load and starting from a cold state. . . . .	42
2.4	The largest differences in power level between the azimuth angles of $-180^\circ$ and $+180^\circ$ among the two different polarizations for the second test. . . . .	44



## List of Figures

1.1	A view of the setup for the first test, consisting of the azimuth-over-elevation-over-azimuth positioner, the styrofoam pylon, the device under test, the rear wall and the styrofoam wall. . . . .	3
1.2	A view of the setup for the second test, consisting of the azimuth-over-elevation-over-azimuth positioner, the styrofoam pylon, the device under test, the rear wall and the styrofoam wall. . . . .	4
1.3	The reference horn setup for the first test. . . . .	5
1.4	The reference horn setup for the second test. . . . .	6
1.5	The 3' cones hung from the rail for the crane and the partly padded crane. This picture is laid on its side. . . . .	8
1.6	The crane partially padded with absorbing material and the control cables. . . . .	9
1.7	The receive horn mounted in the large horn-like opening in one wall of the chamber for the first test. . . . .	10
1.8	The receive horn mounted in the large horn-like opening in one wall of the chamber for the second test. . . . .	11
1.9	The remotely controlled camera in one corner of the chamber. . . . .	12
1.10	The schematic diagram of the equipment setup. . . . .	14

1.11	A photograph of the equipment setup. . . . .	15
1.12	The spherical coordinate system used for the first test. . . . .	19
1.13	The spherical coordinate system used for the second test. . . . .	20
1.14	The bubble level gauge housing the laser sat on top of the styrofoam block for aligning the styrofoam tower with the phase center of the receive horn. This photograph, however, does not show the white plexiglass washers used to increase the height of the styrofoam block. . . .	21
1.15	The $\theta = 90^\circ$ principal cut for the first test. . . . .	23
1.16	The $\theta = 90^\circ$ principal cut for the second test with the free space head. . . . .	24
1.17	The $\theta = 90^\circ$ principal cut for the second test with the box head. . . . .	25
1.18	The $\theta = 90^\circ$ principal cut for the second test with the sphere head. . . . .	26
1.19	The $\phi = 0^\circ$ principal cut for the first test. . . . .	27
1.20	The $\phi = 0^\circ$ principal cut for the second test with the free space head. . . . .	28
1.21	The $\phi = 0^\circ$ principal cut for the second test with the box head. . . . .	29
1.22	The $\phi = 0^\circ$ principal cut for the second test with the sphere head. . . . .	30
1.23	The $\phi = 90^\circ$ principal cut for the first test. . . . .	31
1.24	The $\phi = 90^\circ$ principal cut for the second test with the free space head. . . . .	32
1.25	The $\phi = 90^\circ$ principal cut for the second test with the box head. . . . .	33
1.26	The $\phi = 90^\circ$ principal cut for the second test with the sphere head. . . . .	34
1.27	The styrofoam disk with the four additional circular holes machined out of its upper surface for the second test. . . . .	35
1.28	The sphere head filled with simulated-brain fluid. . . . .	38

1.29	The box head filled with simulated-brain fluid. . . . .	39
2.1	The magnitude of the horizontal polarization signals for the $\theta = 90^\circ$ orientation in the first and second (free space head) tests, respectively. . . . .	45
2.2	The magnitude of the vertical polarization signals for the $\theta = 90^\circ$ orientation in the first and second (free space head) tests, respectively. . . . .	46
2.3	The magnitude of the horizontal polarization signals for the $\phi = 0^\circ$ orientation in the first and second (free space head) tests, respectively. . . . .	47
2.4	The magnitude of the vertical polarization signals for the $\phi = 0^\circ$ orientation in the first and second (free space head) tests, respectively. . . . .	48
2.5	The magnitude of the horizontal polarization signals for the $\phi = 90^\circ$ orientation in the first and second (free space head) tests, respectively. . . . .	49
2.6	The magnitude of the vertical polarization signals for the $\phi = 90^\circ$ orientation in the first and second (free space head) tests, respectively. . . . .	50
2.7	The magnitude of the horizontal polarization signals for the $\theta = 90^\circ$ orientation in the second test with the free space, the box and the sphere heads. . . . .	51
2.8	The magnitude of the vertical polarization signals for the $\theta = 90^\circ$ orientation in the second test with the free space, the box and the sphere heads. . . . .	52
2.9	The magnitude of the horizontal polarization signals for the $\phi = 0^\circ$ orientation in the second test with the free space, the box and the sphere heads. . . . .	53
2.10	The magnitude of the vertical polarization signals for the $\phi = 0^\circ$ orientation in the second test with the free space, the box and the sphere heads. . . . .	54

2.11	The magnitude of the horizontal polarization signals for the $\phi = 90^\circ$ orientation in the second test with the free space, the box and the sphere heads. . . . .	55
2.12	The magnitude of the vertical polarization signals for the $\phi = 90^\circ$ orientation in the second test with the free space, the box and the sphere heads. . . . .	56
3.1	Comparison between the magnitudes of the predicted and measured horizontal polarization for the $\theta = 90^\circ$ orientation of the first test. . .	64
3.2	Comparison between the magnitudes of the predicted and measured vertical polarization for the $\theta = 90^\circ$ orientation of the first test. . . .	65
3.3	Comparison between the magnitudes of the predicted and measured horizontal polarization for the $\phi = 0^\circ$ orientation of the first test. . .	66
3.4	Comparison between the magnitudes of the predicted and measured vertical polarization for the $\phi = 0^\circ$ orientation of the first test. . . . .	67
3.5	Comparison between the magnitudes of the predicted and measured horizontal polarization for the $\phi = 90^\circ$ orientation of the first test. . .	68
3.6	Comparison between the magnitudes of the predicted and measured vertical polarization for the $\phi = 90^\circ$ orientation of the first test. . . .	69
3.7	Comparison between the magnitudes of the predicted and measured horizontal polarization for the $\theta = 90^\circ$ orientation of the second test with the box head. . . . .	70
3.8	Comparison between the magnitudes of the predicted and measured vertical polarization for the $\theta = 90^\circ$ orientation of the second test with the box head. . . . .	71
3.9	Comparison between the magnitudes of the predicted and measured horizontal polarization for the $\phi = 0^\circ$ orientation of the second test with the box head. . . . .	72

3.10 Comparison between the magnitudes of the predicted and measured vertical polarization for the $\phi = 0^\circ$ orientation of the second test with the box head. . . . .	73
3.11 Comparison between the magnitudes of the predicted and measured horizontal polarization for the $\phi = 90^\circ$ orientation of the second test with the box head. . . . .	74
3.12 Comparison between the magnitudes of the predicted and measured vertical polarization for the $\phi = 90^\circ$ orientation of the second test with the box head. . . . .	75
3.13 Comparison between the magnitudes of the predicted and measured horizontal polarization for the $\theta = 90^\circ$ orientation of the second test with the sphere head. . . . .	76
3.14 Comparison between the magnitudes of the predicted and measured vertical polarization for the $\theta = 90^\circ$ orientation of the second test with the sphere head. . . . .	77
3.15 Comparison between the magnitudes of the predicted and measured horizontal polarization for the $\phi = 0^\circ$ orientation of the second test with the sphere head. . . . .	78
3.16 Comparison between the magnitudes of the predicted and measured vertical polarization for the $\phi = 0^\circ$ orientation of the second test with the sphere head. . . . .	79
3.17 Comparison between the magnitudes of the predicted and measured horizontal polarization for the $\phi = 90^\circ$ orientation of the second test with the sphere head. . . . .	80
3.18 Comparison between the magnitudes of the predicted and measured vertical polarization for the $\phi = 90^\circ$ orientation of the second test with the sphere head. . . . .	81

A.1 The schematic diagram of the equipment setup for measuring the gain of the receive horn. . . . .	86
---	----

# Chapter 1

## Test Setup

This section presents the details about the anechoic chamber setup, the equipment setup, the mechanical setup and the experiment setup.

### 1.1 Anechoic chamber setup

The measurements took place in the  $6.1m \times 6.7m \times 6.1m$  David Florida Laboratory (DFL) anechoic chamber. This chamber is a shielded room that has its four walls and the ceiling covered permanently with absorbing cones (18" cones on the wall facing the receive horn, 9" cones on the ceiling and on the three walls). The fourth wall has an  $18' \times 18'$  electromagnetic window made of 1' thick white styrofoam panels dovetailed together without the use of adhesives. A metallic rolling door can be lowered to protect the styrofoam wall against high wind loads from the outside. This sliding door was fully raised for all tests mentioned herein, thus leaving the chamber opened, in effect, to free space through the styrofoam wall. Unfortunately, the performance of this chamber has not been systematically characterized for that frequency (850 MHz) and that configuration, and thus, the size, location and quality of the quiet zone was not known. Since the efficiency of the absorbing material is not large at 850 MHz, some reflections should be expected from the metallic walls of the shielded room even though they were covered with absorbing material. The information found in Reference [1, p. 28] states that the quiet zone of the chamber is located at the centre



of the chamber and has a maximum amplitude taper of 0.5 dB over an aperture of 31.0" at 1.5 GHz.

At the center of the chamber was an azimuth-over-elevation-over-azimuth positioner, Scientific Atlanta model 5524-7, (see Figure 1.1 and 1.2). Note, however, that the lowermost azimuth axis remained fixed for all tests mentioned herein. The floor was covered with a combination of various sizes of removable absorbing cones (4' and 3' cones in front of the positioner, 2' cones around the positioner, and 9" cones everywhere else).

A 0.95-1.15 GHz waveguide transition acting as a reference signal pick-up horn was located directly on the upper azimuth table of the positioner so that the reference horn would rotate in the azimuth plane along with the transmitter. The reference horn was thus located about 2 m vertically down from the transmitter and pointing vertically toward the ceiling. It was found that the reference horn did not need to be positioned at  $45^\circ$  for the purpose of picking up a reference signal regardless of whether the transmitter was in the vertical or horizontal orientations. The reference horn was also surrounded with absorbing material in order to couple mostly the direct wave from the transmitter to the reference horn. In the first test, the reference horn was surrounded with three walls of absorbing material, the fourth wall being the styrofoam pylon on top of which sat the transmitter (see photograph 1.3). In the second test, the reference horn was surrounded with four walls of absorbing material (see photograph 1.4).

In order to minimize possible scatterers, one obsolete camera bracket was removed from the wall facing the receive horn, four pieces of 3' cones were hung from the metallic sliding monorail used for holding a crane that hangs from the ceiling (see Figure 1.5), and this crane was retracted as far to the side as possible and was partly padded with absorbing material (see Figure 1.6). The control cables for this crane, however, could not be padded but these cables were located far enough to the side of the chamber so as to lie outside the main beam of the receive horn ( $\pm 60^\circ$ ). The four pieces of 3' thick absorbing material hung from the rail on the ceiling were used to minimize the amplitude variations incurred with the reference signal when the azimuth table was rotated since the metallic rail then appeared, in effect, to be swept



Figure 1.1: A view of the setup for the first test, consisting of the azimuth-over-elevation-over-azimuth positioner, the styrofoam pylon, the device under test, the rear wall and the styrofoam wall.





Figure 1.2: A view of the setup for the second test, consisting of the azimuth-over-elevation-over-azimuth positioner, the styrofoam pylon, the device under test, the rear wall and the styrofoam wall.



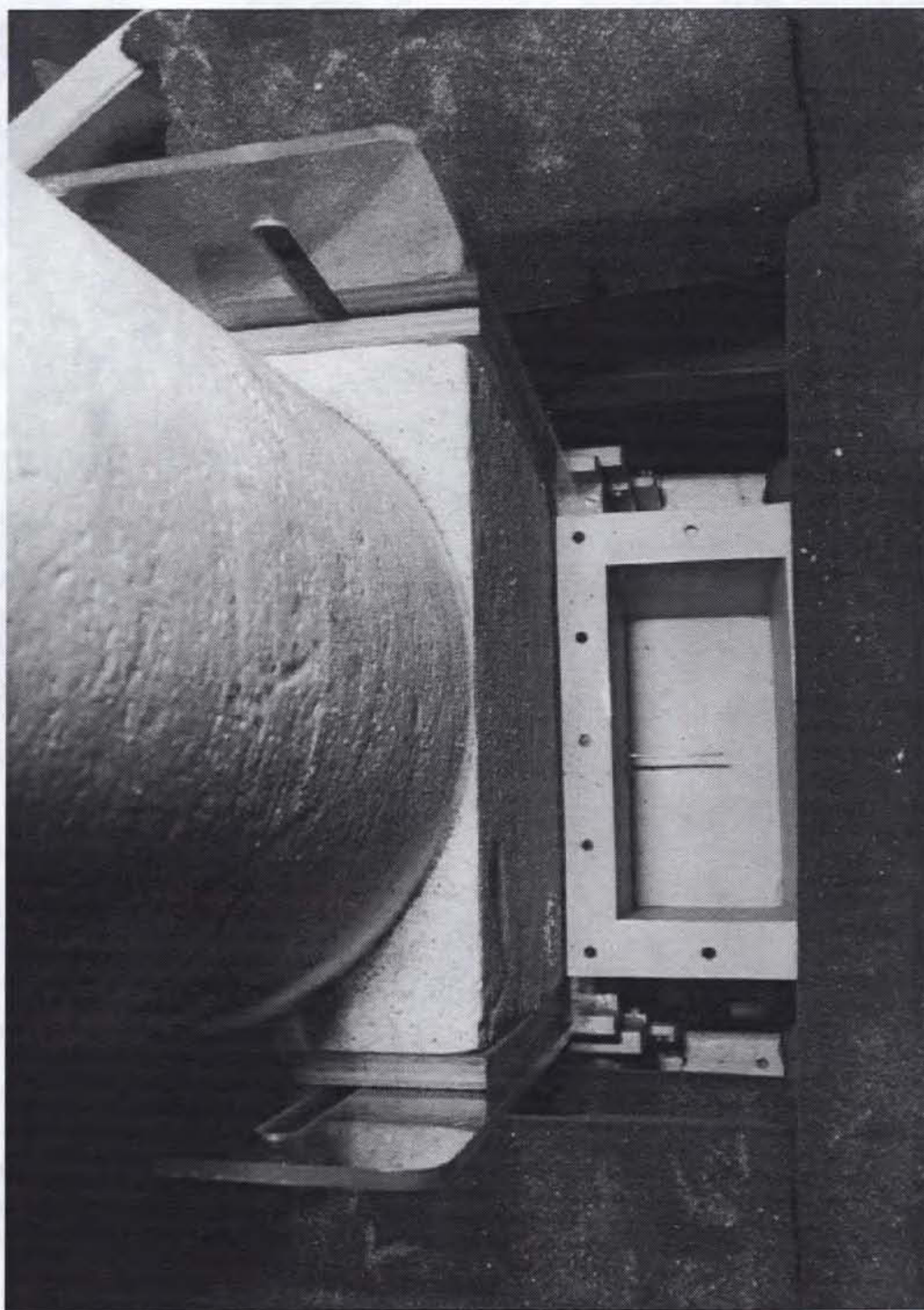


Figure 1.3: The reference horn setup for the first test.

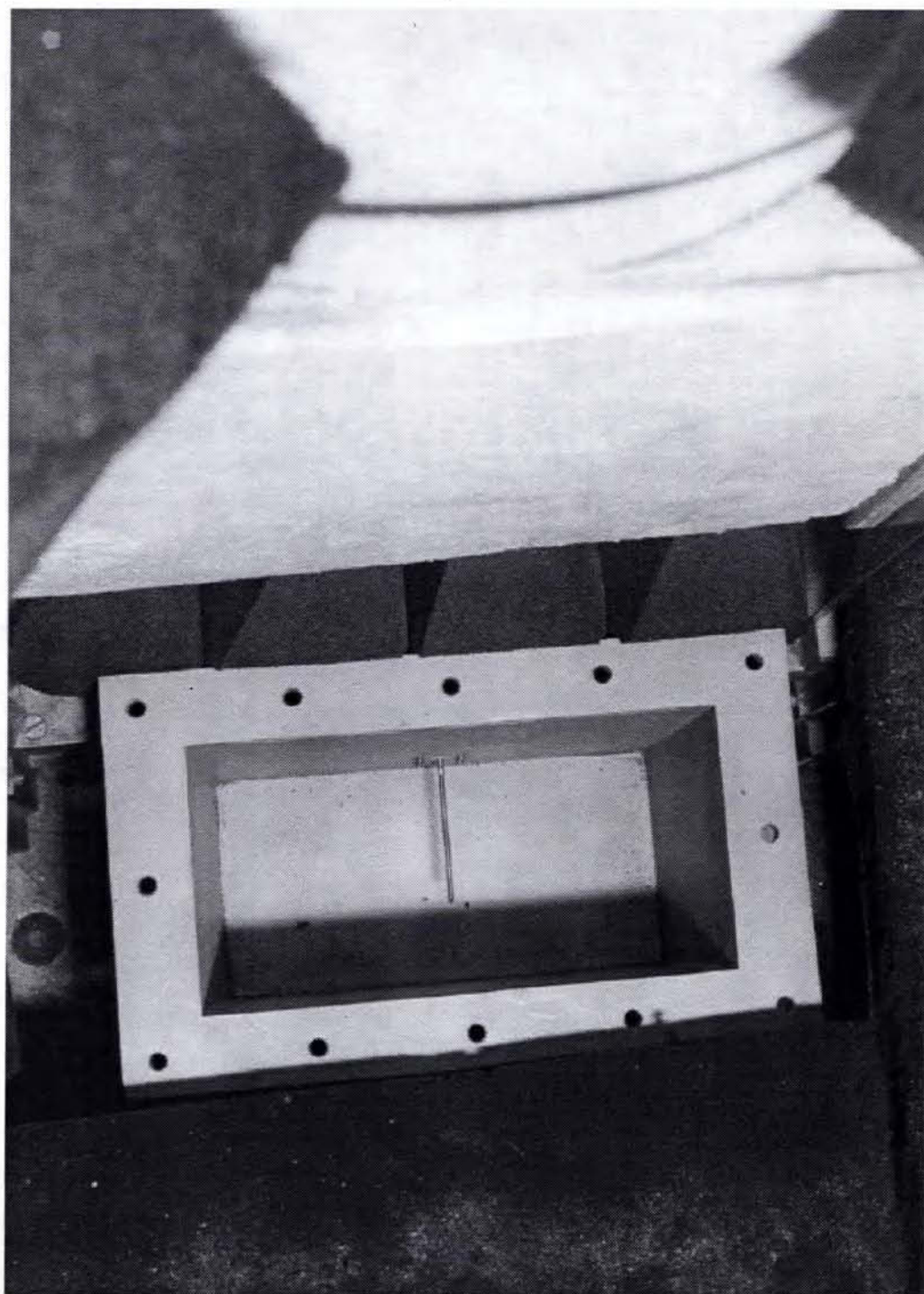


Figure 1.4: The reference horn setup for the second test.



across the radiation beam of the reference horn as the azimuth table was rotated.

Another horn, the receive horn, was positioned in the aperture of a large  $6' \times 6'$  pyramidal extension protruding from one wall of the chamber (see Figure 1.7 and 1.8). The walls of this large horn were lined with flat sheets of absorbing material Emerson and Cuming AN-75 and the remaining area of the aperture was loaded with pieces of absorbing material so as to leave free only the aperture of the smaller receive horn. The pieces of absorbing material, however, were positioned around the receive horn in recess with respect to the aperture of the receive horn in order to avoid disturbing the performance of the receive horn.

Another camera (see Figure 1.9) was mounted in the corner opposite from the one where the obsolete bracket was removed. This remotely controlled camera was not covered with absorbing material because it laid completely outside the field of view of the receive horn.



Figure 1.5: The 3' cones hung from the rail for the crane and the partly padded crane. This picture is laid on its side.



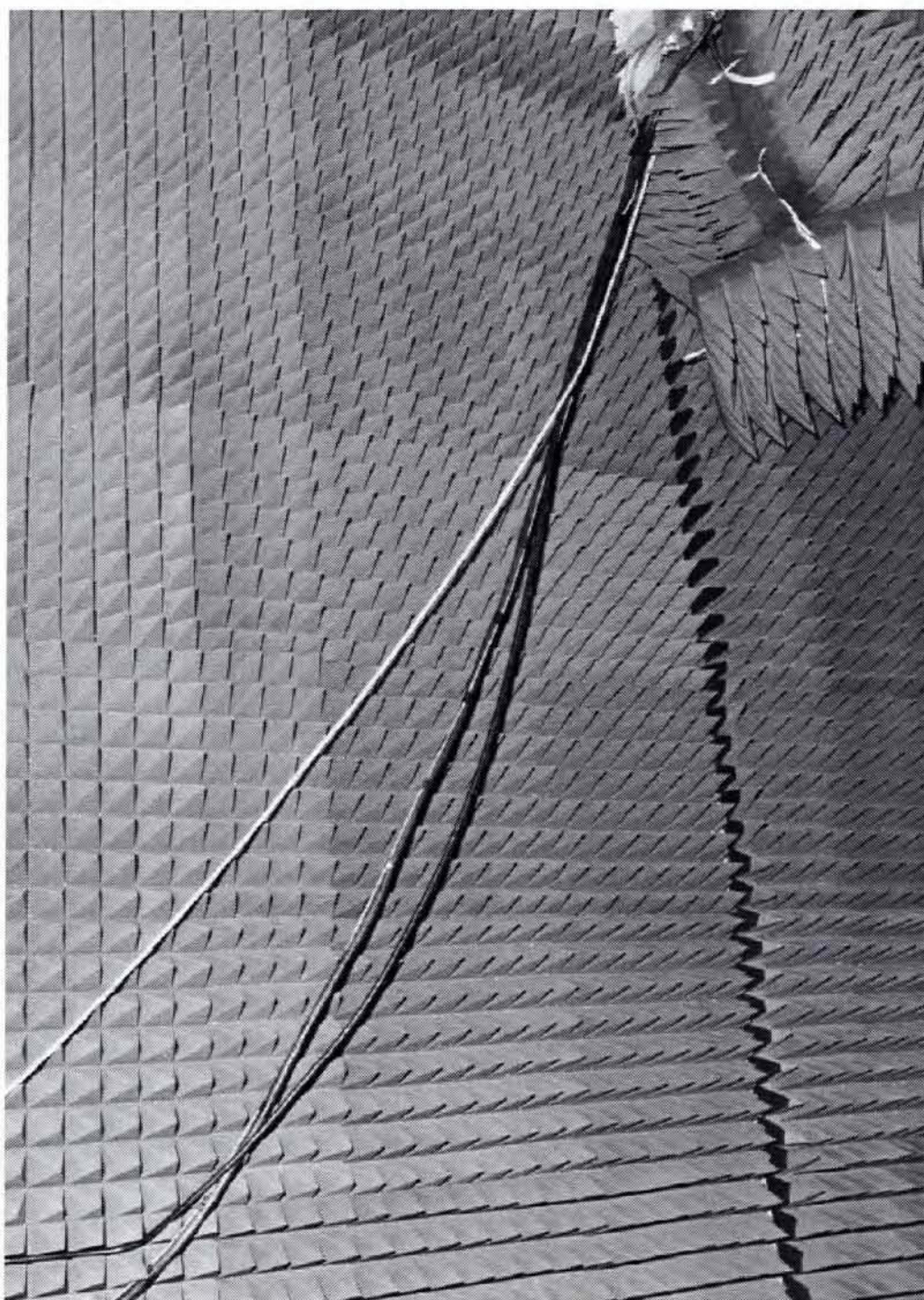


Figure 1.6: The crane partially padded with absorbing material and the control cables.



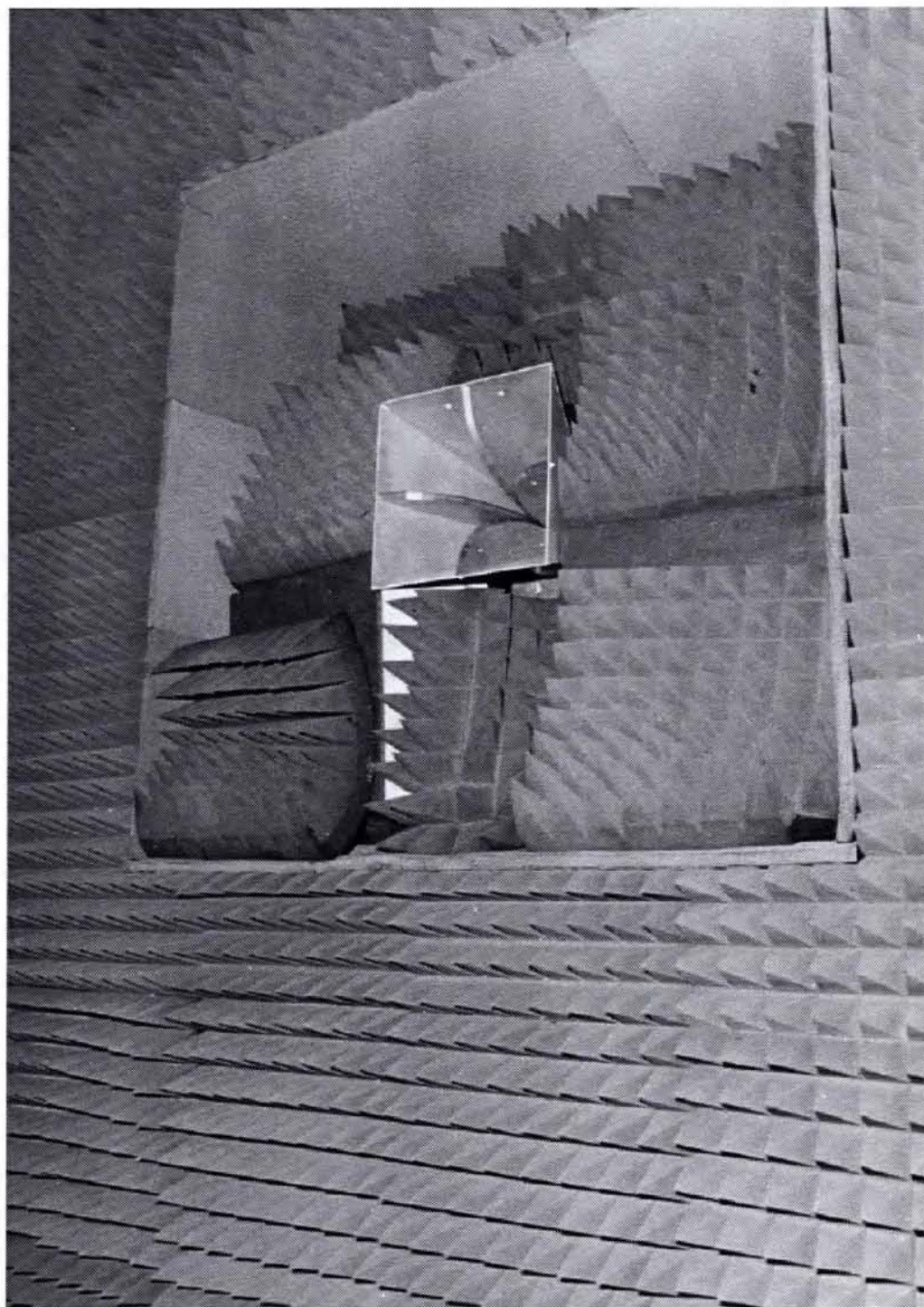


Figure 1.7: The receive horn mounted in the large horn-like opening in one wall of the chamber for the first test.



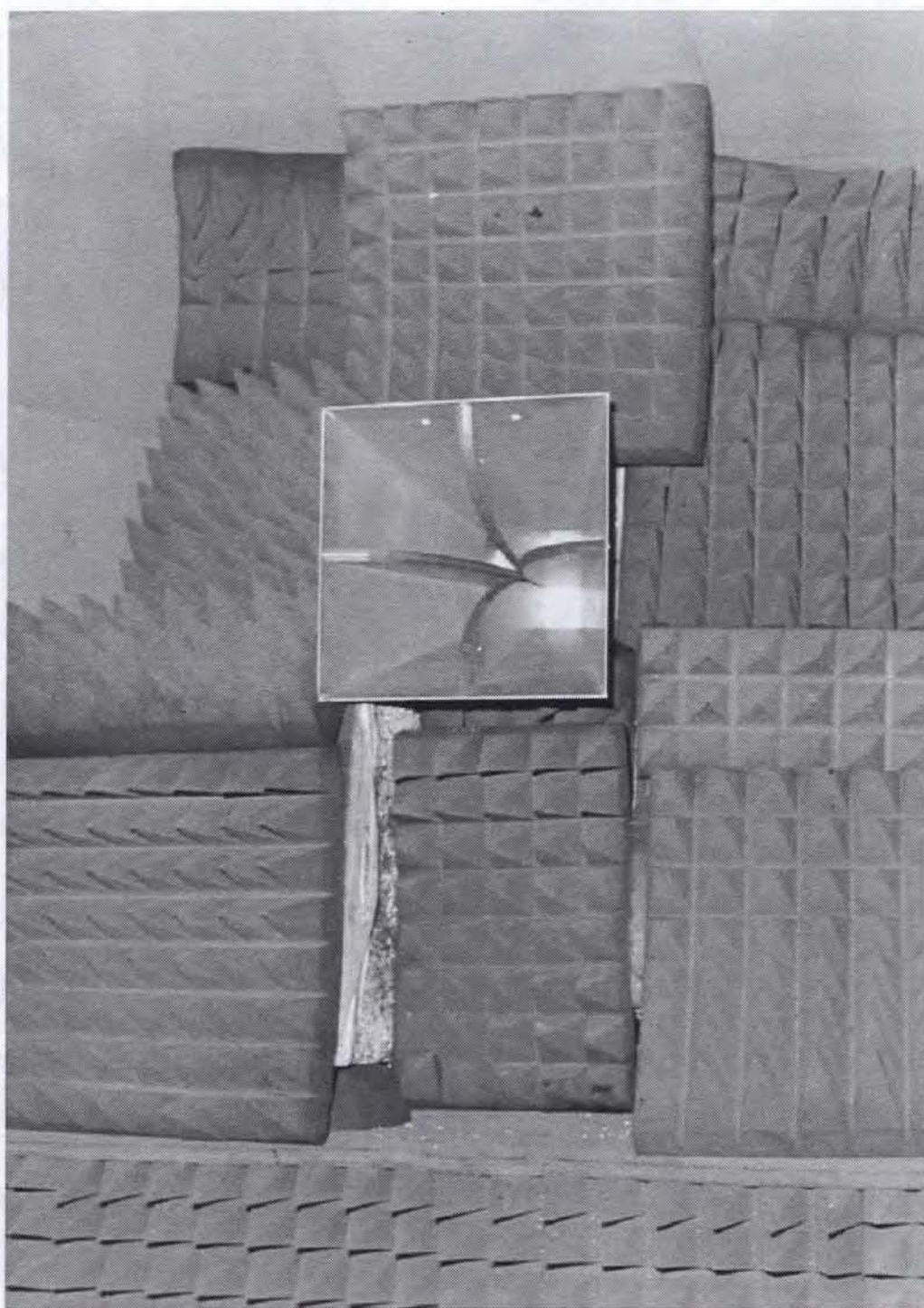


Figure 1.8: The receive horn mounted in the large horn-like opening in one wall of the chamber for the second test.





Figure 1.9: The remotely controlled camera in one corner of the chamber.

## 1.2 Equipment setup

The setup of the equipment is shown in Figures 1.10 and 1.11.

The Device Under Test (D.U.T.) corresponded to the transmitter alone in the first test, or to the transmitter with a simulated head in the second test. Technical specifications for the transmitter can be found in Reference [2].

The receive horn was a dual polarization quad-ridged horn (Condor Systems, AS-48450) with a measured gain of 9.05 dB for the vertical polarization (see Appendix A). Although not measured, the gain for the horizontal polarization can be assumed to be equal to that for the vertical polarization since the horn geometry has a four-fold rotational symmetry.

The vertically and the horizontally polarized signals obtained from the quad-ridged horn were fed to a network analyzer (HP8530A) which had a very narrow effective bandwidth from synchronous demodulation. A waveguide launcher acting as the reference horn was installed on the azimuth table and pointed upward in order to obtain a reference signal on which to phase-lock the vertically and horizontally polarized signals in order for the network analyzer to track the frequency drift of the oscillator in the transmitter.

The signal from the reference horn was connected to a 850 MHz filter (K&L Microwave, 3BT-500/1000-SN C691-1) followed by a 20 dB coupler (HP778D terminated with an external 50 Ohm load) then a 26 dB RF amplifier (HP8447D) and finally the reference port of the network analyzer (HP8530A). The coupled port of the coupler was connected to a spectrum analyzer (HP8560E). The signal level at the reference port of the network analyzer ranged from -14 dBm to -9 dBm for the first test and from -24 dBm to -16 dBm for the second test. The network analyzer operates most accurately with the power level of the phase-locking signal being between -10 dBm and -50 dBm. No 850 MHz filter was needed in the path of the vertically or the horizontally polarized signals because of the very narrow bandwidth of the HP8530A network analyzer. The 10 MHz reference signal from the spectrum analyzer was used to synchronize the 10 MHz clock of the HP8530A network analyzer via the HP83623B

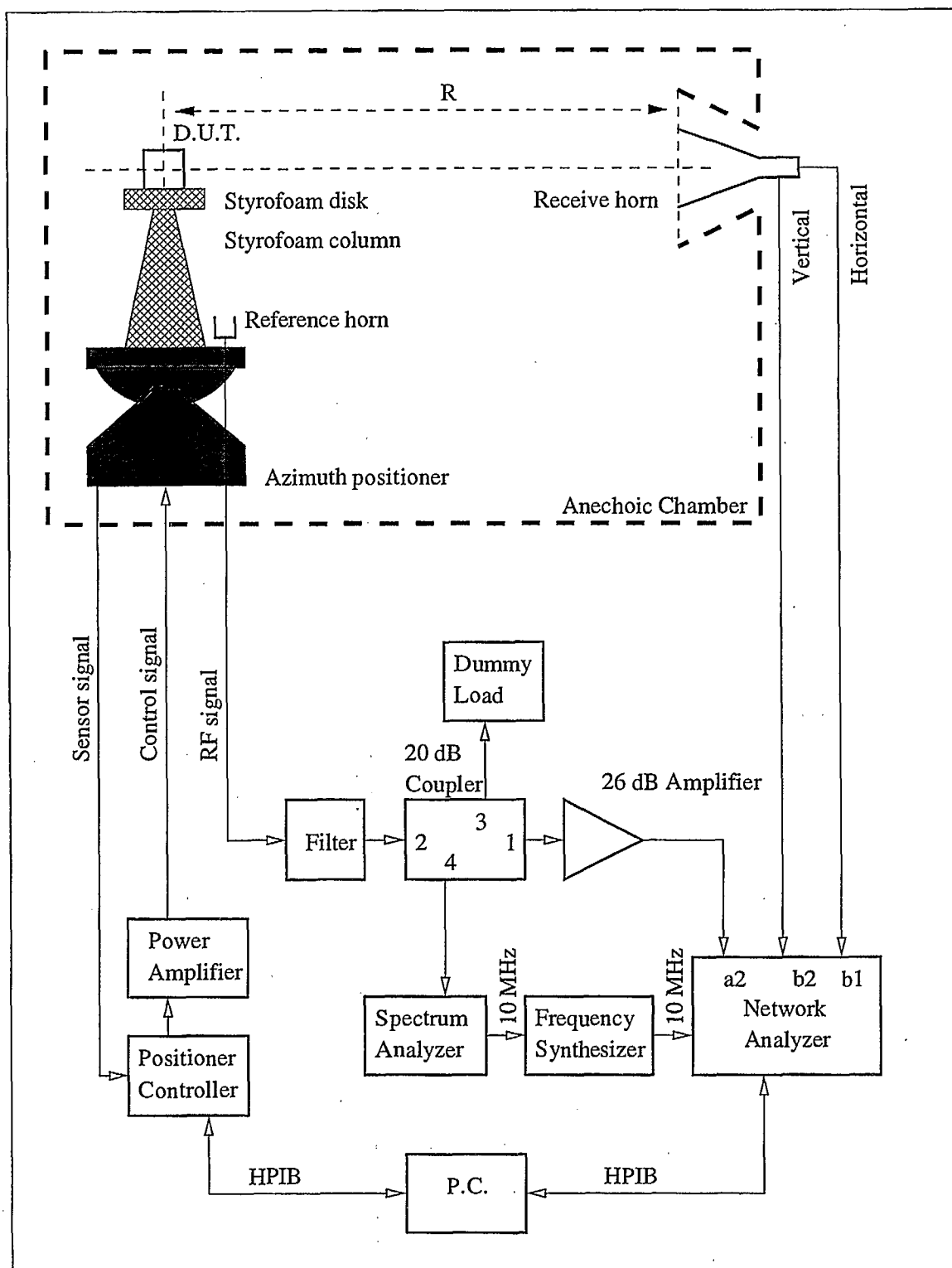


Figure 1.10: The schematic diagram of the equipment setup.



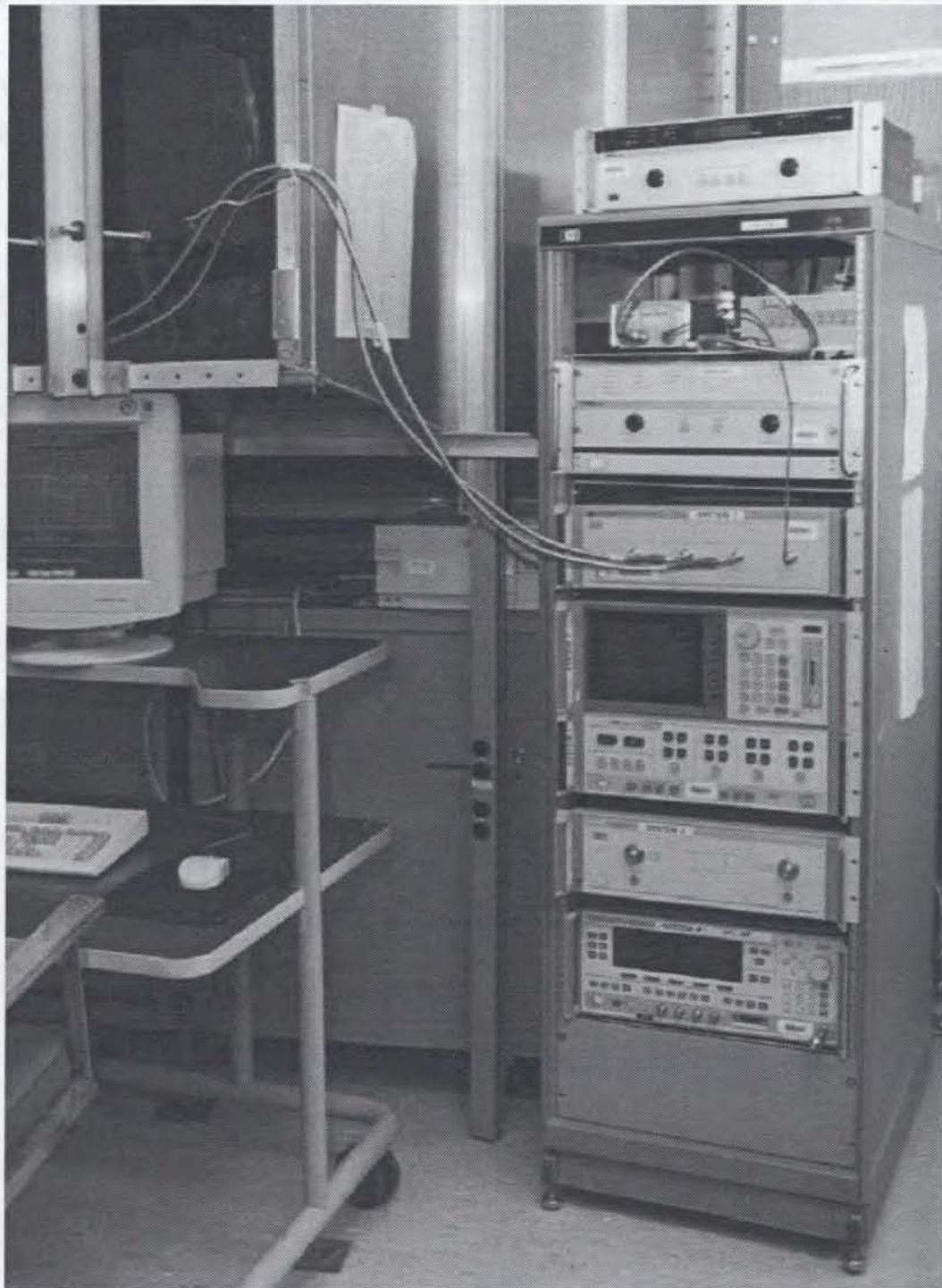


Figure 1.11: A photograph of the equipment setup.



frequency synthesizer (the reason for using the frequency synthesizer was simply that this piece of equipment was already connected to the HP8530A, and had a very good frequency stability). The 20 dB coupler and the spectrum analyzer were passed their respective calibration date but this situation was not deemed to be critical, owing to the passive nature of the coupler and to the secondary importance of the spectrum analyzer.

The positioner was controlled by a Flam & Russel 8502 positioner programmer controller and a Flam & Russel 8601A power amplifier. Although the resolution of the numerical display on the controller was  $0.001^\circ$ , the mechanical resolution of the positioner was about  $0.007^\circ$  (see Reference [1, p. 2]).

### 1.3 Mechanical setup

The far field radiation patterns in both the horizontal and the vertical (with respect to the chamber) polarizations were taken with the transmitter being in either one of three orientations:

1. the vertical orientation, corresponding to the  $\theta = 90^\circ$  principal cut (see photographs 1.15, 1.16, 1.17, 1.18);
2. the broad flat side orientation, corresponding to the  $\phi = \{0^\circ, 180^\circ\}$  principal cut (see photographs 1.19, 1.20, 1.21, 1.22);
3. the edge side orientation, corresponding to the  $\phi = \{90^\circ, 270^\circ\}$  principal cut (see photographs 1.23, 1.24, 1.25, 1.26);

where the angles  $\theta$  and  $\phi$  were the angles for the spherical coordinate systems in Figures 1.12 and 1.13. These coordinate systems are used herein only to describe the angular cuts. The measurement angle was related to these spherical coordinate angles as described here and as summarized in Table 1.1. The tower was operated in azimuth from  $-180^\circ$  to  $+180^\circ$ , with  $-90^\circ$  corresponding to the D.U.T. facing the styrofoam wall. For the  $\theta = 90^\circ$  cut, the measurement angle ranging from  $-180^\circ$  to  $0^\circ$  corresponded to  $\phi$  varying from  $+90^\circ$  to  $+270^\circ$ , and the measurement angle ranging from  $0^\circ$  to  $+180^\circ$  corresponded to  $\phi$  varying from  $+270^\circ$  to  $+90^\circ$ . For the  $\phi = \{0^\circ, 180^\circ\}$  cut, the measurement angle ranging from  $-180^\circ$  to  $0^\circ$  corresponded to  $\theta$  varying from  $180^\circ$  to  $0^\circ$  of the  $\phi = 180^\circ$  cut, and the measurement angle ranging from  $0^\circ$  to  $+180^\circ$  corresponded to  $\theta$  varying from  $0^\circ$  to  $180^\circ$  of the  $\phi = 0^\circ$  cut. For the  $\phi = \{90^\circ, 270^\circ\}$  cut, the measurement angle ranging from  $-180^\circ$  to  $0^\circ$  corresponded to  $\theta$  varying from  $180^\circ$  to  $0^\circ$  of the  $\phi = 270^\circ$  cut, and the measurement angle ranging from  $0^\circ$  to  $+180^\circ$  corresponded to  $\theta$  varying from  $0^\circ$  to  $180^\circ$  of the  $\phi = 90^\circ$  cut. In order to ease the writing process, however, the  $\phi = \{0^\circ, 180^\circ\}$  and the  $\phi = \{90^\circ, 270^\circ\}$  cuts will be referred to more simply from here on end as the  $\phi = 0^\circ$  and the  $\phi = 90^\circ$  cuts, respectively, with the tacit understanding of the above. The origin of the coordinate system was shifted from the base of the monopole antenna in the first test to the center of the styrofoam assembly in the second test in order for the origin to remain

Table 1.1: Mapping between measured and spherical coordinate angular values.

Cut	Measurement Angle ( $^{\circ}$ )	Spherical Coordinate Angle ( $^{\circ}$ )
$\theta = 90^{\circ}$	$-180 \rightarrow 0$ $0 \rightarrow +180$	$\phi = +90 \rightarrow +270$ $\phi = +270 \rightarrow +90$
$\phi = \{0^{\circ}, 180^{\circ}\}$	$-180 \rightarrow 0$ $0 \rightarrow +180$	$\theta = 180 \rightarrow 0$ ..... of the $\phi = 180^{\circ}$ cut $\theta = 0 \rightarrow 180$ ..... of the $\phi = 0^{\circ}$ cut
$\phi = \{90^{\circ}, 270^{\circ}\}$	$-180 \rightarrow 0$ $0 \rightarrow +180$	$\theta = 180 \rightarrow 0$ ..... of the $\phi = 270^{\circ}$ cut $\theta = 0 \rightarrow 180$ ..... of the $\phi = 90^{\circ}$ cut

in the same point in space as the styrofoam assembly was positioned in either one of the three orientations. In the presence of the box and sphere heads, the transmitter was obstructed in the range of measurement angle values about  $0^{\circ}$  for the vertical orientation, and about  $-90^{\circ}$  for the edge orientation. No significant obstruction was ever incurred for the flat orientation.

The styrofoam pylon consisted of a styrofoam column on top of which a styrofoam disk was mated. The disk was positioned with a bubble level gauge and the styrofoam pylon was aligned with a laser beam such that the base of the monopole antenna in the first test, or the center of the styrofoam assembly in the second test, laid at the height of the phase center of the horn and on the axis of rotation of the azimuth table. The laser was integrated as part of a bubble level gauge. This gauge sat on a styrofoam block the thickness of which was augmented with one layer of plexiglass washers. These washers sat on the styrofoam disk (see Figure 1.14), leaving a gap between the two styrofoam pieces.

The distance between the azimuthal axis of rotation and the aperture of the receive horn was 334.6 cm (or 131.75") for the first test and 331.5 cm (or 130.5") for the second test (these two tests were not performed in the same period and the chamber had to be reconfigured for the use of an external customer between these two tests; the difference owed to having repositioned the receive horn in the horn-like opening of the wall). The proper vertical and horizontal orientations of the transmitter were checked by means of a bubble level gauge.

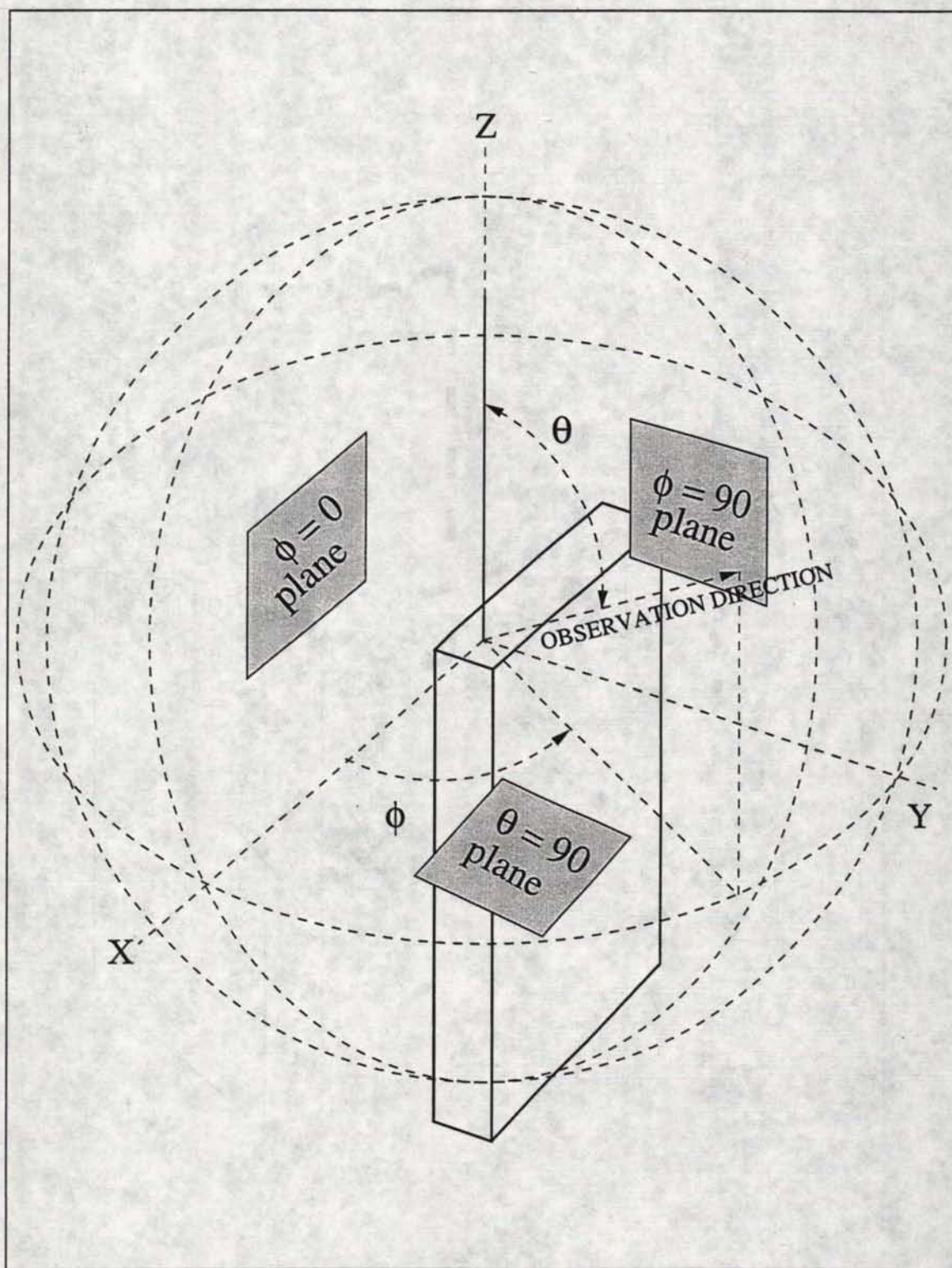


Figure 1.12: The spherical coordinate system used for the first test.



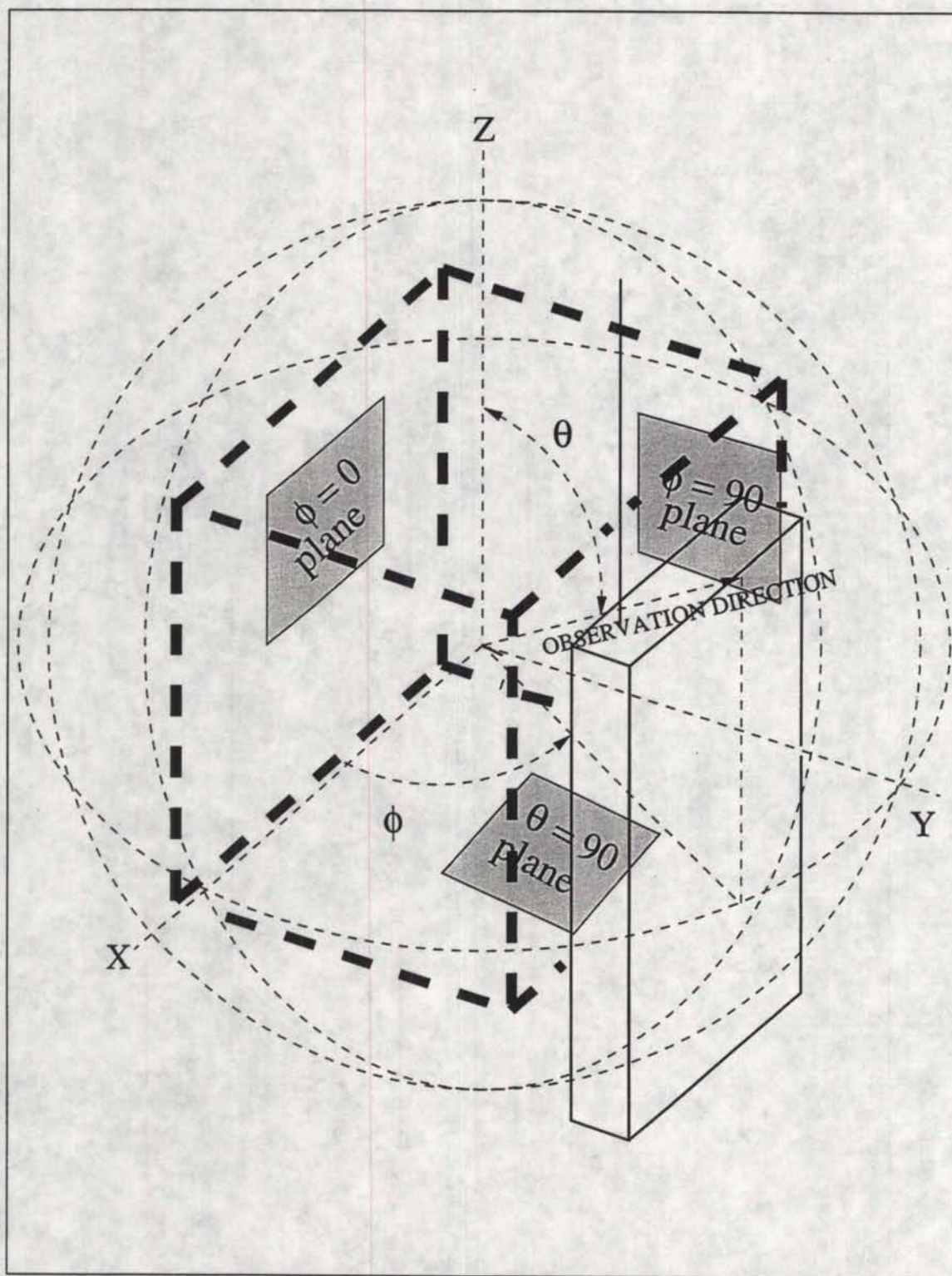


Figure 1.13: The spherical coordinate system used for the second test.

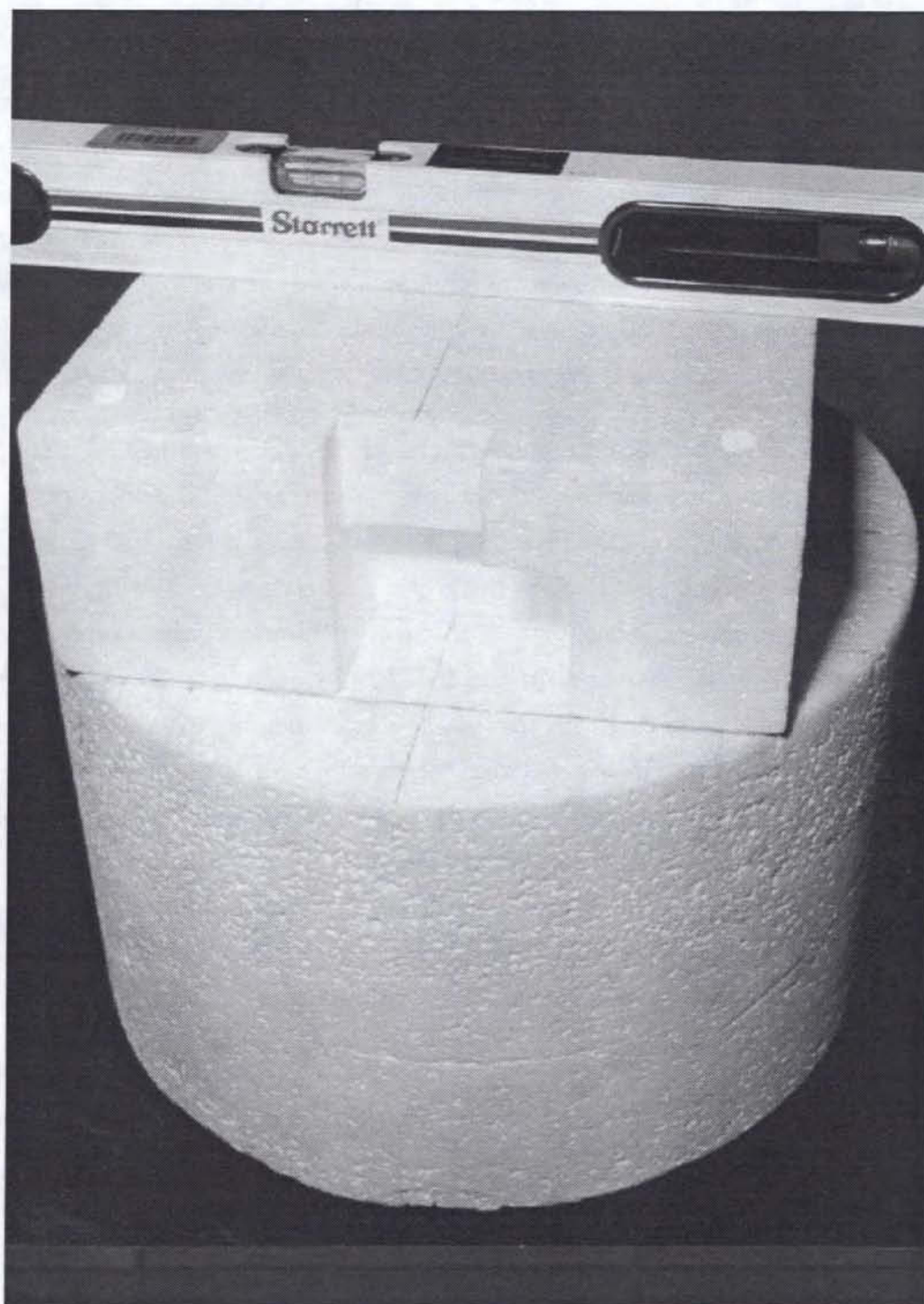


Figure 1.14: The bubble level gauge housing the laser sat on top of the styrofoam block for aligning the styrofoam tower with the phase center of the receive horn. This photograph, however, does not show the white plexiglass washers used to increase the height of the styrofoam block.



In the first test, the three orientations were held fixed by means of slots in styrofoam blocks of such conception as to maintain the base of the monopole antenna of the transmitter at the same location in the chamber, regardless of the orientation of the transmitter (see photographs and drawings). In contrast, for the second test, the three orientations were set by manually positioning the styrofoam assembly on top of the styrofoam disk. Consequently, the accuracy in aligning the zero azimuthal angle of the styrofoam assembly was estimated to be no better than about  $0.6^\circ$ .

Although shown on some photographs, the rubber band holding the transmitter in place when facing down was never used because herein, the transmitter was never positioned such as to be facing down. For the case of the simulated head being the sphere, the spacing provided by two white plexiglass washers was used for the test with the transmitter being in the vertical orientation in order to have the center of the assembly at the same position in the chamber, owing to the height of the sphere assembly being different from that for the box assembly. Consequently, an air gap (see Figure 1.18) was present between the styrofoam disk and the styrofoam assembly. Moreover, owing to the construction of the sphere assembly, the spacing between the top and bottom styrofoam pieces holding the sphere could vary depending on how much the four nuts holding together the assembly could be tightened. This spacing was adjusted to  $\approx 4.5$  cm (or  $1\frac{25}{32}$  inches). For the second test (but not so for the first test), the styrofoam disk had four holes machined out of its upper surface (see Figure 1.27) in order to make room for the nuts of the styrofoam assembly when the transmitter was in the vertical position.

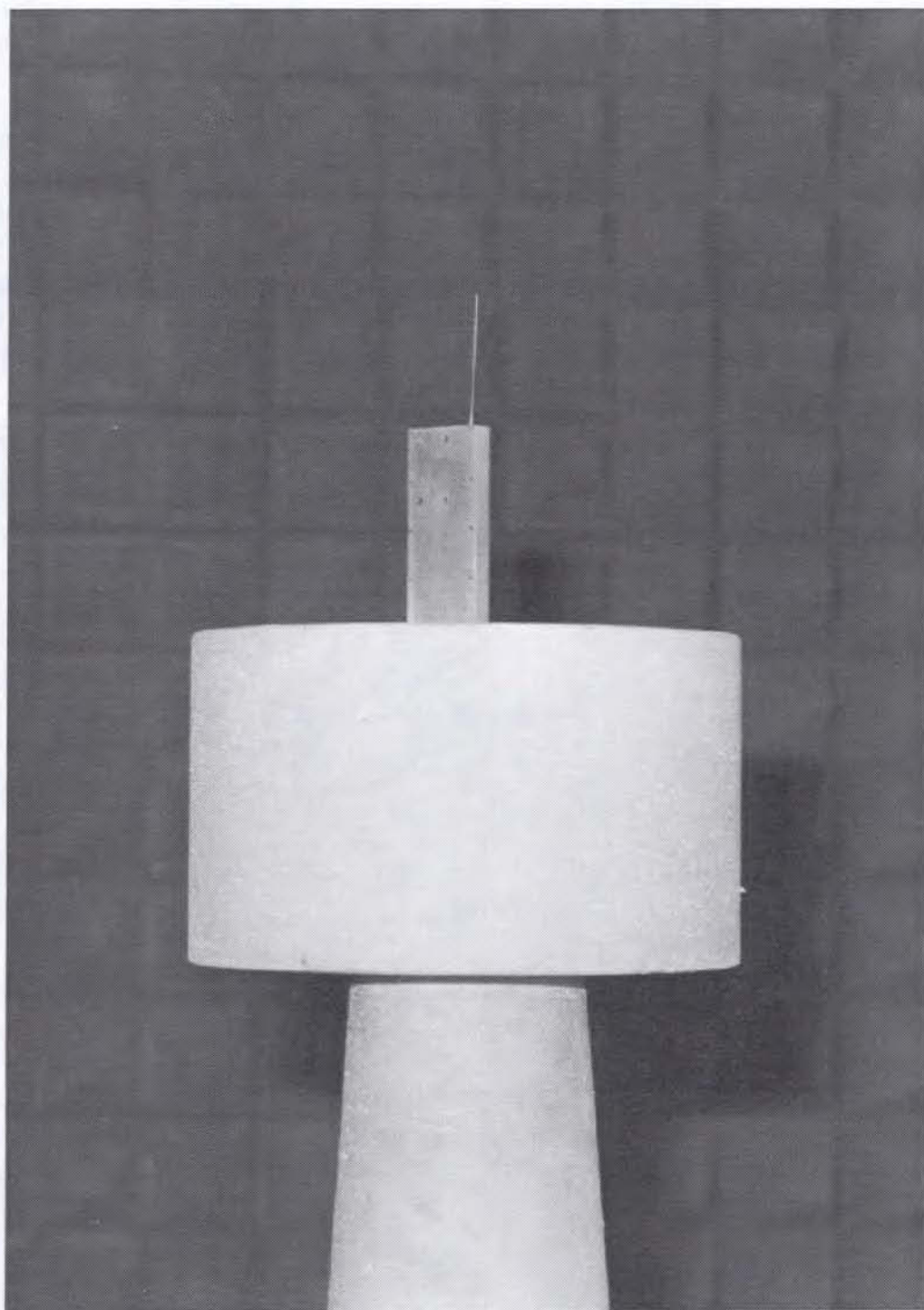


Figure 1.15: The  $\theta = 90^\circ$  principal cut for the first test.



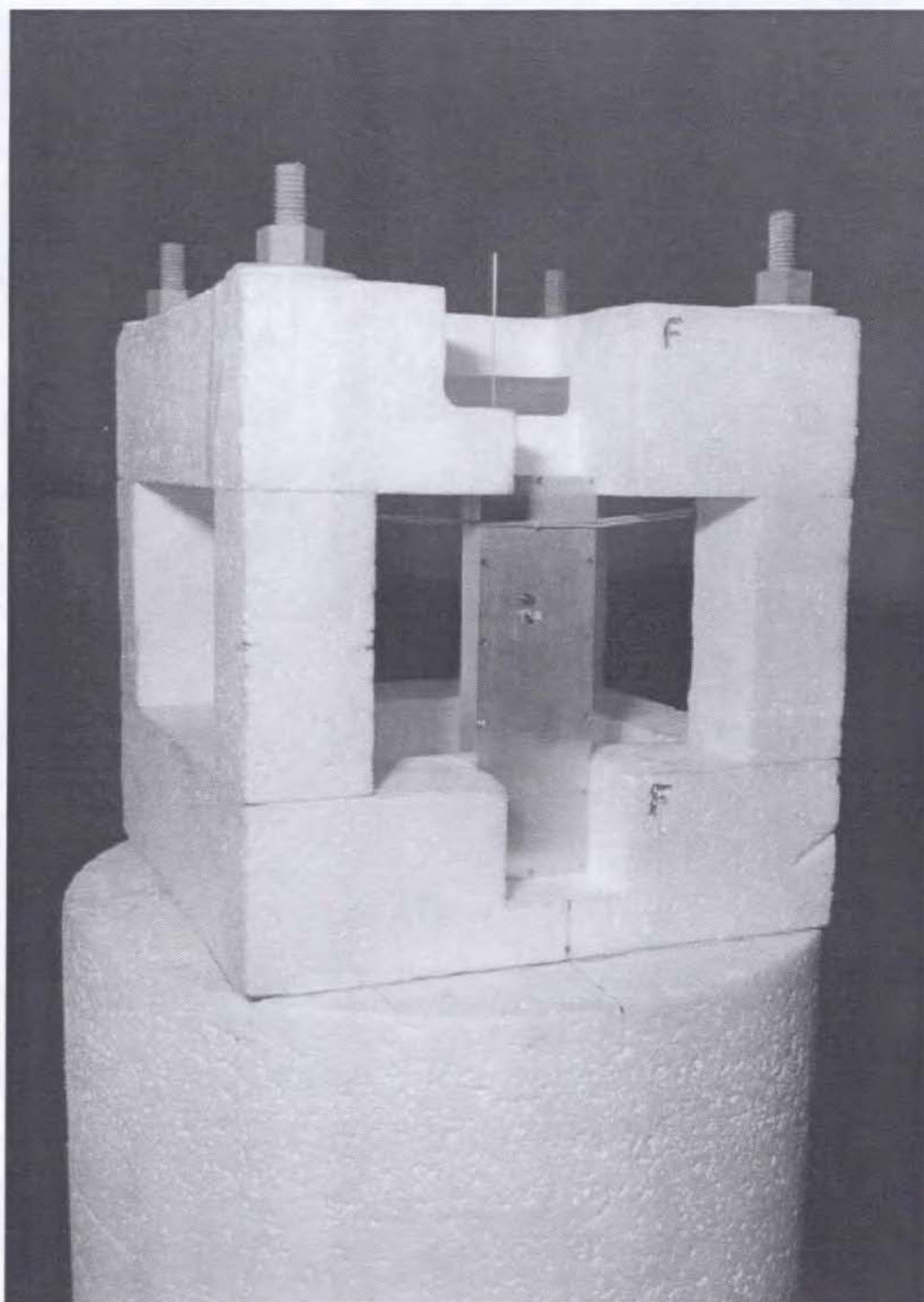


Figure 1.16: The  $\theta = 90^\circ$  principal cut for the second test with the free space head.

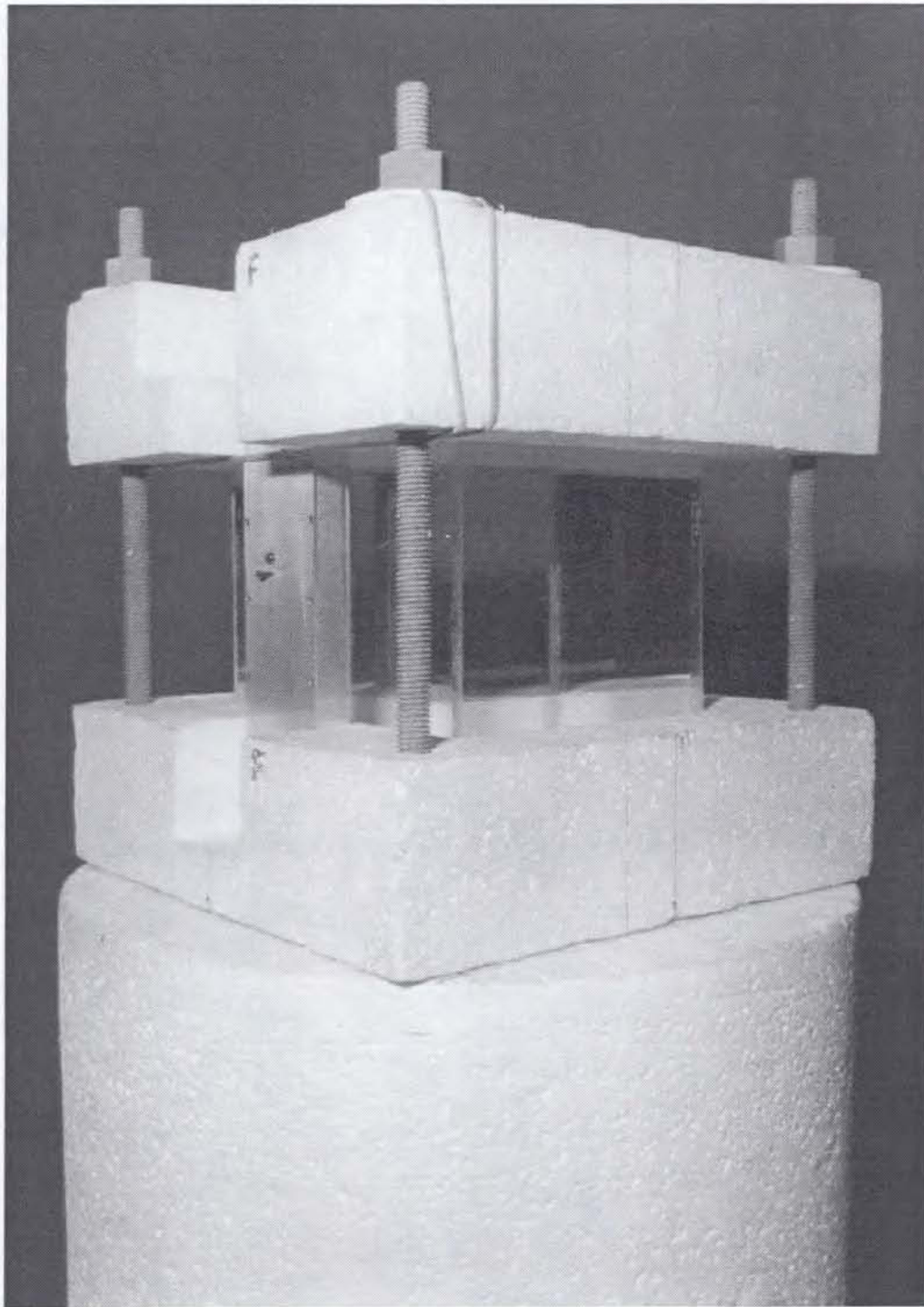


Figure 1.17: The  $\theta = 90^\circ$  principal cut for the second test with the box head.



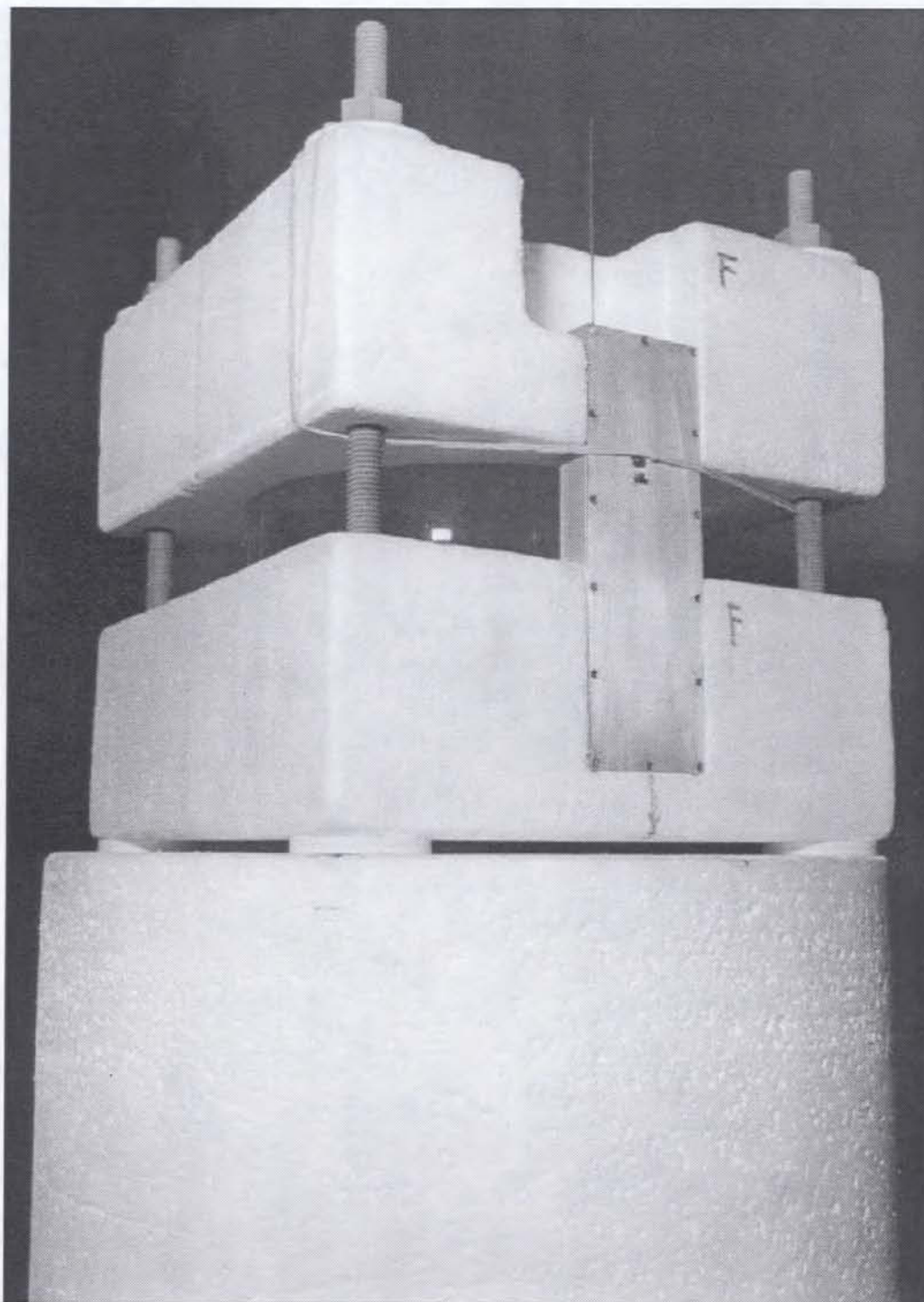


Figure 1.18: The  $\theta = 90^\circ$  principal cut for the second test with the sphere head.

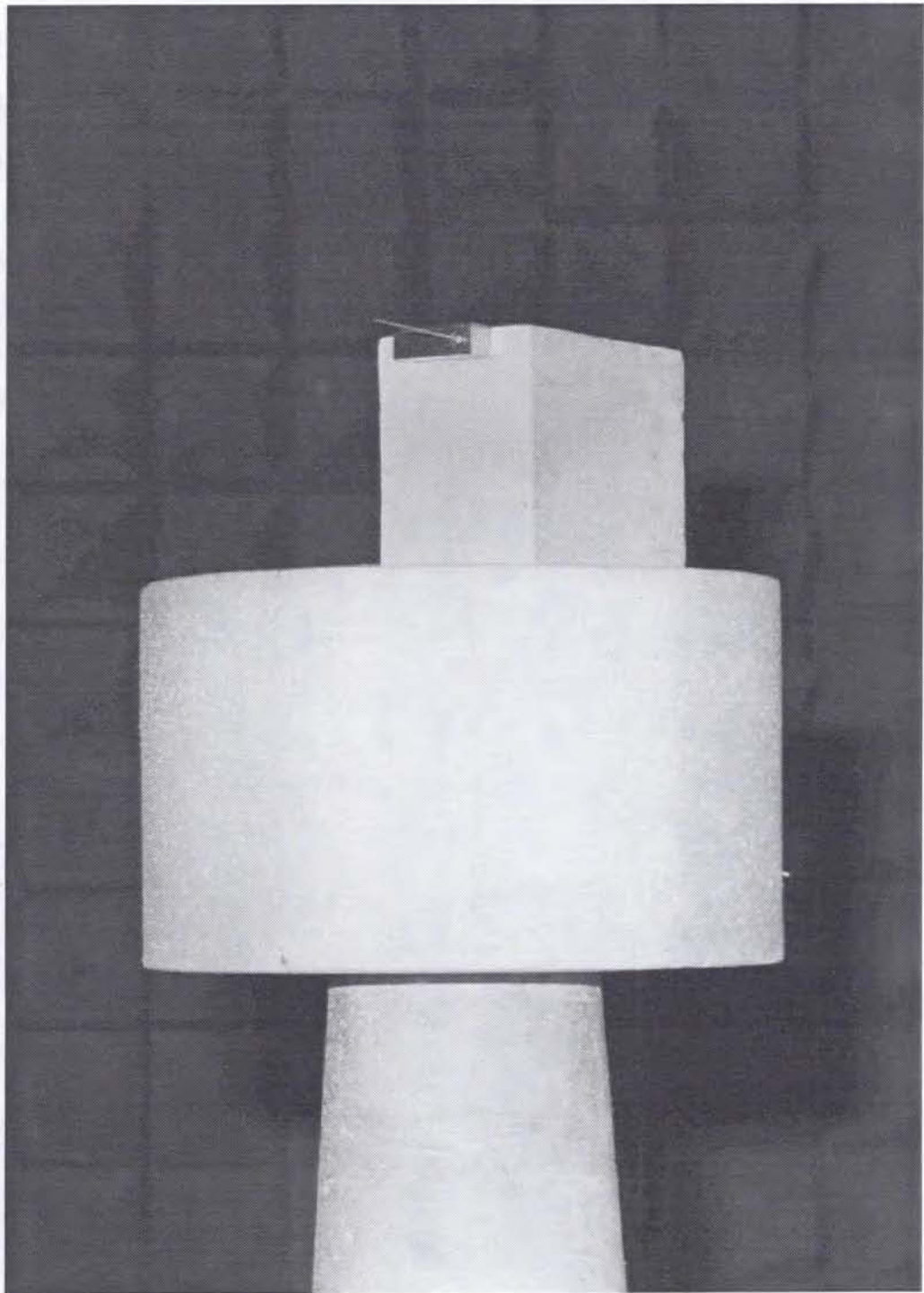


Figure 1.19: The  $\phi = 0^\circ$  principal cut for the first test.



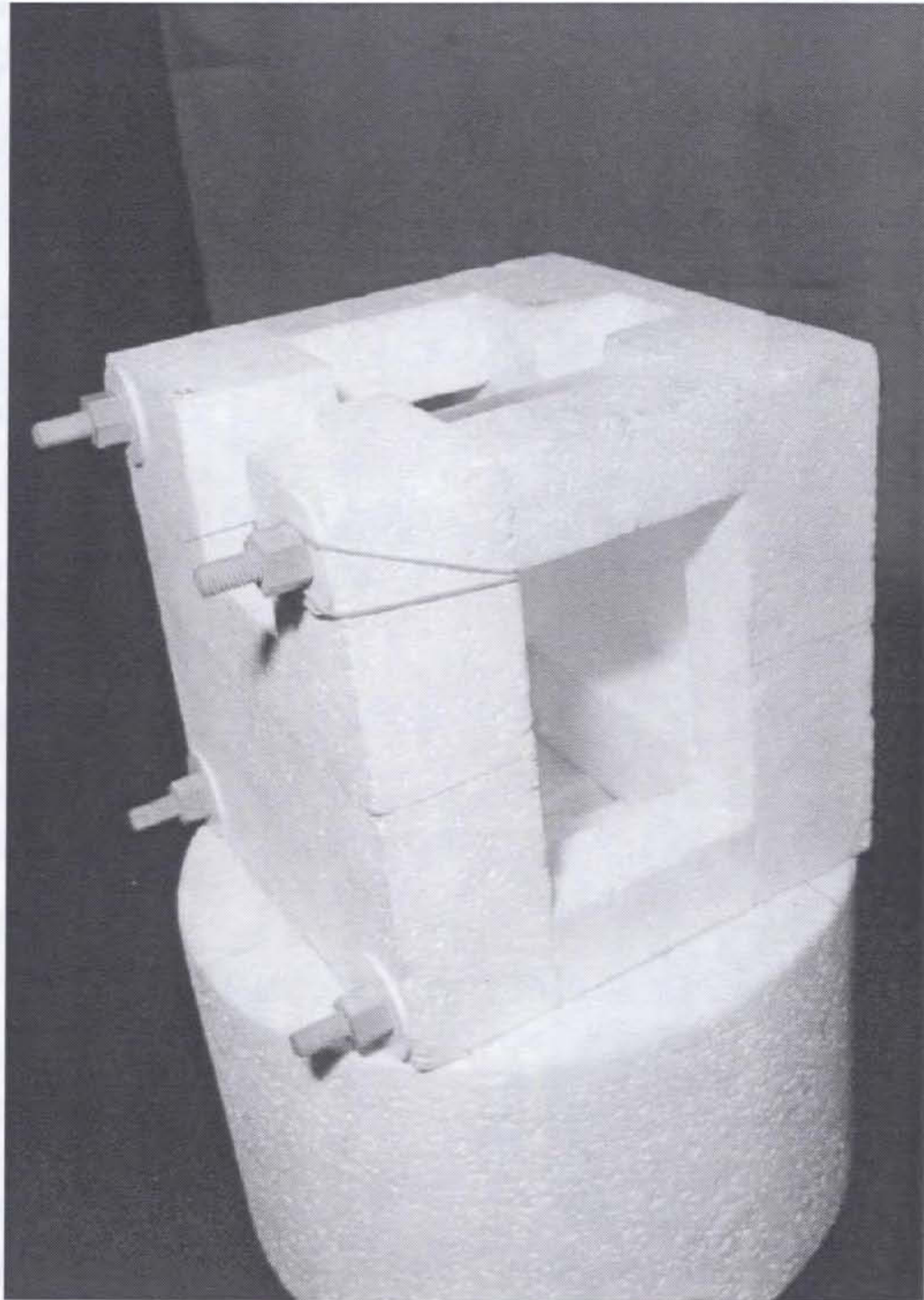


Figure 1.20: The  $\phi = 0^\circ$  principal cut for the second test with the free space head.

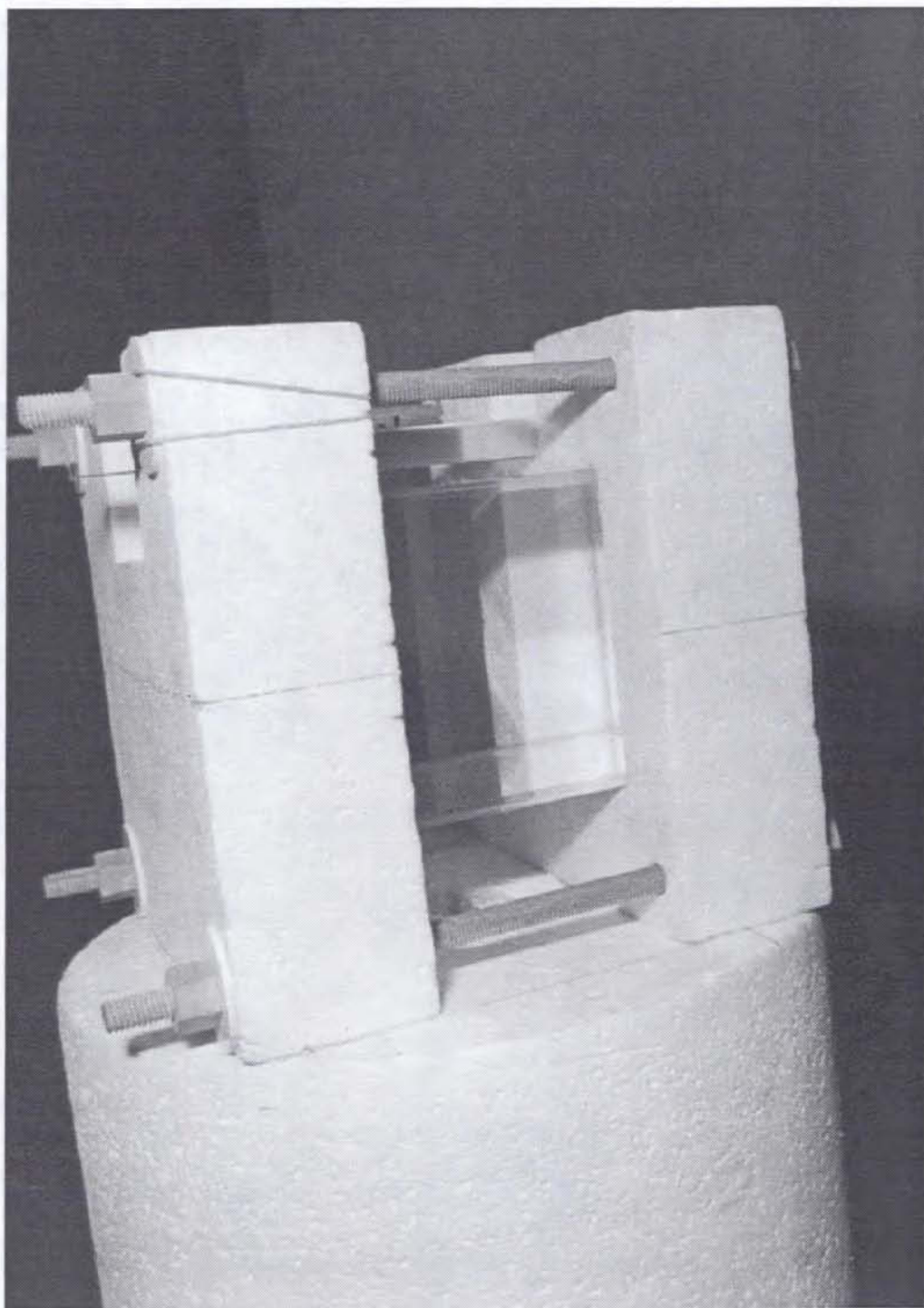


Figure 1.21: The  $\phi = 0^\circ$  principal cut for the second test with the box head.



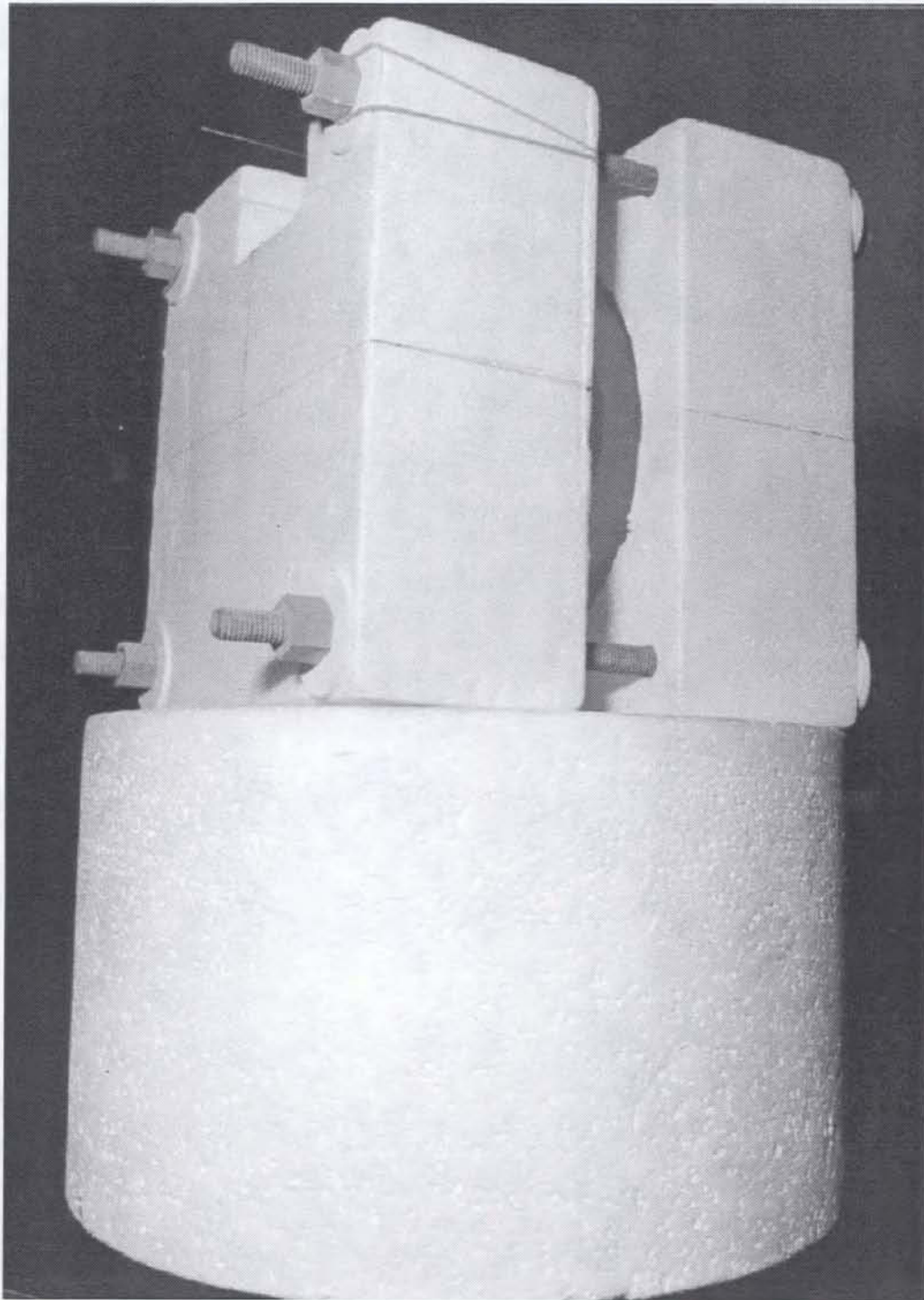


Figure 1.22: The  $\phi = 0^\circ$  principal cut for the second test with the sphere head.



Figure 1.23: The  $\phi = 90^\circ$  principal cut for the first test.



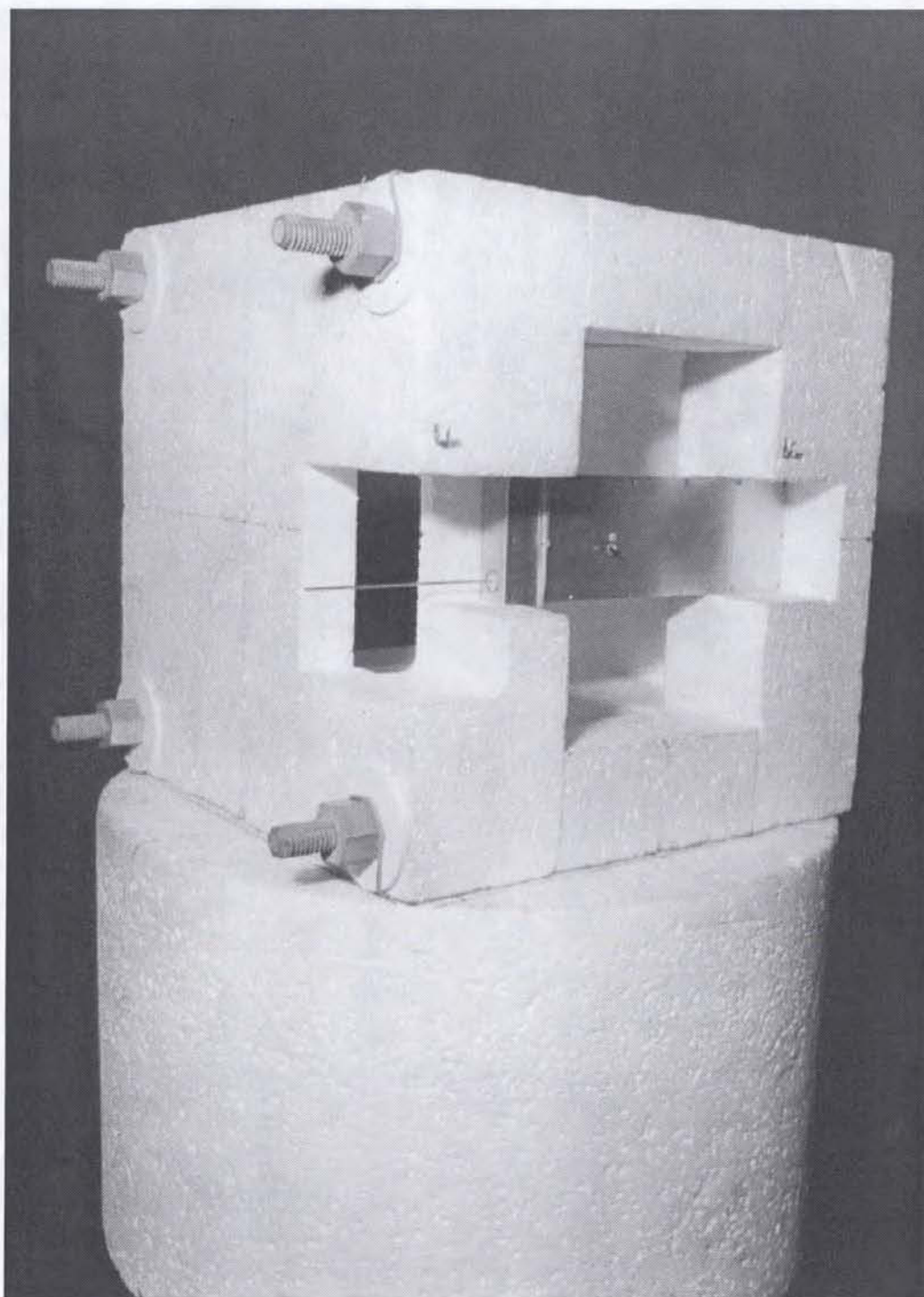


Figure 1.24: The  $\phi = 90^\circ$  principal cut for the second test with the free space head.

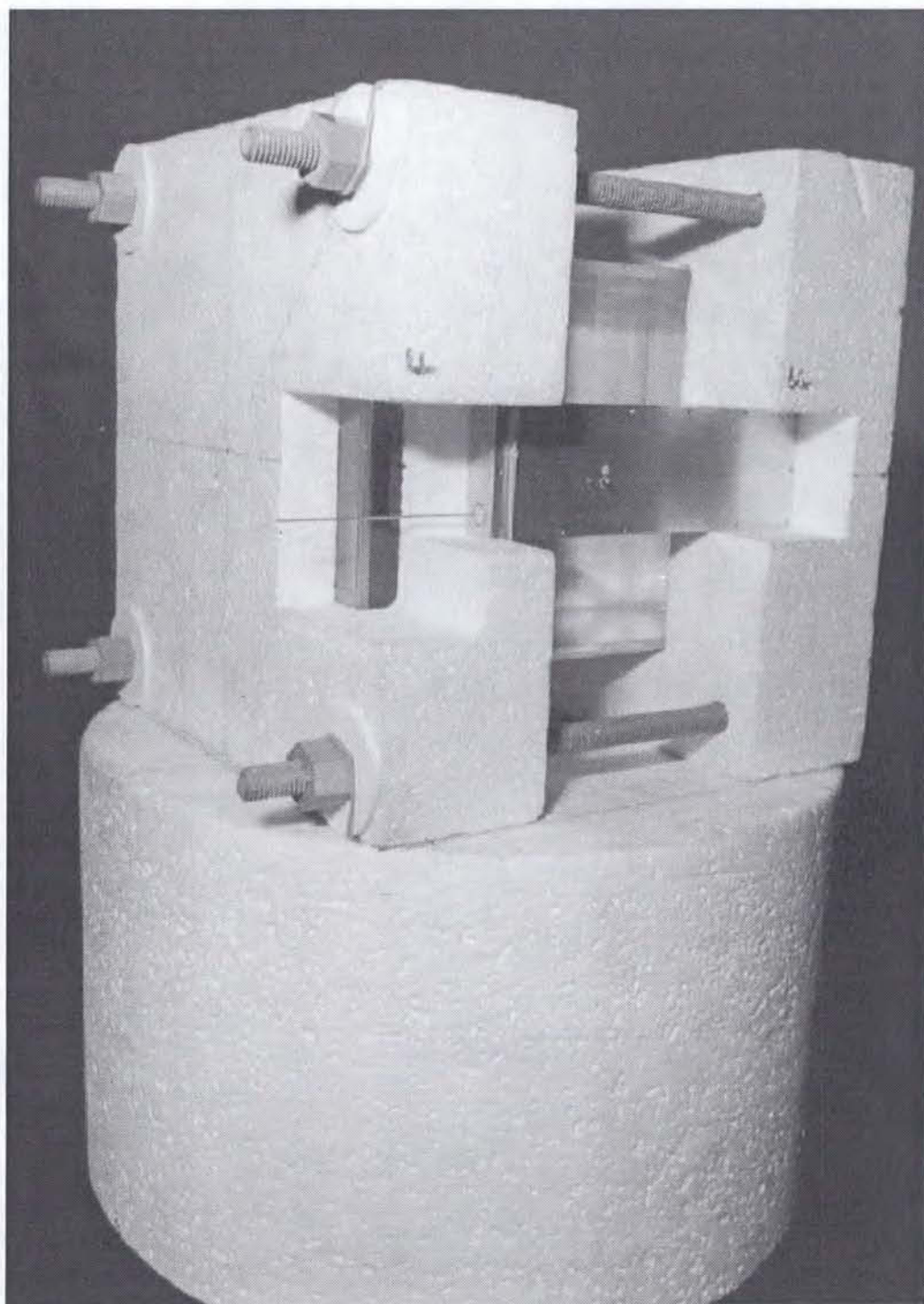


Figure 1.25: The  $\phi = 90^\circ$  principal cut for the second test with the box head.



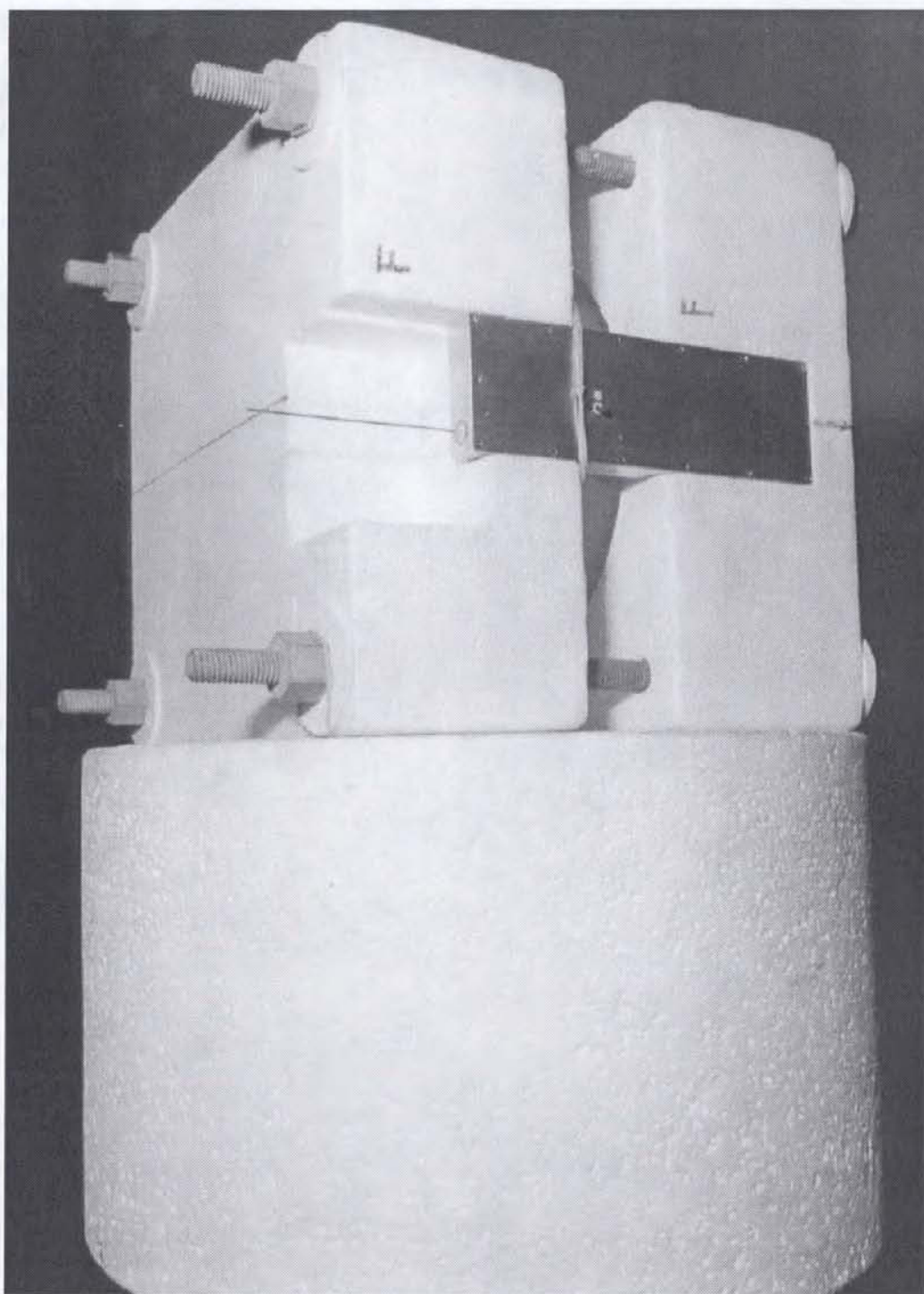


Figure 1.26: The  $\phi = 90^\circ$  principal cut for the second test with the sphere head.

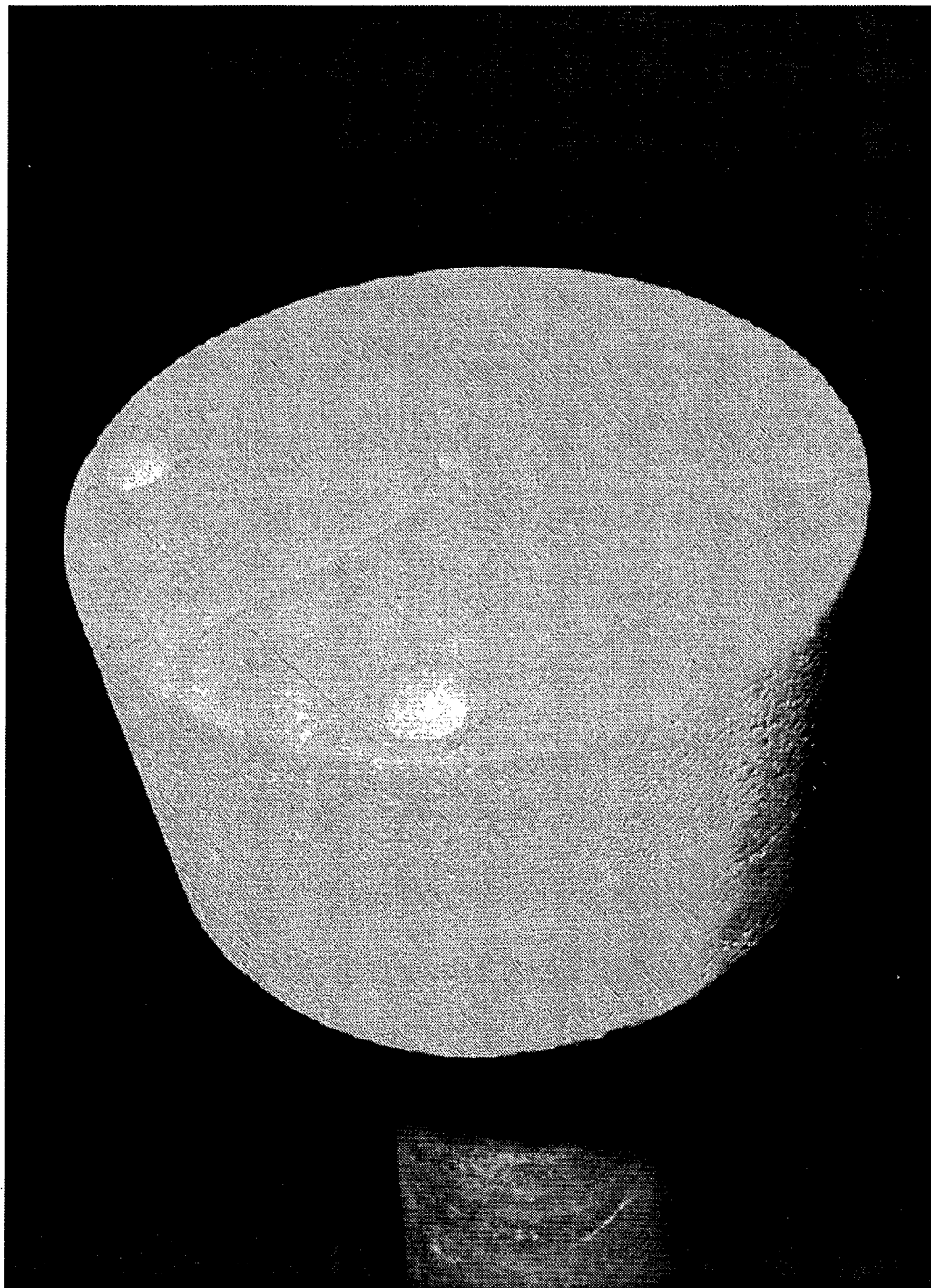


Figure 1.27: The styrofoam disk with the four additional circular holes machined out of its upper surface for the second test.



## 1.4 Experiment setup

For the first test, a different fully charged battery pack was used in the transmitter for each different orientation in order to minimize the power variation during three consecutive runs. The first two runs were made with the network analyzer configured for no ratio between the reference channel and the two test channels, in order to assess the measurement repeatability and the variation in the radiated power level incurred by the battery discharging. A third run was made in order to monitor the power variation of the signal from the reference horn. Both phase and amplitude were measured during each run. The DC voltage of the battery pack with the transmitter in operation was measured before and after the three consecutive runs. For the second test, a different battery pack initially charged between 15.0 V and 15.5 V was used for each different simulated head but the same battery pack was used for all three orientations. The second test was conducted with the network analyzer always configured for no ratio.

For the first test, an averaging of 64 consecutive measurements was used for each point, one point per degree, from  $-180^\circ$  to  $+180^\circ$ . The rotational speed of the azimuth table was adjusted for a continuous but slow motion such that each run lasted about 7.5 minutes in order to minimize the phenomenon of data smearing. For the second test, the data smearing caused by using a continuous scan and data averaging was investigated more systematically. The externally DC supplied transmitter instead of the battery operated transmitter was used in order to avoid the variation in radiated power level caused by the draining of the battery. Various values of rotation speed and various values of data averaging were investigated. By comparing the results for using the continuous scan and a given averaging with the results for using the start-and-stop scan and the maximum averaging, i.e. averaging over 4096 consecutive data values, it was found that a speed of  $0.5^\circ/s$  and a data averaging of 64 consecutive measurements afforded an angular spread of less than  $0.10^\circ$ . The resulting data smearing was found to be about 0.4 dB in magnitude and about  $5^\circ$  in phase for a signal of about -57 dBm in the vicinity of a null region where the pattern presents a large field variation with respect to the angular variation. For strong signals where the gradient is small, the data smearing was much smaller, being within the variations in repeatability, i.e.

about 0.01 dB variation in amplitude and 0.5° variation in phase. The test duration for each pattern cut of the second test was about 18 minutes.

For the second test, the preparation of the brain fluid, the recipe of which is found in Reference [3], proceeded in washing all the containers and tools with hot water and isopropyl alcohol, measuring the weight of the sugar (3.5000 kg), salt (0.1563 kg) and warm deionized water (2.5250 kg) with an electronic scale then mixing the ingredients in a large silver bowl at a room temperature of 20°C. Two such batches were prepared then mixed together and stirred in a large pail. The box and the sphere were also washed both on the inside and outside surfaces then filled with the brain fluid. The simulated heads were then set at rest in order to evacuate the air bubbles, then refilled to the brim. The sphere ended up with just one air bubble at the top (see Figure 1.28) while the box seemed to be free of any air bubble (see Figure 1.29). Between the time of the first test and the time of the second test, however, more bubbles appeared in the sphere and the process of refilling the sphere was repeated many times until only very small air bubbles attached to the inside surface of the sphere remained. The excess fluid from the preparation were put in two sealed plastic bottles. One bottle was kept with the simulated heads at 20°C while the other bottle was kept in a refrigerator. Contrary to the original recipe, no bacteriacide nor HEC gelling agent were used in the preparation and thus, the percentage of the ingredients were adjusted in a pro-rated manner to achieve a total value of 100% in the absence of these two ingredients. Once the simulated heads had been filled with the brain fluid, some small particles were seen to be in suspension in the fluid. It is thought that these particles originated from the electric kettle used in boiling the water.

Measurements of the dielectric properties ( $\epsilon_r = \epsilon'_r - j\epsilon''_r$  with  $\epsilon''_r = \frac{\sigma}{\omega\epsilon_0}$ ) of the brain fluid with an HP85070M dielectric probe at 850 MHz over the temperature range of 10°C to 30°C, and curve fitting to the data points yielded these two parametric equations (Reference [4]):

$$\epsilon'_r = 39.857 - 0.1436T + 8.438 \times 10^{-3}T^2 \quad (1.1)$$

$$\sigma = 1.0808 - 8.0979 \times 10^{-3}T + 3.5663 \times 10^{-4}T^2 \quad (1.2)$$

where  $T$  is the temperature in °C. With  $T = 20^\circ\text{C}$ , there obtained  $\epsilon'_r \approx 40.4$

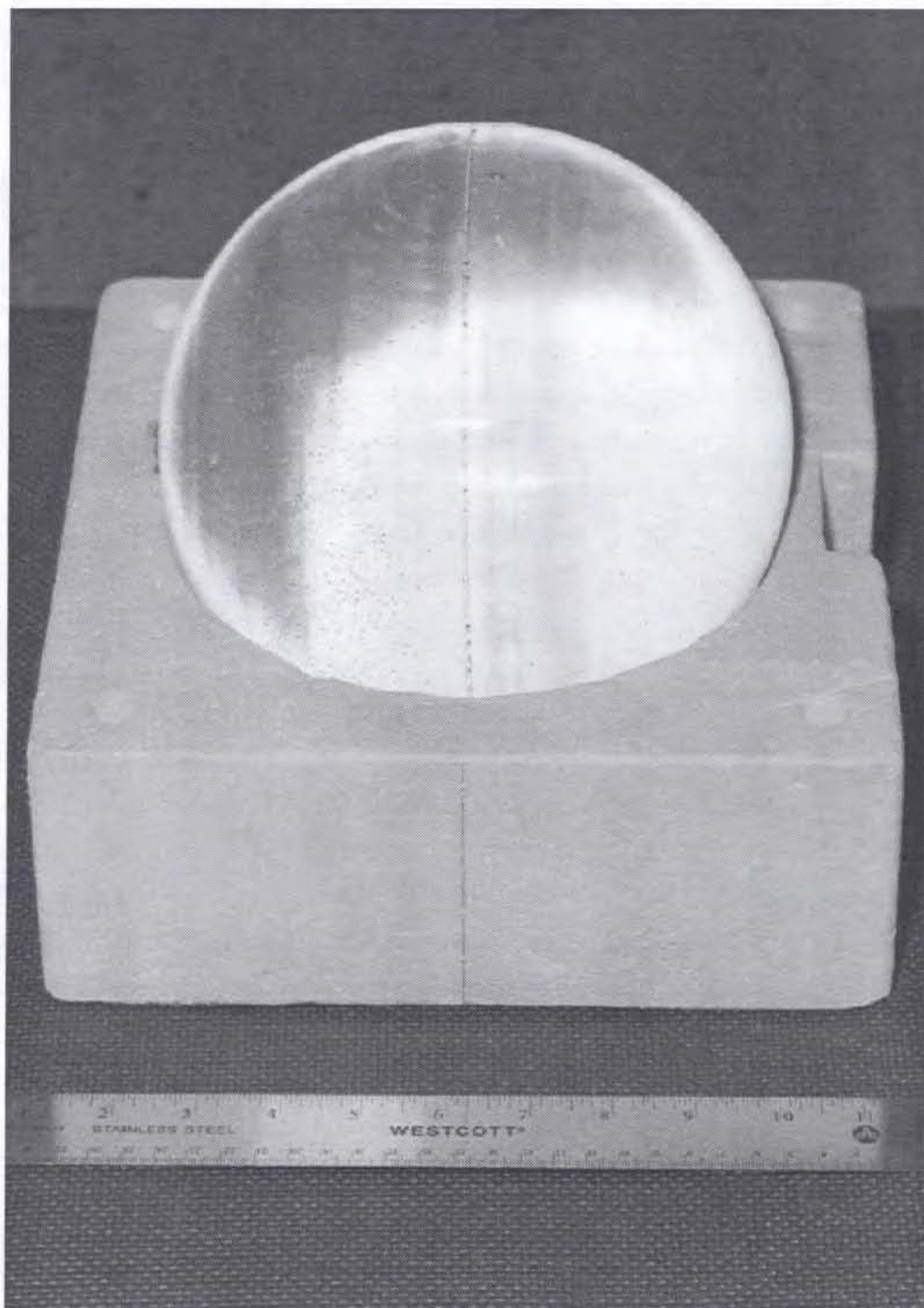


Figure 1.28: The sphere head filled with simulated-brain fluid.



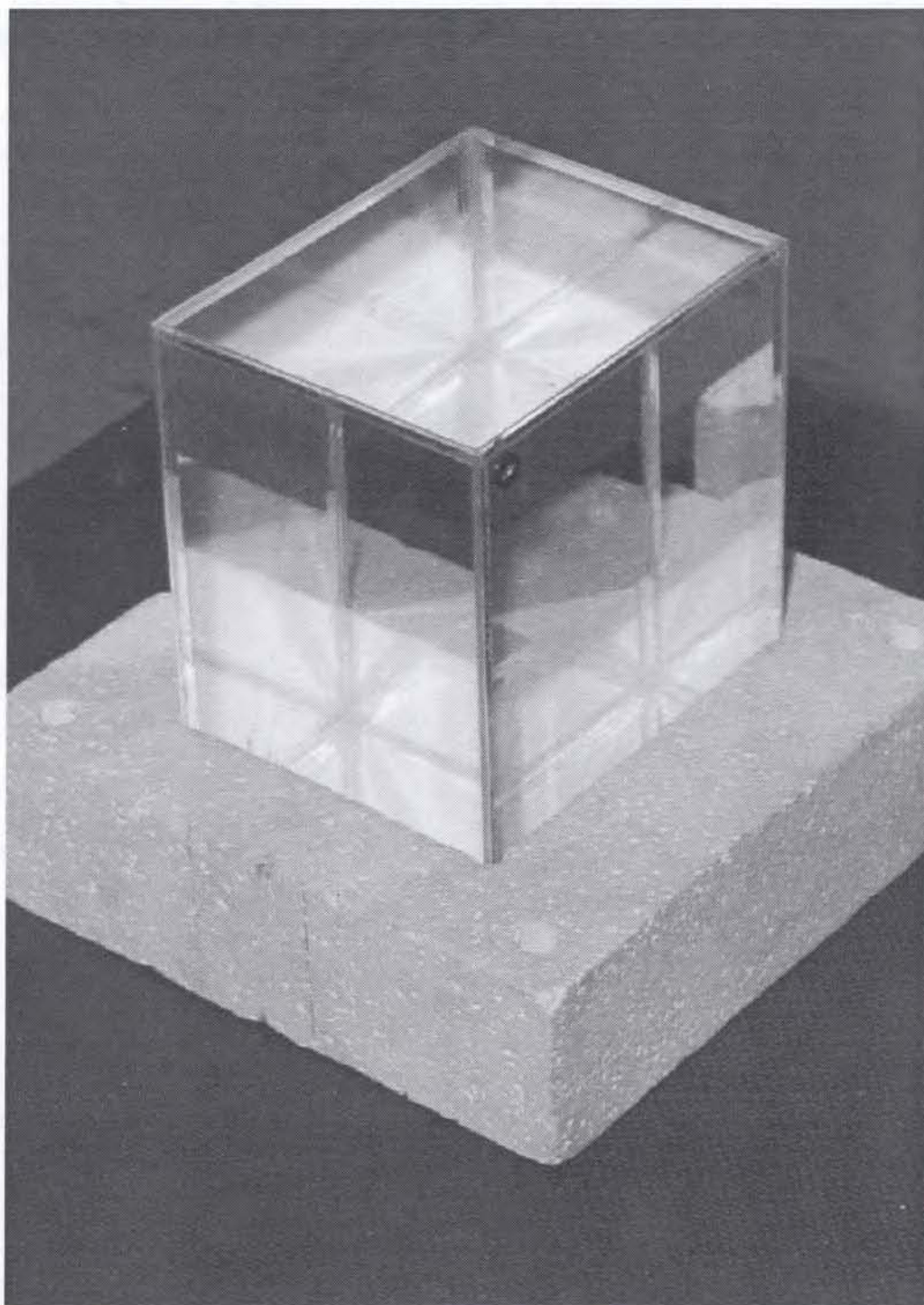


Figure 1.29: The box head filled with simulated-brain fluid.



(dimensionless number) and  $\sigma \approx 1.06$  S/m while the corresponding values predicted by the recipe were 41.2 and 1.2 S/m, respectively.

## Chapter 2

### Results

#### 2.1 Generalities

From the first test, the repeatability of the tests was estimated to be within 0.5 dB in amplitude and  $5^\circ$  in phase, by comparing the measurement results between the first and the second run for each orientation.

The DC voltages of the battery pack with the transmitter under operation were as per Table 2.1 and 2.2.

The data for the power generated by the very same oscillator working into a 50 Ohm resistive load from a cold start was as per Table 2.3.

The power radiated by the transmitter alone could then be estimated as  $P_{in}$  from

Table 2.1: DC voltages of the battery packs for the first test.

Cut	Before test (V)	After test (V)	Battery pack #
$\theta = 90^\circ$	16.40	15.29	A
$\phi = 0^\circ$	???	15.21	C
$\phi = 90^\circ$	16.41	15.38	B
???: Not measured			

Table 2.2: DC voltages of the battery packs for the second test.

Simulated head	Before test (V)	After test (V)	Battery pack #
Free space	15.35	14.60	A
Box	15.40	14.52	B
Sphere	15.40	14.60	C

Table 2.3: RF Power level from the oscillator in function of DC supply voltage, for the oscillator working into a 50 Ohm resistive load and starting from a cold state.

DC Supply Voltage (V)	Power level $P_{in}$ (dBm)
16.51	20.34
16.41	20.17
16.31	20.00
16.20	20.00
16.11	20.00
16.00	19.84
15.91	19.67
15.80	19.67
15.70	19.67
15.61	19.50
15.51	19.50
15.40	19.50
15.31	19.50
15.20	19.50
15.00	19.34
14.50	19.00
14.00	18.67
13.50	18.17
13.00	18.00
12.50	17.67
12.00	17.17
11.50	16.84
11.00	16.17
10.50	15.34
10.00	14.50



Table 2.3 less the return loss corresponding to the impedance mismatch between the 50 Ohm output impedance of the oscillator and the input impedance of the monopole antenna radiating in free space, transformed through the length of the coaxial cable connecting the antenna to the oscillator. The value of this return loss was estimated to be about 1.01 dB (see Appendix B). Similarly, the radiated power could also be estimated in the second test, provided that the return loss was known when the monopole antenna radiated in the presence of each simulated head.

The above information, however, provided only an estimate of the variation of the radiated power level during a measurement run because of the time delay and the temperature cooling that took place between the time that a test ended and the time that the cover of the transmitter was removed for checking the battery voltage. A better gauge for assessing the variation of the radiated power level during a measurement run was obtained by taking the difference between the radiated power levels measured at the azimuth angles of  $-180^\circ$  and  $+180^\circ$  since these two angles corresponded to the same point in space. Unfortunately, it was found that for all three orientations of the first test, the data corresponding to the first data acquisition, i.e. the data for the horizontal polarization at  $-180^\circ$ , was not trustworthy as a result of the data acquisition program failing to clear some data buffer before acquisition. This problem was identified and fixed before the second test was conducted. Using the externally DC supplied transmitter, the variation of the radiated power levels between the results at  $-180^\circ$  and  $+180^\circ$  was found to be less than 0.05 dB in amplitude and thus, the variation of the radiated power level during a measurement run with the battery operated transmitter was then reliably estimated from the difference between the power level at  $-180^\circ$  and the power level at  $+180^\circ$ . However, this variation of the radiated power level between the results at  $-180^\circ$  and  $+180^\circ$  does not come out to be necessarily the same for the two polarizations in the same run. This situation is thought to owe mostly to the facts that:

1. the signal strength at  $\pm 180^\circ$  is widely different for the two polarizations and that the amount of data smearing varies with the gradient value of the pattern with respect to the angular variation;
2. the effect of the multipath in the anechoic chamber is different between the

Table 2.4: The largest differences in power level between the azimuth angles of  $-180^\circ$  and  $+180^\circ$  among the two different polarizations for the second test.

Simulated head	Principal plane			Battery pack #
	$\theta = 90^\circ$	$\phi = 0^\circ$	$\phi = 90^\circ$	
Free space	-0.05 dBm	-0.11 dBm	-0.13 dBm	A
Box	-0.09 dBm	-0.10 dBm	-0.15 dBm	B
Sphere	-0.07 dBm	-0.08 dBm	-0.12 dBm	C

co-polarization and the cross-polarization signals.

The finite resolution of the positioner, being as good as about  $0.007^\circ$ , is not thought to be a significant cause for the variation between the results at  $-180^\circ$  and  $+180^\circ$ . For the second test, the largest differences among the two polarizations were found to be as per Table 2.4.

## 2.2 Plots

This section presents all the magnitude plots for the first and the second tests. The data is also available in ASCII format on a small diskette.

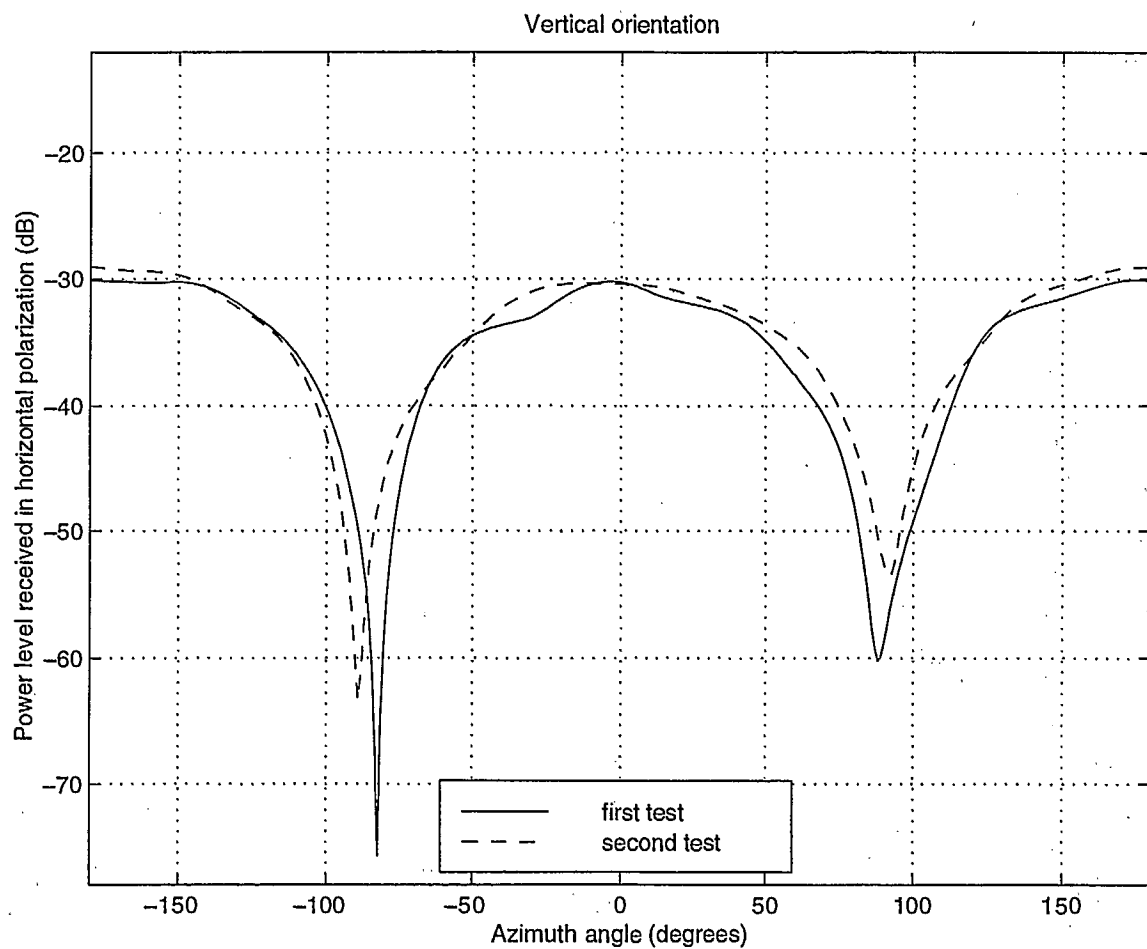


Figure 2.1: The magnitude of the horizontal polarization signals for the  $\theta = 90^\circ$  orientation in the first and second (free space head) tests, respectively.



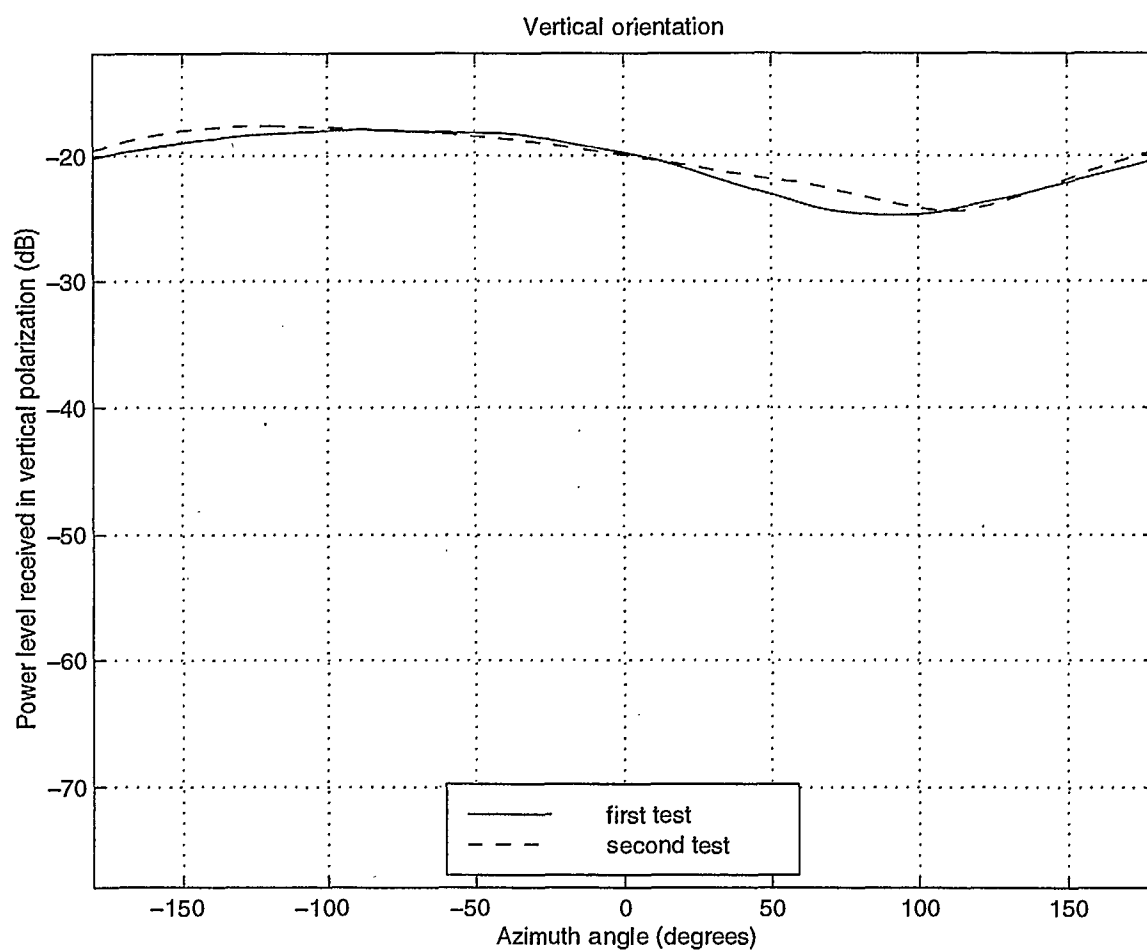


Figure 2.2: The magnitude of the vertical polarization signals for the  $\theta = 90^\circ$  orientation in the first and second (free space head) tests, respectively.

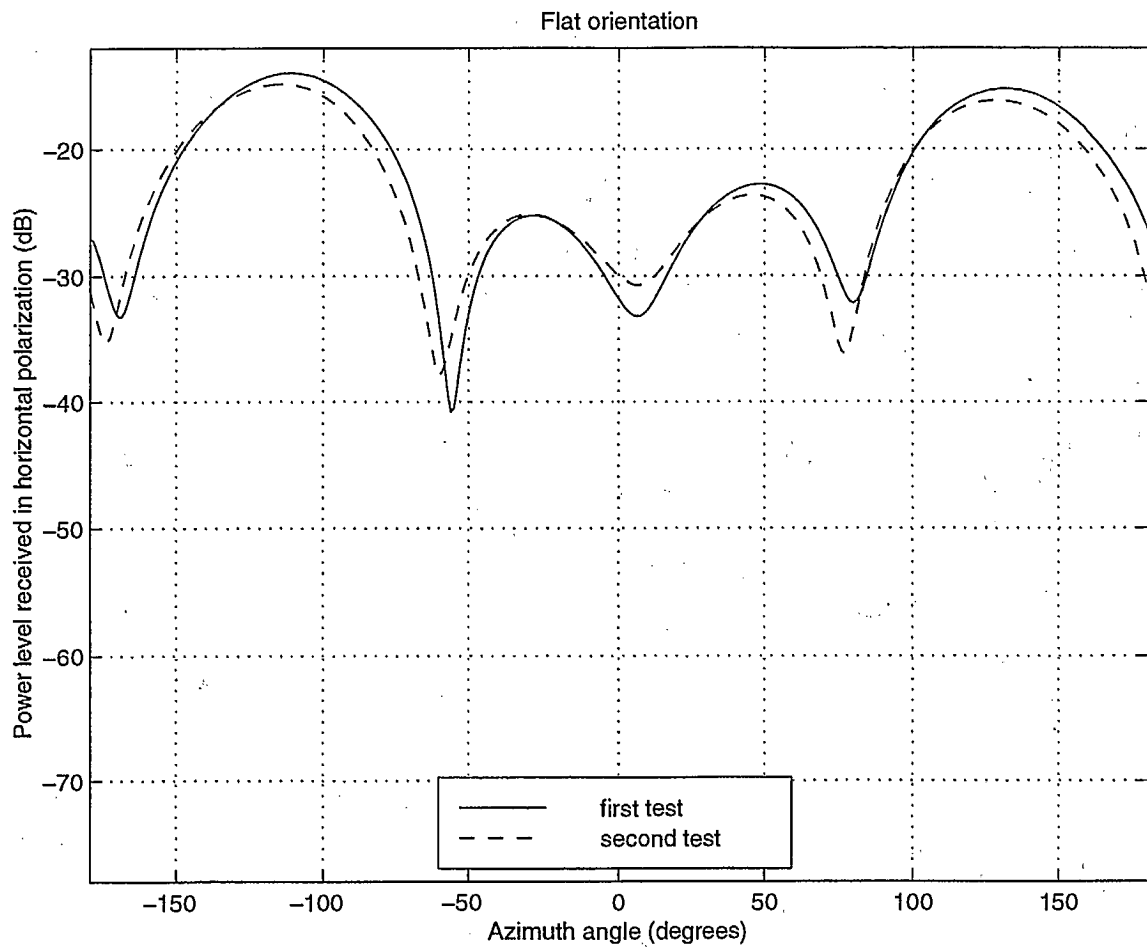


Figure 2.3: The magnitude of the horizontal polarization signals for the  $\phi = 0^\circ$  orientation in the first and second (free space head) tests, respectively.

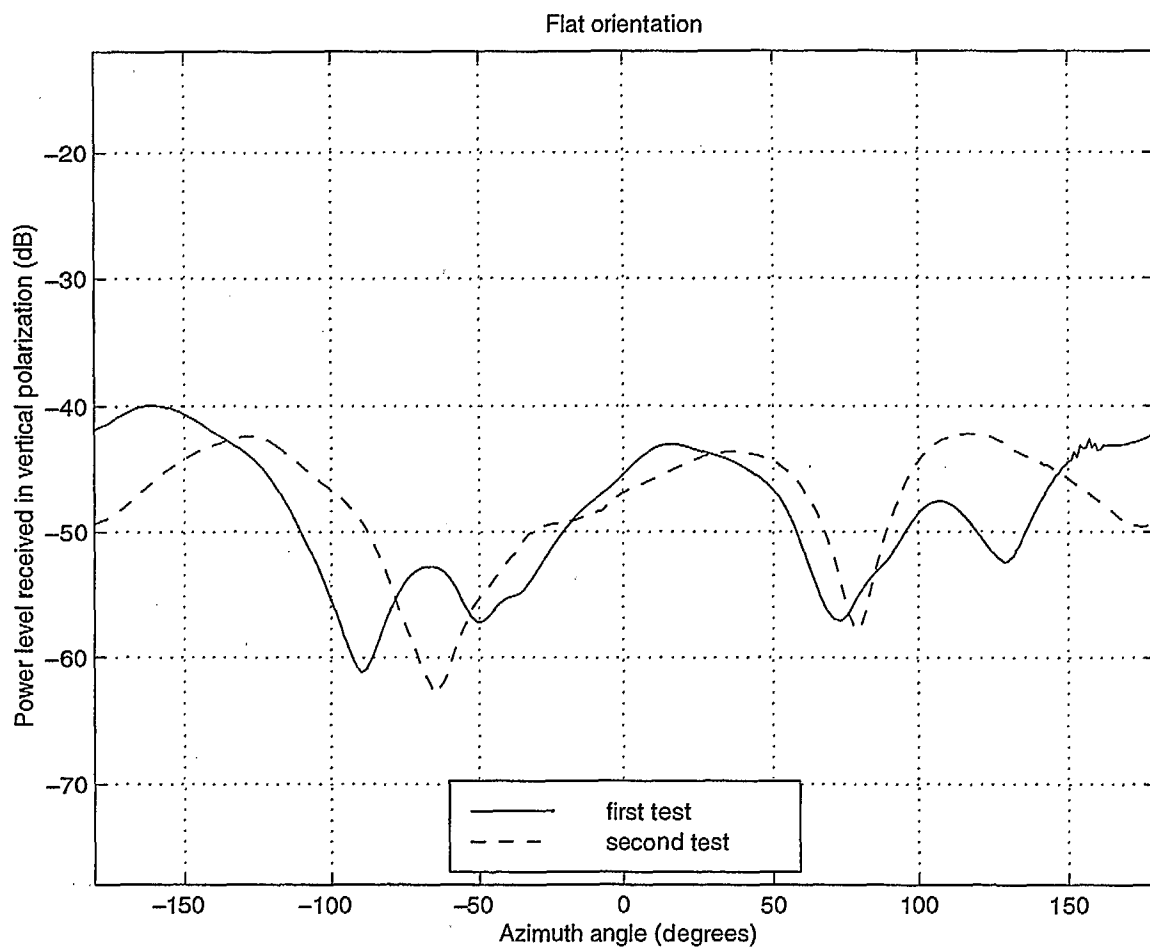


Figure 2.4: The magnitude of the vertical polarization signals for the  $\phi = 0^\circ$  orientation in the first and second (free space head) tests, respectively.



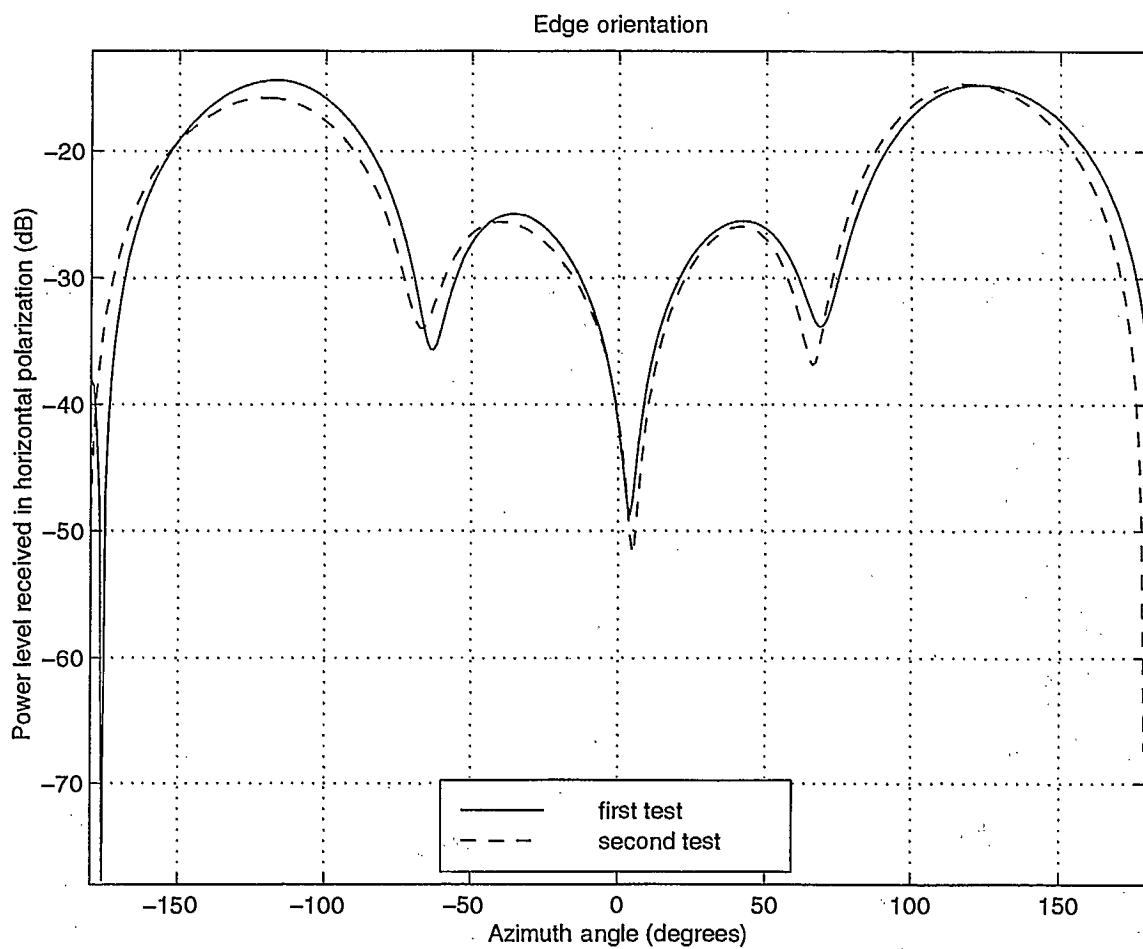


Figure 2.5: The magnitude of the horizontal polarization signals for the  $\phi = 90^\circ$  orientation in the first and second (free space head) tests, respectively.

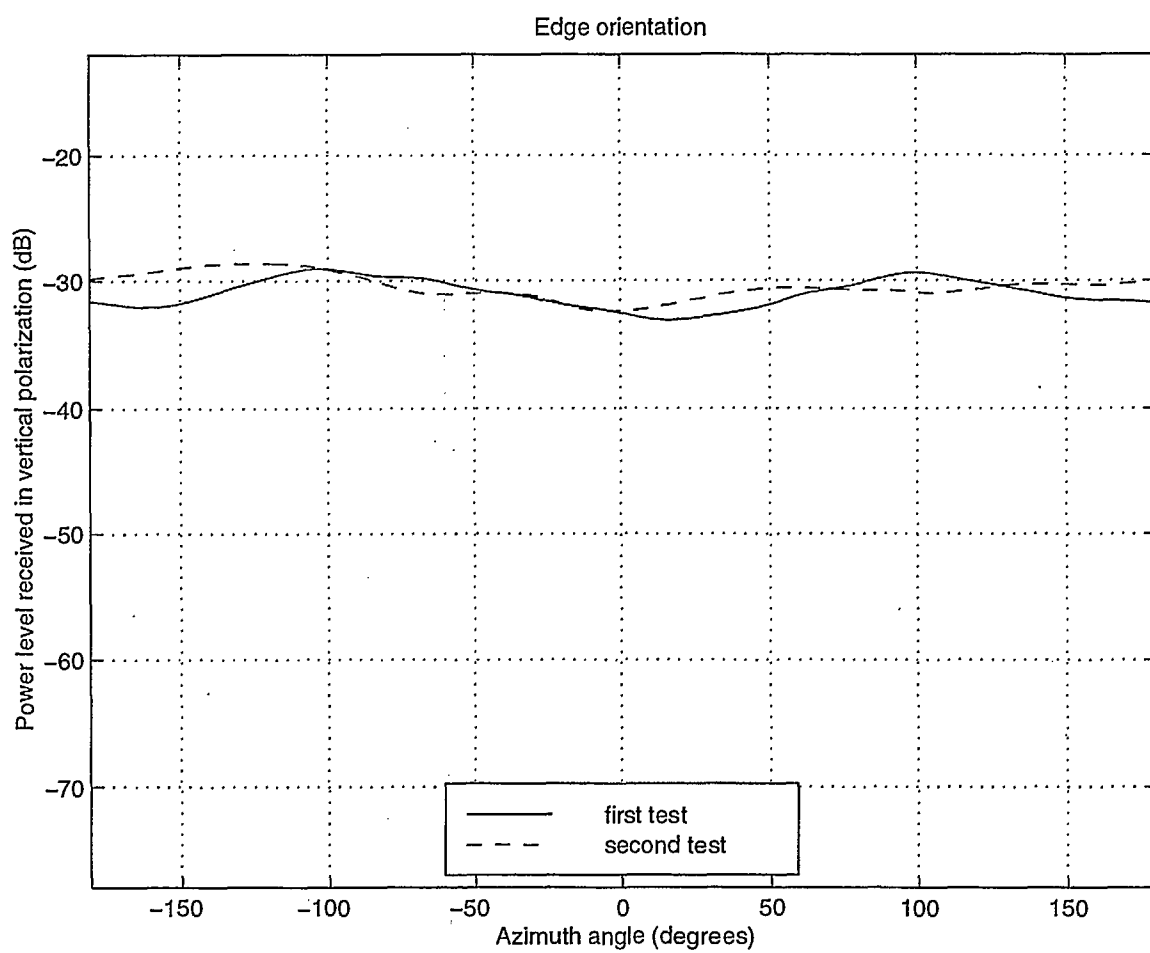


Figure 2.6: The magnitude of the vertical polarization signals for the  $\phi = 90^\circ$  orientation in the first and second (free space head) tests, respectively.

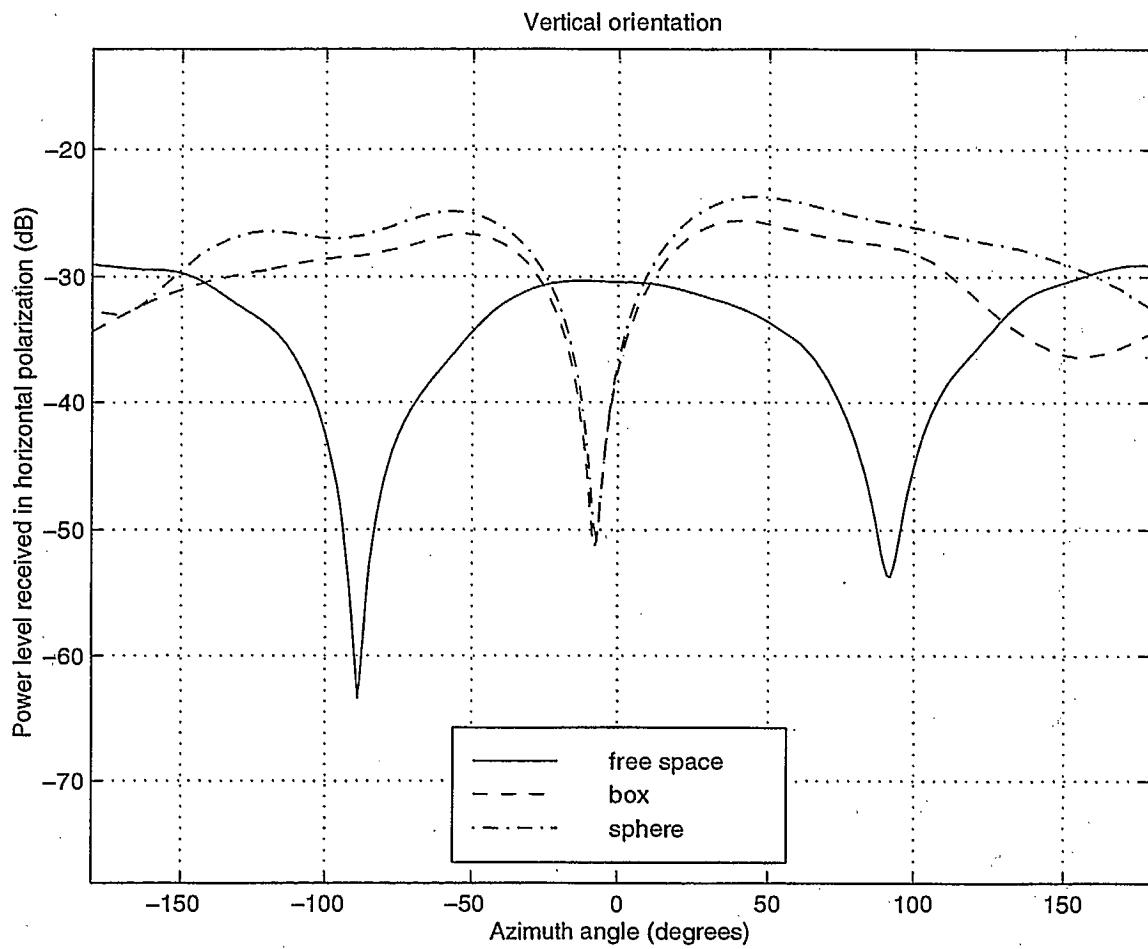


Figure 2.7: The magnitude of the horizontal polarization signals for the  $\theta = 90^\circ$  orientation in the second test with the free space, the box and the sphere heads.

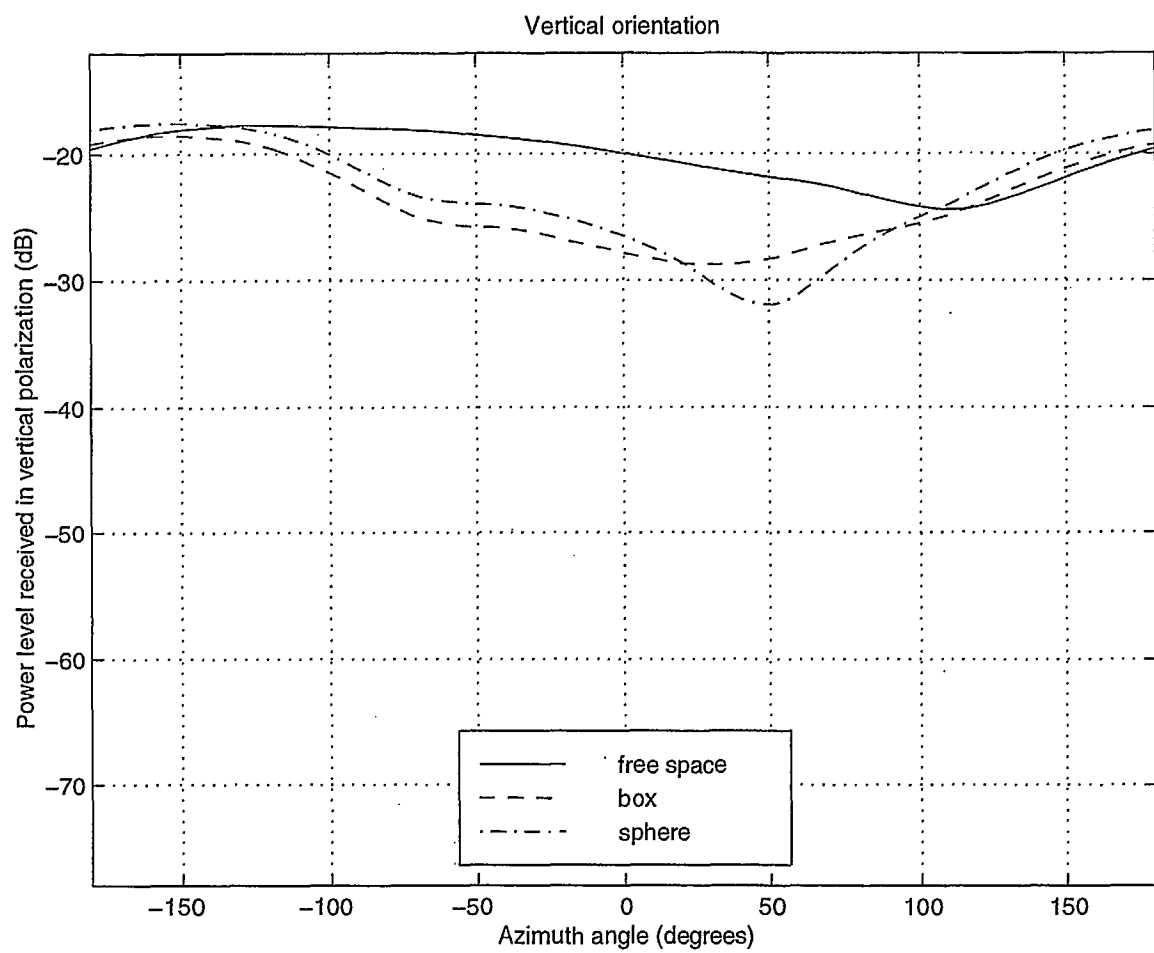


Figure 2.8: The magnitude of the vertical polarization signals for the  $\theta = 90^\circ$  orientation in the second test with the free space, the box and the sphere heads.



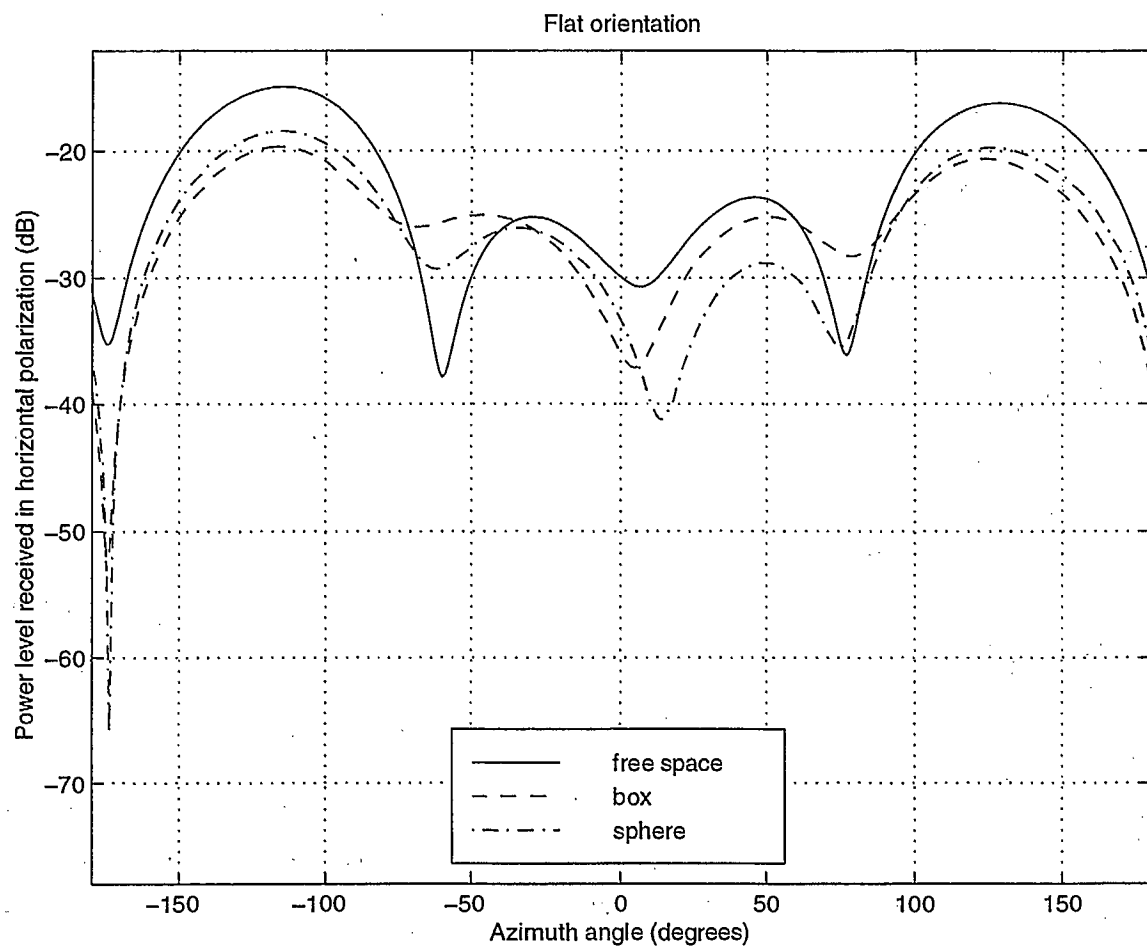


Figure 2.9: The magnitude of the horizontal polarization signals for the  $\phi = 0^\circ$  orientation in the second test with the free space, the box and the sphere heads.

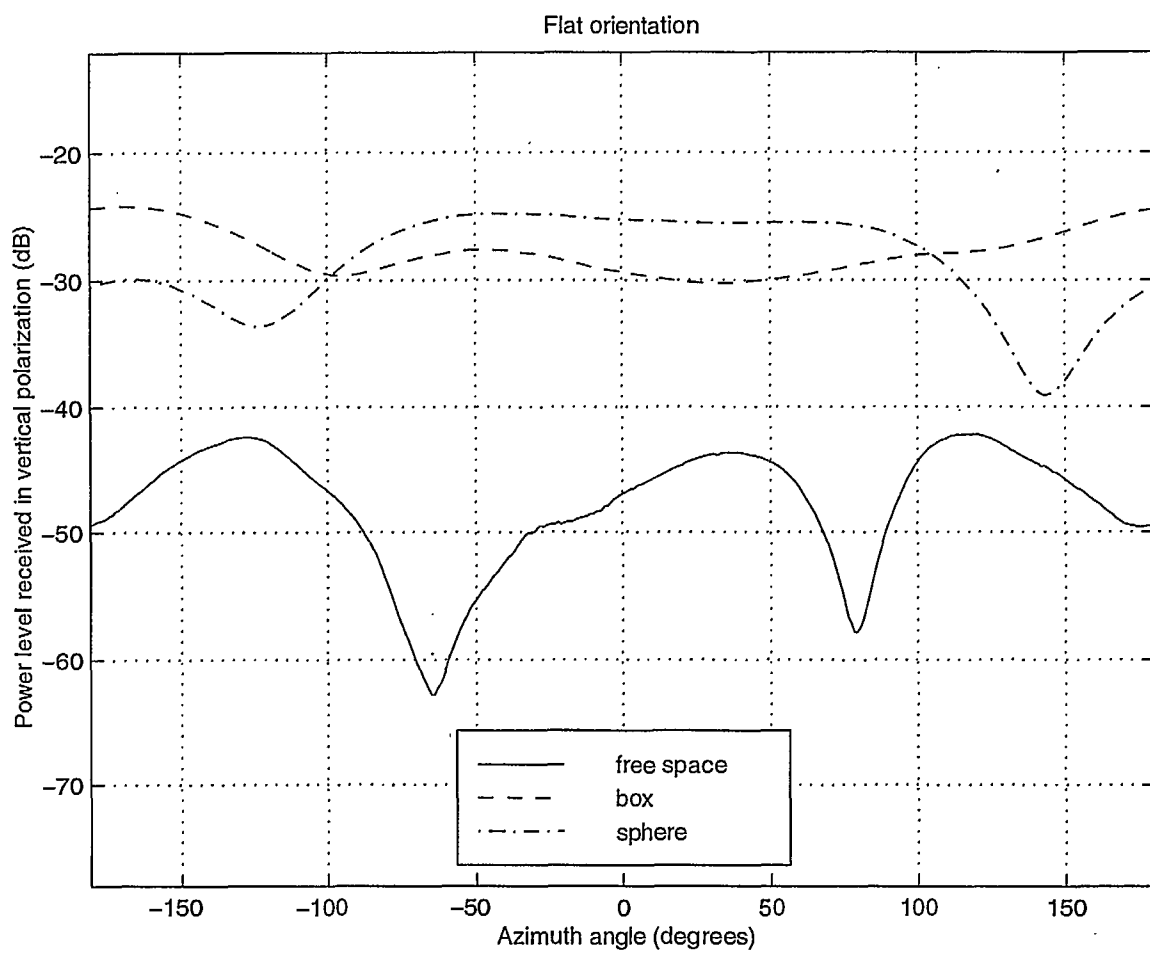


Figure 2.10: The magnitude of the vertical polarization signals for the  $\phi = 0^\circ$  orientation in the second test with the free space, the box and the sphere heads.

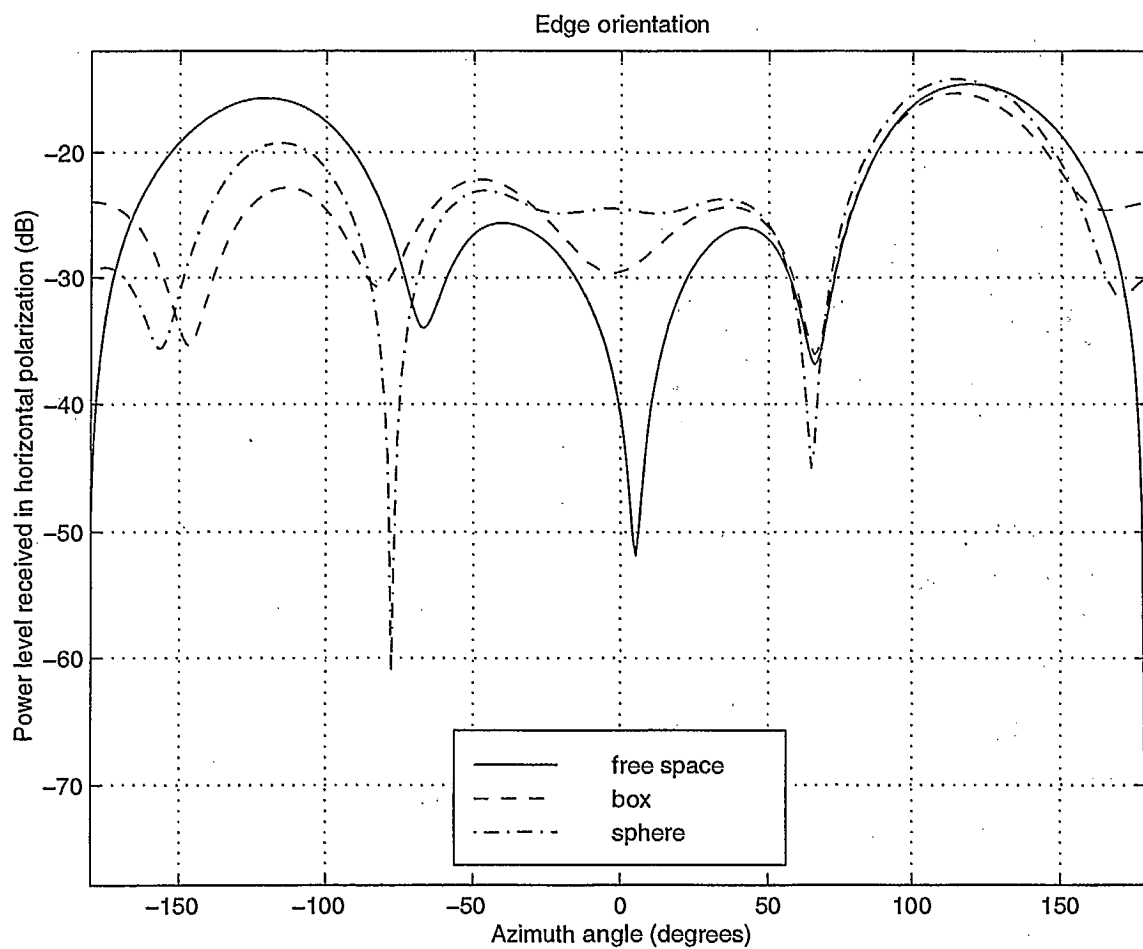


Figure 2.11: The magnitude of the horizontal polarization signals for the  $\phi = 90^\circ$  orientation in the second test with the free space, the box and the sphere heads.

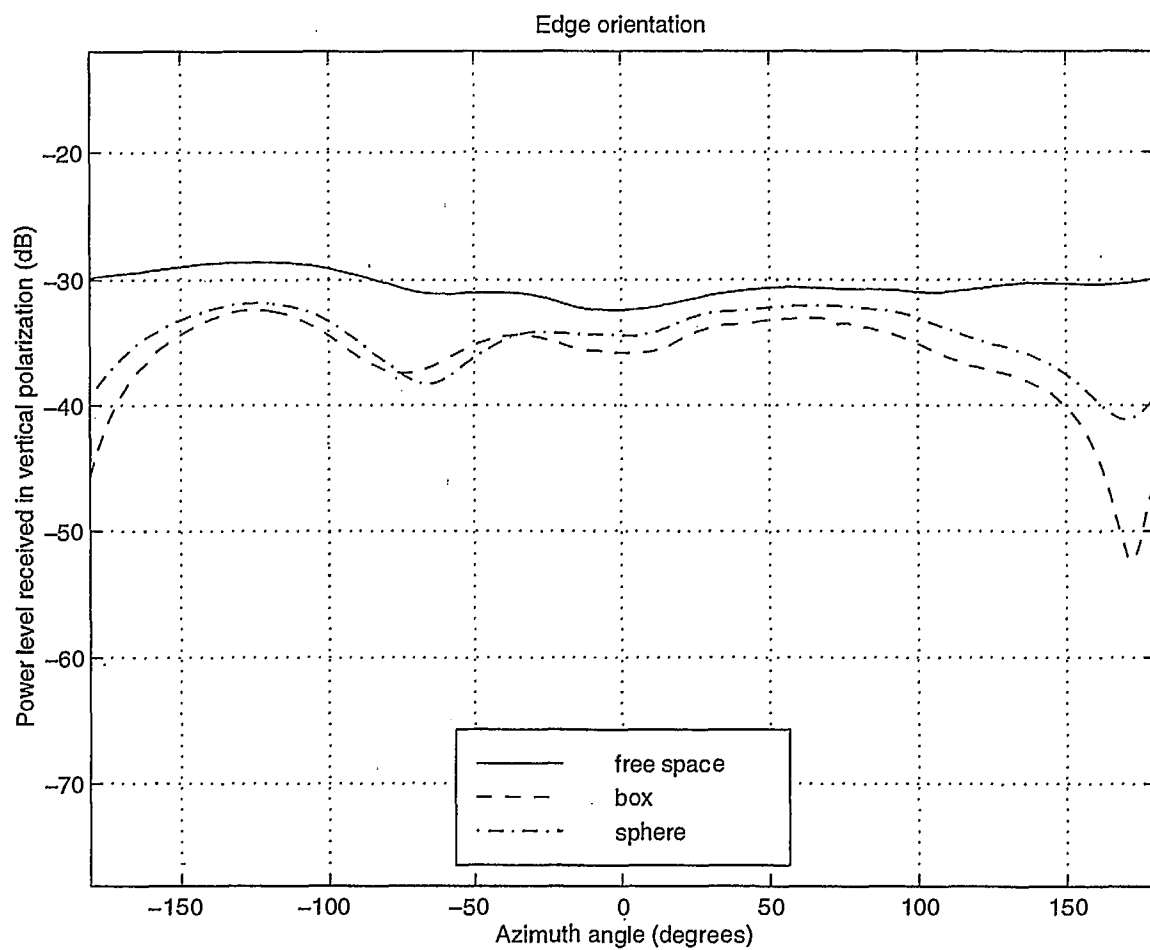


Figure 2.12: The magnitude of the vertical polarization signals for the  $\phi = 90^\circ$  orientation in the second test with the free space, the box and the sphere heads.



## 2.3 Discussion

The existence of the co-polarization and cross-polarization signals can be explained in terms of the existence of equivalent currents induced on the various faces of the metallic case and in the volume of the dielectric bodies surrounding the antenna. From the equivalence principle, the conducting surfaces of the metallic case can be replaced by equivalent surface currents and the simulated heads can be replaced by equivalent volume polarization currents, all these equivalent currents being electric and existing in free space.

As expected, the dominant signal for most azimuth angles had the polarization corresponding to the orientation of the monopole antenna, although the cross-polarization signal was much stronger when a lossy material (i.e. box or sphere heads) was present in the vicinity of the antenna, specially for the vertical and the flat orientations.

In Figure 2.1, the curves for the cross-polarization signals showed deep notches at about  $\pm 90^\circ$  because for the vertical orientation, the equivalent surface currents with the most horizontal orientation laid on the top and bottom surfaces of the metallic case such that these surfaces acted as fat dipoles. Consequently, as dipoles, they produced the least radiation in the direction of their axes. As expected, the level of the curves for the cross-polarization signals in Figure 2.4 was much smaller than that for the co-polarization signals in Figure 2.3 because for the flat orientation, the equivalent surface electric currents were mostly horizontal.

In Figure 2.2, the curves for the co-polarization signals were asymmetrical because the monopole antenna was located asymmetrical on the metallic case of the transmitter. In Figure 2.5, the curve for the first test should be perfectly symmetrical about the  $0^\circ$  azimuth angle because for the edge orientation, the geometry of the transmitter was symmetrical with respect to the origin of the coordinate system (i.e. the base of the monopole antenna). This expectation was well borne out by the measurement results except for a misalignment of the angle about which the curve was to be symmetrical. In contrast, in the same figure, the curve for the second test was not nearly as symmetrical because the transmitter no longer laid on the axis of

rotation of the azimuth table.

A comparison between the figures for the first test with those for the second test for the free space head showed that all the co-polarization curves have the same trend in the first as in the second tests. Since the location of the pivot point was changed from being at the base of the antenna in the first test, to being at the center of the styrofoam assembly in the second test, the measured data for the second test was affected by a variation of the power level resulting from a variation of the separation distance between the monopole antenna and the receive horn, and a variation of the angle of arrival at the receive horn, as the azimuth table was rotated from  $-180^\circ$  to  $+180^\circ$ . According to the drawings in Appendix D, the base of the monopole antenna laid at  $x=18.15$  mm,  $y=87.8$  mm and  $z=62.3$  mm in the system of coordinate of Figure 1.13. Taking the separation distance between the pivot point of the azimuth table and the aperture of the receive horn to be 331.5 cm, the resulting maximum angular variation was about  $1.5^\circ$  for the vertical orientation, about  $1.9^\circ$  for the edge orientation, and about  $1.1^\circ$  for the flat orientation, at the azimuth angles of  $+90^\circ$  or  $-90^\circ$ . Assuming a  $1/r$  variation for the far field and taking separation values between the pivot point of the azimuth table and the aperture of the receive horn to be 334.6 cm in the first test and 331.5 cm in the second test, the resulting maximum power variation was about:

$$20 \log_{10} \left( \frac{334.6}{331.5 \pm 9.0} \right) \approx \mp 0.3 \text{ dB for the vertical orientation;}$$

$$20 \log_{10} \left( \frac{334.6}{331.5 \pm 10.8} \right) \approx \mp 0.4 \text{ dB for the edge orientation;}$$

$$20 \log_{10} \left( \frac{334.6}{331.5 \pm 6.5} \right) \approx \mp 0.3 \text{ dB for the flat orientation.}$$

Other possible reasons for the difference in the measured data were:

1. the presence of the styrofoam assembly with its fiberglass threaded rods and nuts, and plexiglass washers;
2. the greater uncertainty in aligning the device under test in the second test;
3. the fact that the monopole antenna required to be resoldered between the two tests as a result of accidentally hitting the antenna.

The most striking effect due to the presence of the simulated heads was found in Figures 2.7 and 2.10. These two figures show that the presence of a lossy dielectric body, like the box or the sphere heads, incurred the presence of strong cross-polarization levels over most of the angular range. This significant change occurred for both simulated heads regardless of the specific shape of the simulated head. Interestingly, Figure 2.11 shows that for the edge orientation, the cross-polarization plot of the sphere head had two nulls at about  $-80^\circ$  and  $+65^\circ$ , that were much deeper than those seen in the cross-polarization plot of the box head. Interestingly also is the observation that the cross-polarization levels for the flat orientation in Figure 2.10 always remained higher for the lossy heads than those for the free-space head whereas the cross-polarization levels for the edge orientation in Figure 2.12 remained lower for the lossy heads than those for the free-space head.

In Figure 2.9, the presence of a lossy head incurred the presence of a significant level of cross-polarization to an amount that was, for some measurement angles, comparable or even greater than the co-polarization level. Surprisingly, however, the cross-polarization levels in Figure 2.7 about  $0^\circ$  and  $180^\circ$  are seen to be lower for the box and the sphere heads than those for the free-space head. Whereas the cross-polarization level was minimum at about  $+90^\circ$  and  $-90^\circ$  with the free-space head, these nulls shifted to about  $0^\circ$  and  $180^\circ$  for the box and the sphere heads, although the depth of the  $180^\circ$  null was also reduced by more than 10 dB. Yet, this decrease of the cross-polarization level in the  $0^\circ$  region was not accompanied by a corresponding increase of the co-polarization level in the same region. In fact, Figure 2.8 shows that, in the  $0^\circ$  region, the co-polarization levels for the box and the sphere heads were also lower than those for the free-space head, whereas, in the  $180^\circ$  region, the co-polarization levels were about the same for all three simulated heads.

A possible reason for the fact that the co-polarization levels in Figure 2.8, were lower in the  $0^\circ$  region, but about the same in the  $180^\circ$  region, for the box and the sphere heads compared to those for the free-space head, is that for the  $0^\circ$  region, the transmitter laid behind the lossy head so that the wave propagating toward the receive horn was partly absorbed as it propagated through the lossy head. In contrast, for the  $180^\circ$  region, the transmitter was unobstructed by these same lossy heads. The co-polarization curves for the vertical orientation shown in Figure 2.8 and for the

edge orientation shown in Figure 2.11 are seen to be very similar between the various simulated heads in the range of angles for which the transmitter was not obstructed by the box or the sphere heads, i.e. about  $180^\circ$  for the vertical orientation and about  $+90^\circ$  for the edge orientation. However, the co-polarization curves for the flat orientation shown in Figure 2.9 presents some larger difference between the various simulated heads even though the transmitter was never obstructed by the presence of a lossy head.

Surprising also is the observation from Figures 2.3, 2.5, 2.9 and 2.11, that the bottom end of the metallic case radiates more than the antenna end of the metallic case. This suggests that the transmitter acts somewhat as a center-fed dipole with one half of the dipole, the case, being very fat compared to the other half, the monopole.



## Chapter 3

# Comparison Between Predicted and Measured Data

### 3.1 Generalities

The measured results were compared with the predicted results. The predicted values for the first and the second tests were obtained from a NEC-4 simulation (see Reference [5]) and a FDTD simulation (see Reference [6]), respectively. The comparison was based on taking the difference between a measured plot corrected by a constant scaling factor and the corresponding predicted plot. The scaling factor accounted for the difference between the radiated power level during the simulation and the radiated power level during the measurement. This factor was obtained as the linear average of two overall scaling factors in dB (or equivalently, as the geometrical average of these two scaling factors on a linear scale), one overall factor for each polarization. Hence, in Figures 3.1 to 3.18, the same value of the scaling factor is shown for both polarizations of a same test run; the value of the scaling factor, however, might have varied between different test runs for a same simulated head because the battery packs were either changed between runs or discharging at different rates during consecutive runs. Each overall scaling factor was itself a linear average of many scaling factors, one factor for every angular increment, each factor having been obtained as the difference on a dB scale between the measured and the predicted results.

A variable offset angle was also added to the azimuth angle of the measured data. The value of this offset was so selected as to minimize the absolute difference value between the predicted and the measured data. The minimization process was performed on the co-polarized signal unless this signal offered little variation. In this latter case, the minimization process was performed on the cross-polarized signal, thereby attempting to align the sharp nulls of the measured and the predicted data. For the cases of the transmitter in the presence of a simulated head, the sequence progression of the predicted data needed to be reversed for the  $\phi = 0^\circ$  and the  $\phi = 90^\circ$  cuts, in order to take into account the difference between the coordinate system used for the simulation and that used for the measurement.

In all figures of this chapter, the horizontal axis represents the measurement angle and the values range from  $0^\circ$  to  $360^\circ$  rather than from  $-180^\circ$  to  $+180^\circ$ . The angle corresponds to the  $\phi$  angle for the vertical orientation but to the  $\theta$  angle for the flat and the edge orientations. Since, however,  $\theta$  is defined only from  $0^\circ$  to  $180^\circ$  in the spherical coordinate system, the values of the horizontal axis from  $180^\circ$  to  $360^\circ$  correspond rigorously to  $\theta$  varying from  $180^\circ$  to  $0^\circ$  for the opposite  $\phi$  cut, i.e. the  $\phi = 180^\circ$  cut instead of the  $0^\circ$  cut for the flat orientation, and the  $\phi = 270^\circ$  cut instead of the  $90^\circ$  cut for the edge orientation.

The mapping of the measured data from the angular range  $\alpha = \{-180^\circ, +180^\circ\}$  to the angular range  $\beta = \{0^\circ, 360^\circ\}$  was performed by using the "modulo" function with the FORTRAN code  $\beta = \text{AMOD}(\alpha + 360.0, 360.0)$ . Thus, both  $\alpha = -180^\circ$  and  $\alpha = +180^\circ$  were mapped to the same  $\beta = 180^\circ$  whereas no value of  $\alpha$  was mapped to  $\beta = 360^\circ$ . Since the power level varied during measurement, the data for  $\alpha = -180^\circ$  was not identical to the data for  $\alpha = +180^\circ$ , unless power correction was subsequently applied to the measured data (herein, power correction was always applied except for the first test because the data corresponding to  $\alpha = -180^\circ$  was not trustworthy as a result of some data buffer not having been cleared before the data acquisition). The value corresponding to  $\alpha = +180^\circ$  was the one retained as the value corresponding to  $\beta = 180^\circ$  and the value corresponding to  $\alpha = 0^\circ$  was used for both angles  $\beta = 0^\circ$  and  $\beta = 360^\circ$ .

The near-to-far field transformation did not account for the difference between

the placement of the origin in the simulation (all objects having been modelled in the first octant with respect to the origin in the FDTD simulation) and the placement of the origin at the pivot point of the azimuth table in the measurement setup. As with the different location of the antenna between the first and the second tests, the different placement of the origin between the FDTD simulation and the measurement setups incurred a variation of the power level and a variation of the angle of arrival (see Appendix C) as the azimuth table was rotated. Since these variations were not accounted for in the simulation, they explain in part the discrepancy between the measured and the predicted data. Another systematic error affecting the simulation data lies in the slight modelling error arising from approximating the geometry and the placement of the various objects with an integer number of cells. Furthermore, the FDTD simulation model did not include the presence of the styrofoam, fiberglass threaded rods and nuts, and plexiglass washers.

### 3.2 Plots

This section presents all the magnitude plots for the comparison.

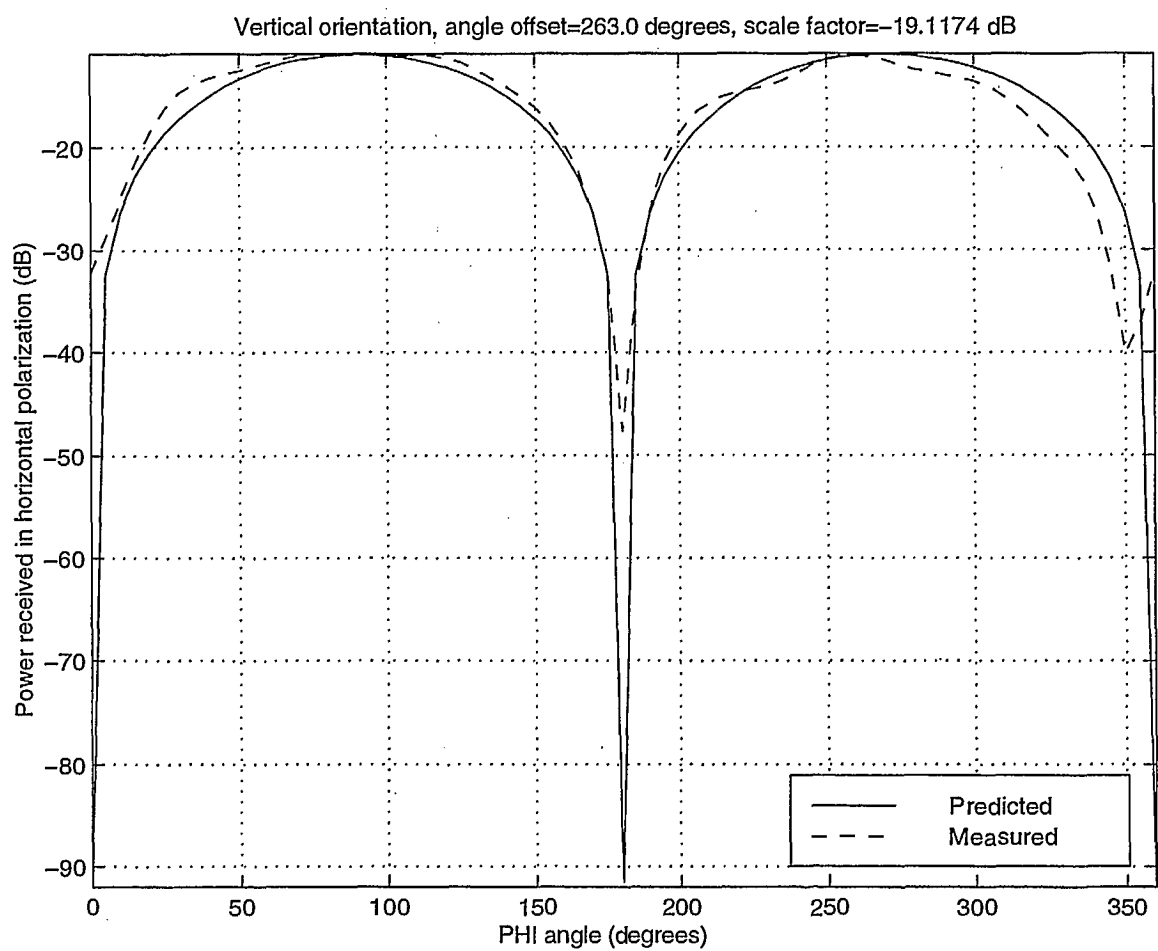


Figure 3.1: Comparison between the magnitudes of the predicted and measured horizontal polarization for the  $\theta = 90^\circ$  orientation of the first test.



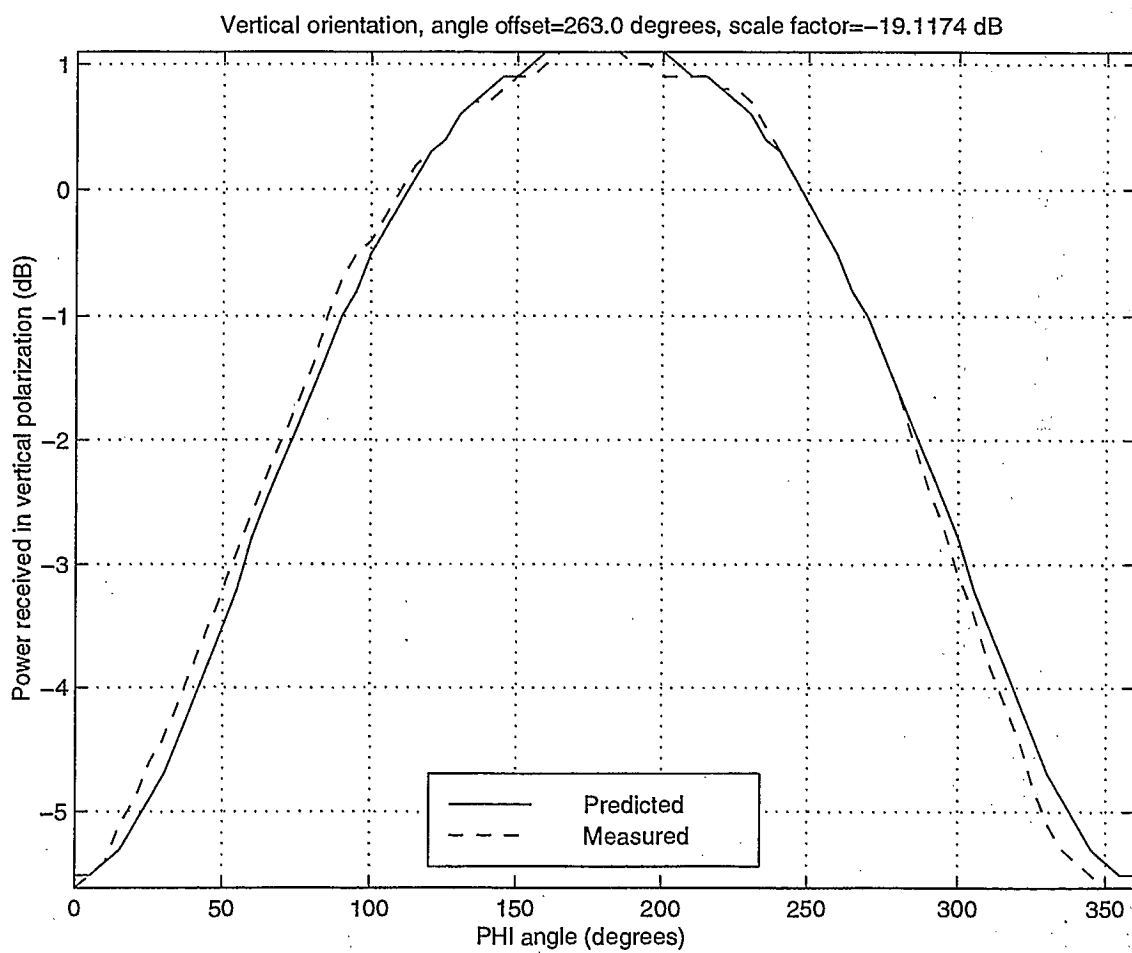


Figure 3.2: Comparison between the magnitudes of the predicted and measured vertical polarization for the  $\theta = 90^\circ$  orientation of the first test.

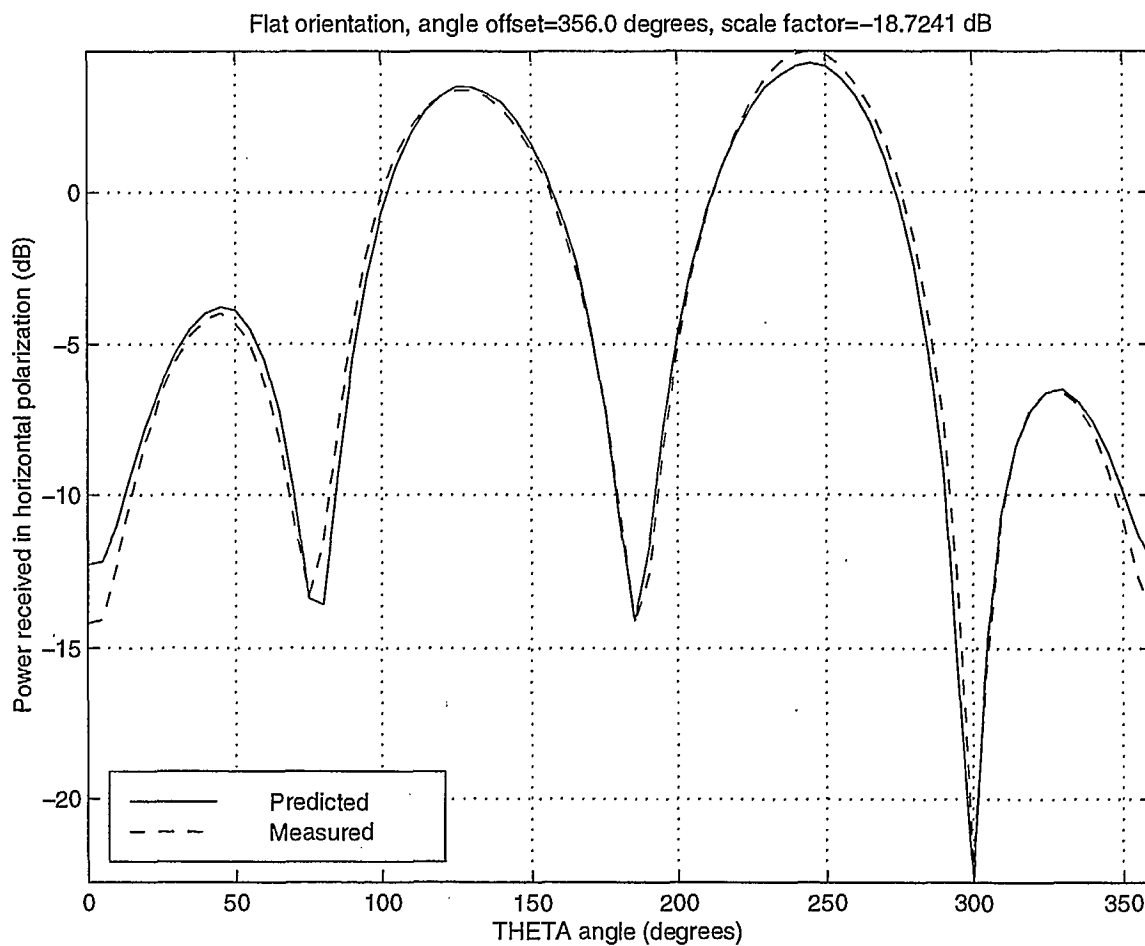


Figure 3.3: Comparison between the magnitudes of the predicted and measured horizontal polarization for the  $\phi = 0^\circ$  orientation of the first test.

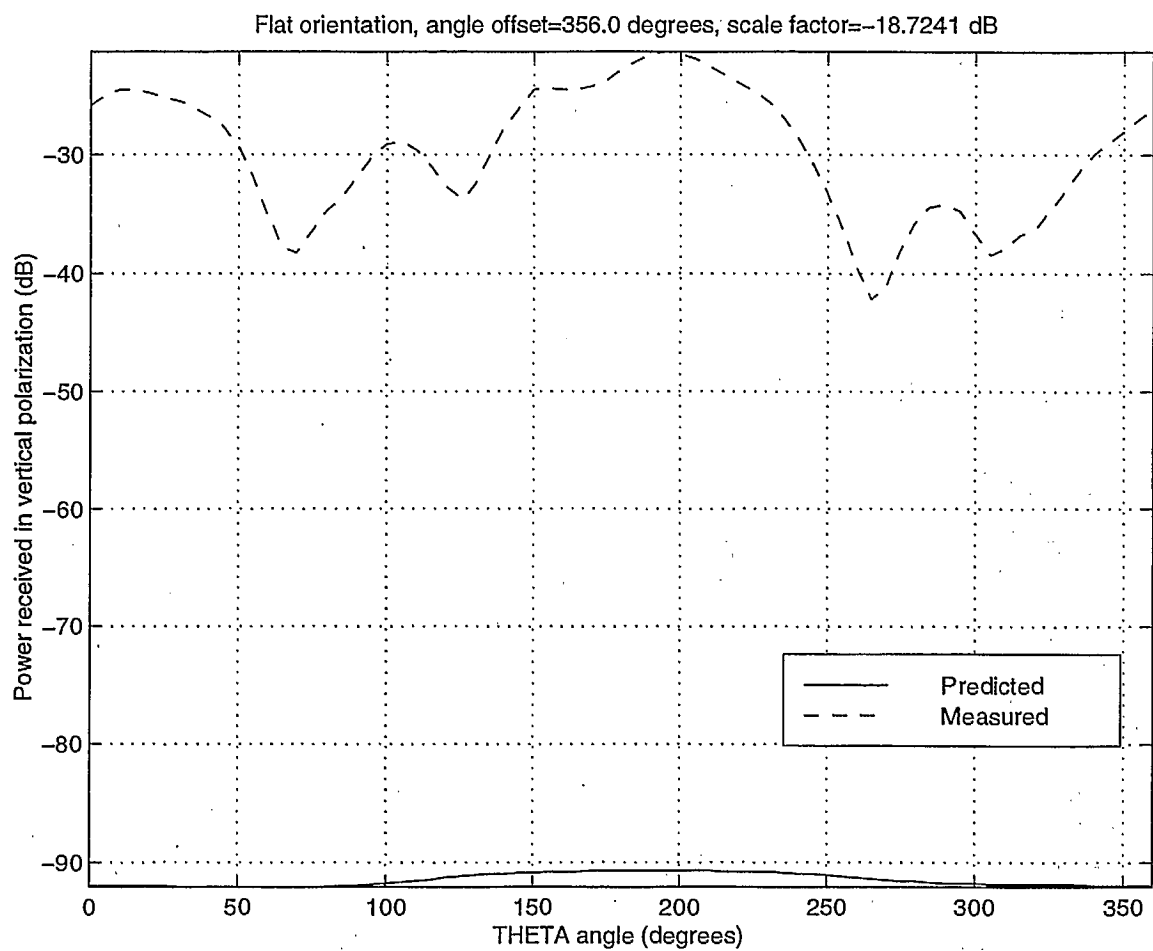


Figure 3.4: Comparison between the magnitudes of the predicted and measured vertical polarization for the  $\phi = 0^\circ$  orientation of the first test.

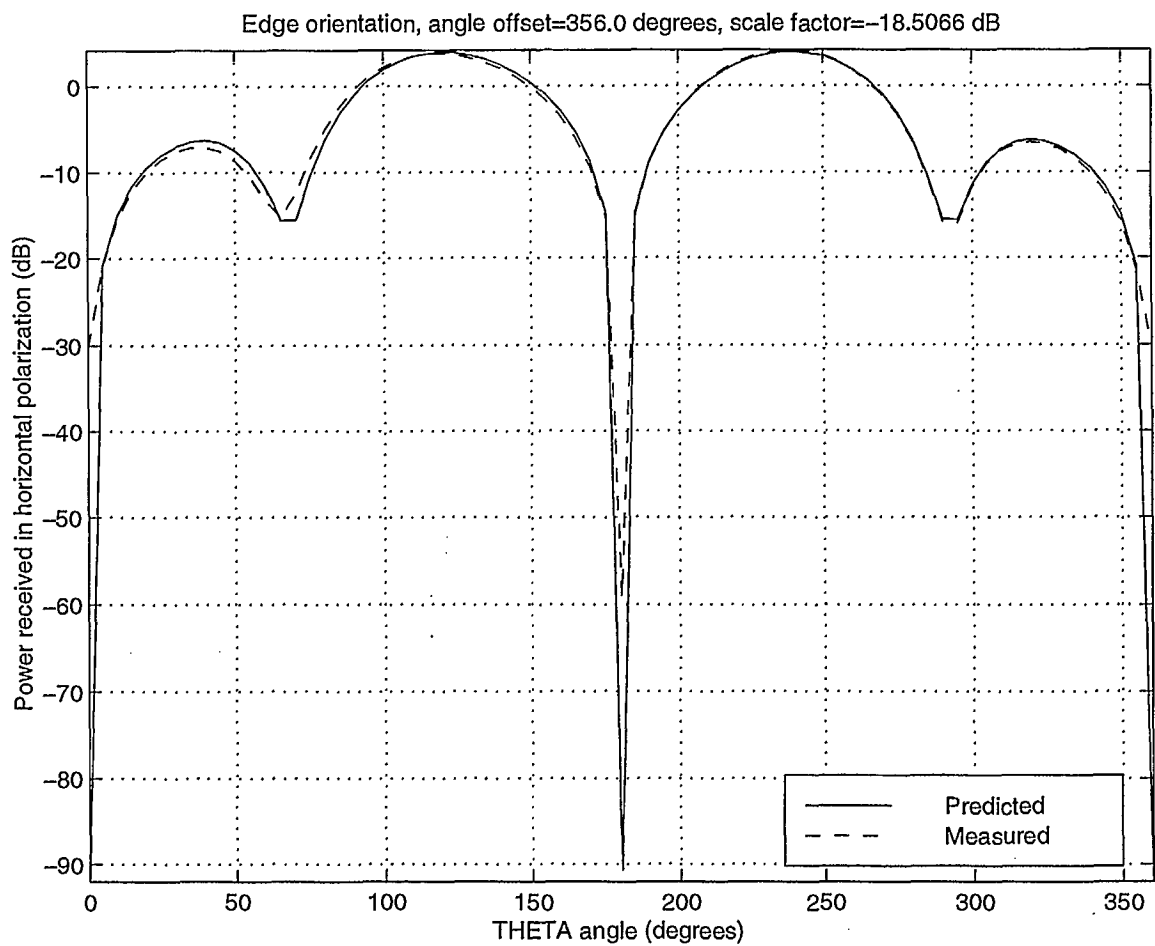


Figure 3.5: Comparison between the magnitudes of the predicted and measured horizontal polarization for the  $\phi = 90^\circ$  orientation of the first test.



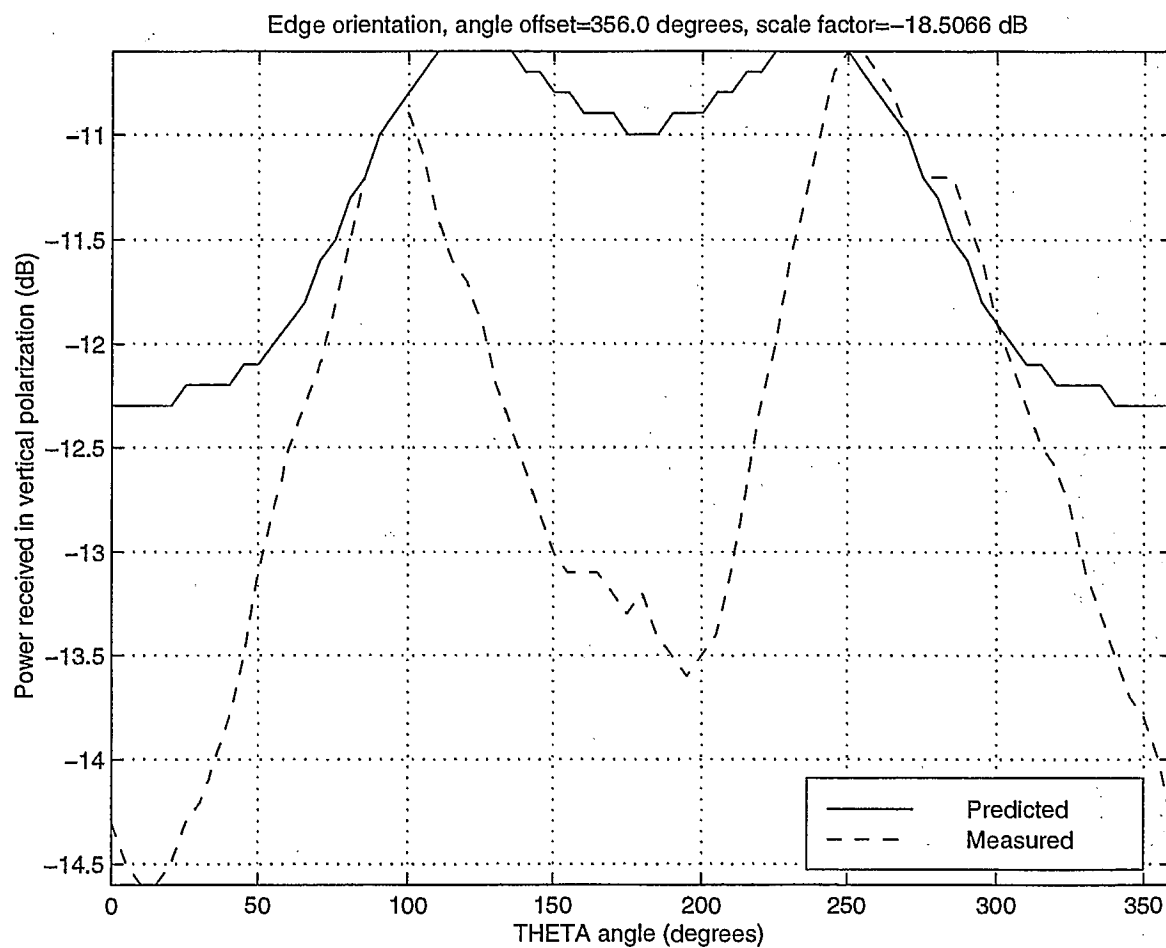


Figure 3.6: Comparison between the magnitudes of the predicted and measured vertical polarization for the  $\phi = 90^\circ$  orientation of the first test.

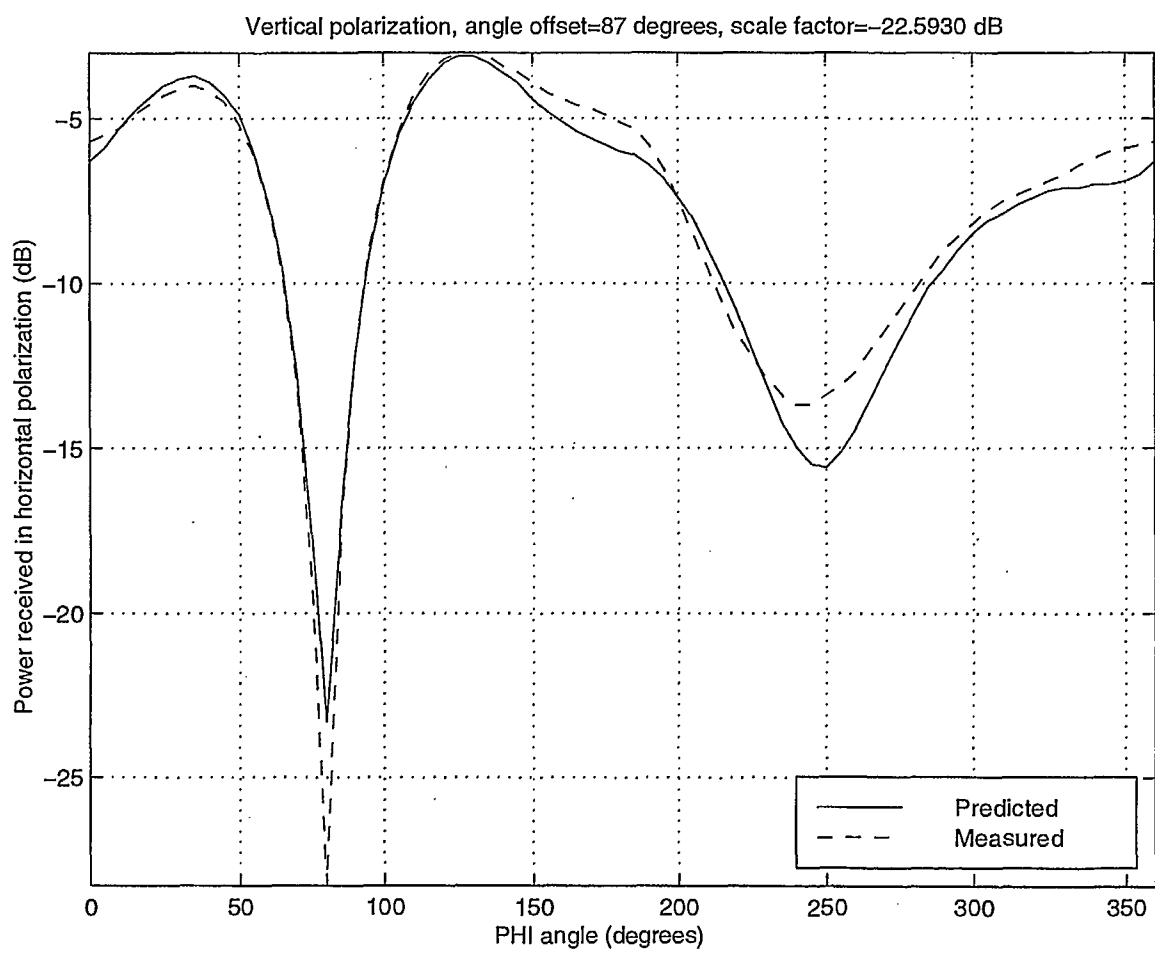


Figure 3.7: Comparison between the magnitudes of the predicted and measured horizontal polarization for the  $\theta = 90^\circ$  orientation of the second test with the box head.

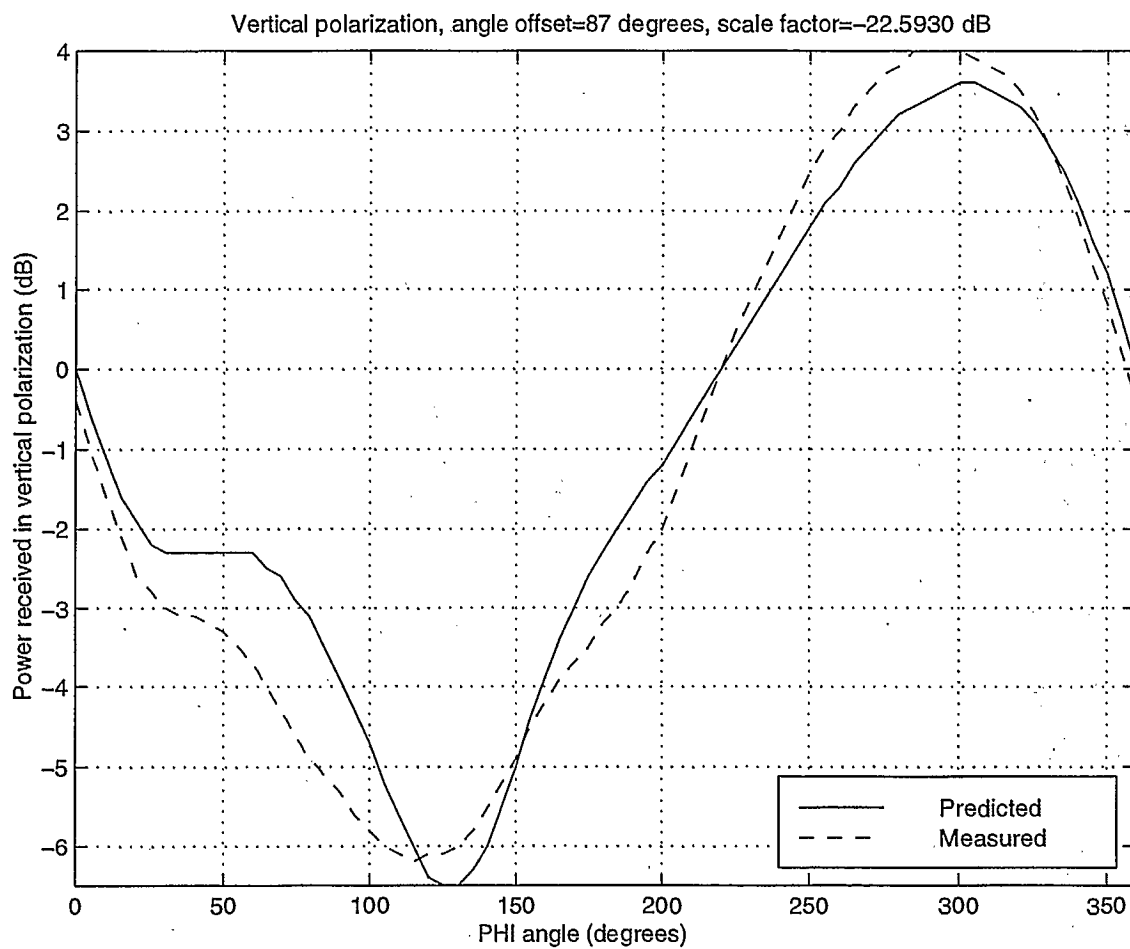


Figure 3.8: Comparison between the magnitudes of the predicted and measured vertical polarization for the  $\theta = 90^\circ$  orientation of the second test with the box head.

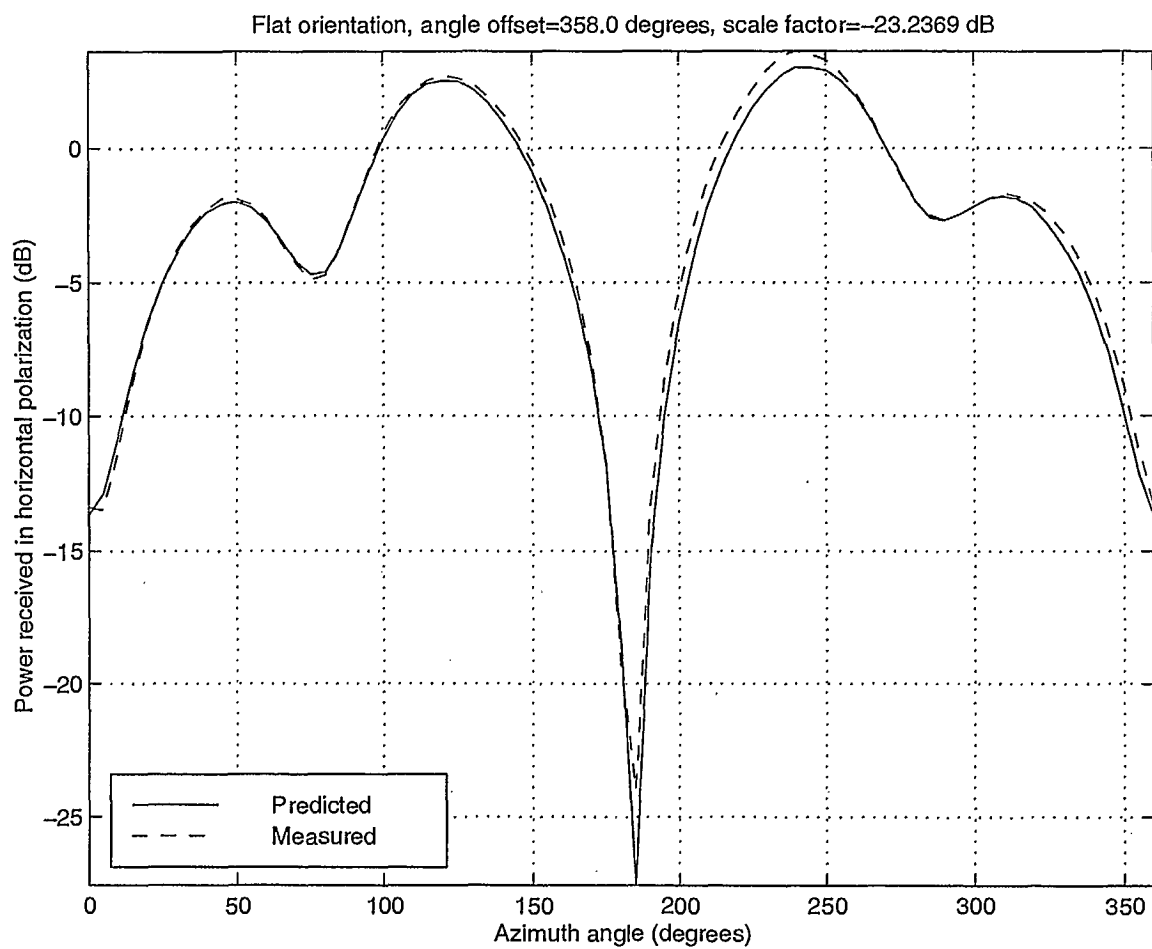


Figure 3.9: Comparison between the magnitudes of the predicted and measured horizontal polarization for the  $\phi = 0^\circ$  orientation of the second test with the box head.

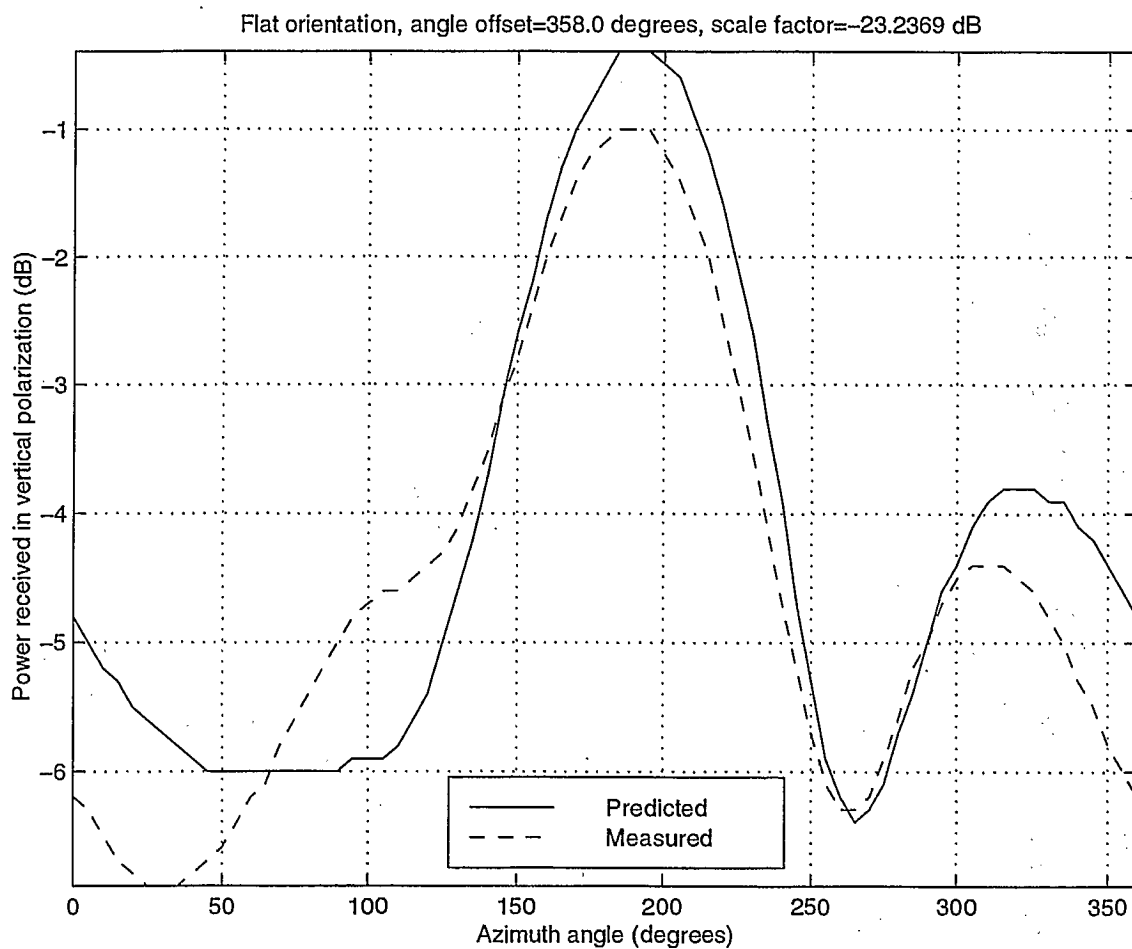


Figure 3.10: Comparison between the magnitudes of the predicted and measured vertical polarization for the  $\phi = 0^\circ$  orientation of the second test with the box head.



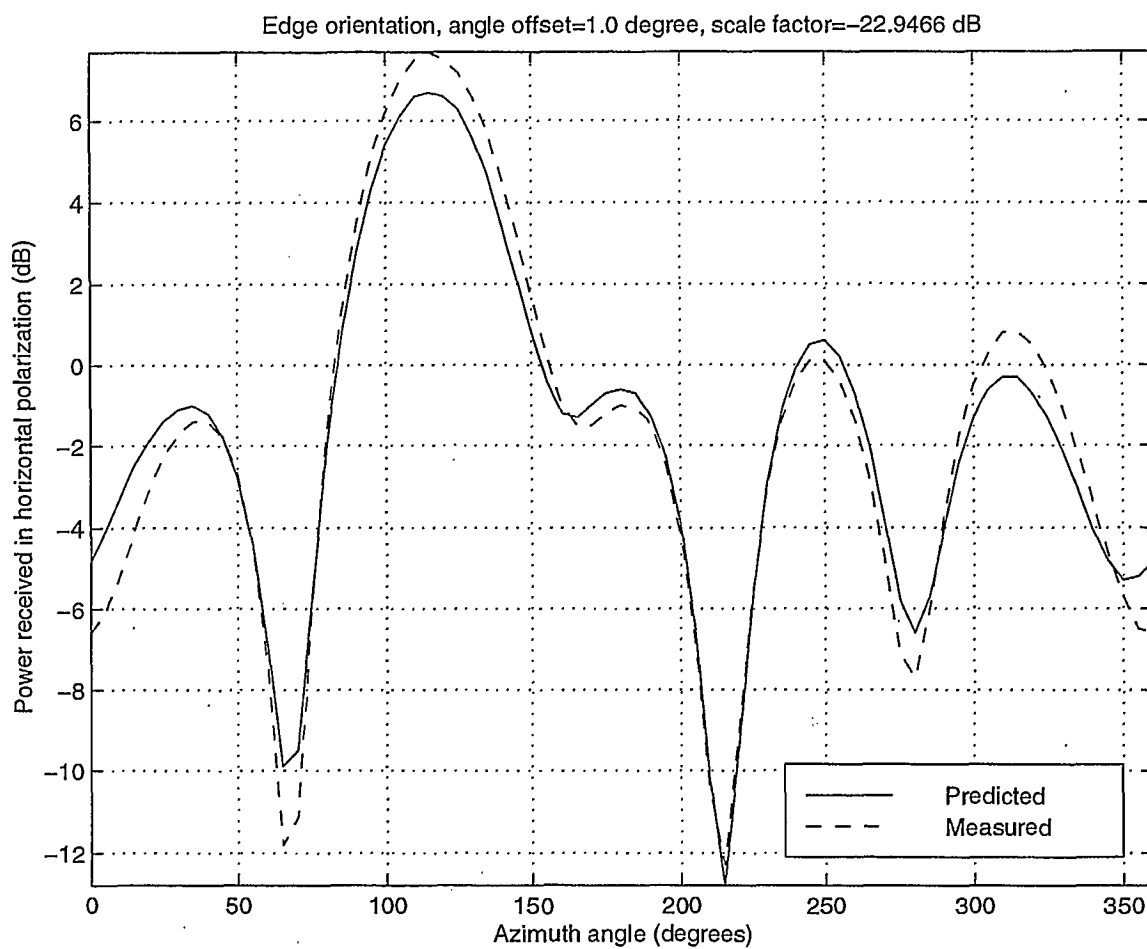


Figure 3.11: Comparison between the magnitudes of the predicted and measured horizontal polarization for the  $\phi = 90^\circ$  orientation of the second test with the box head.

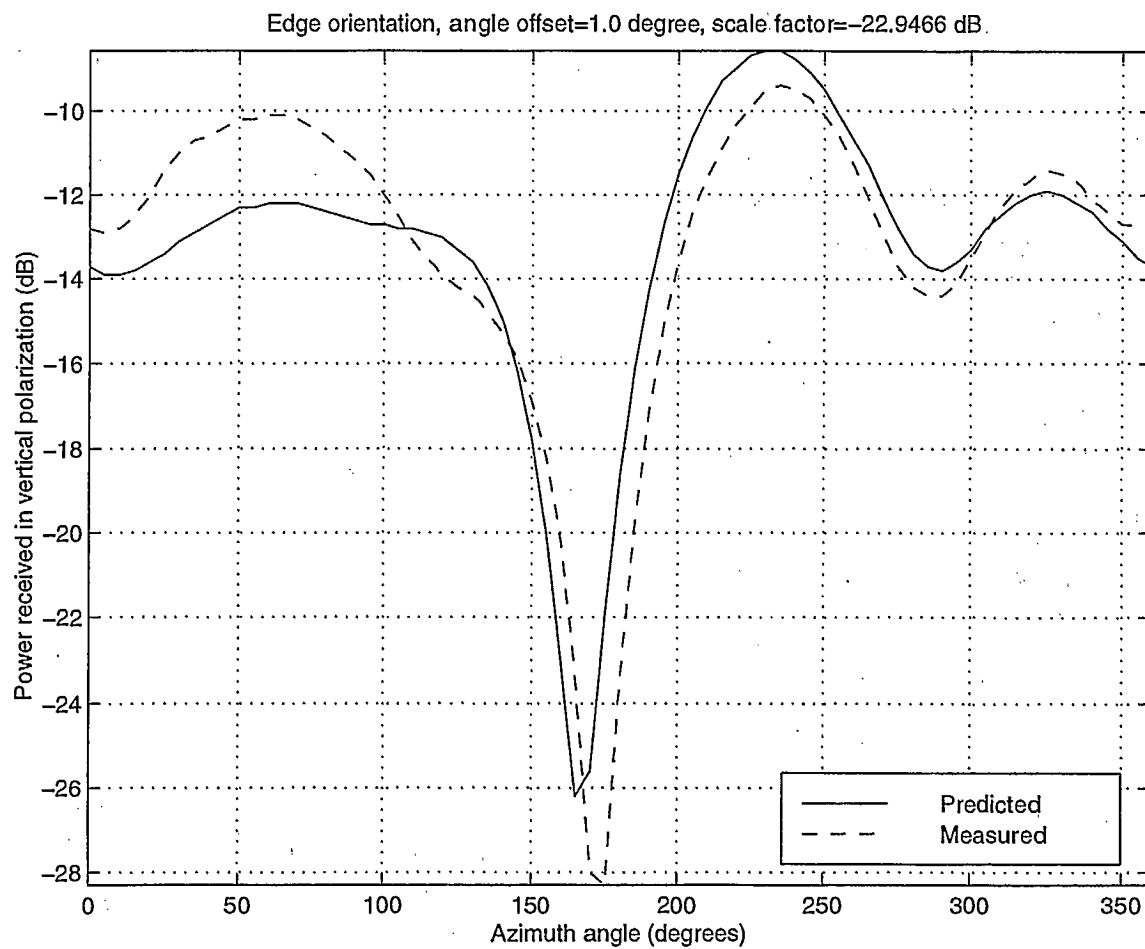


Figure 3.12: Comparison between the magnitudes of the predicted and measured vertical polarization for the  $\phi = 90^\circ$  orientation of the second test with the box head.

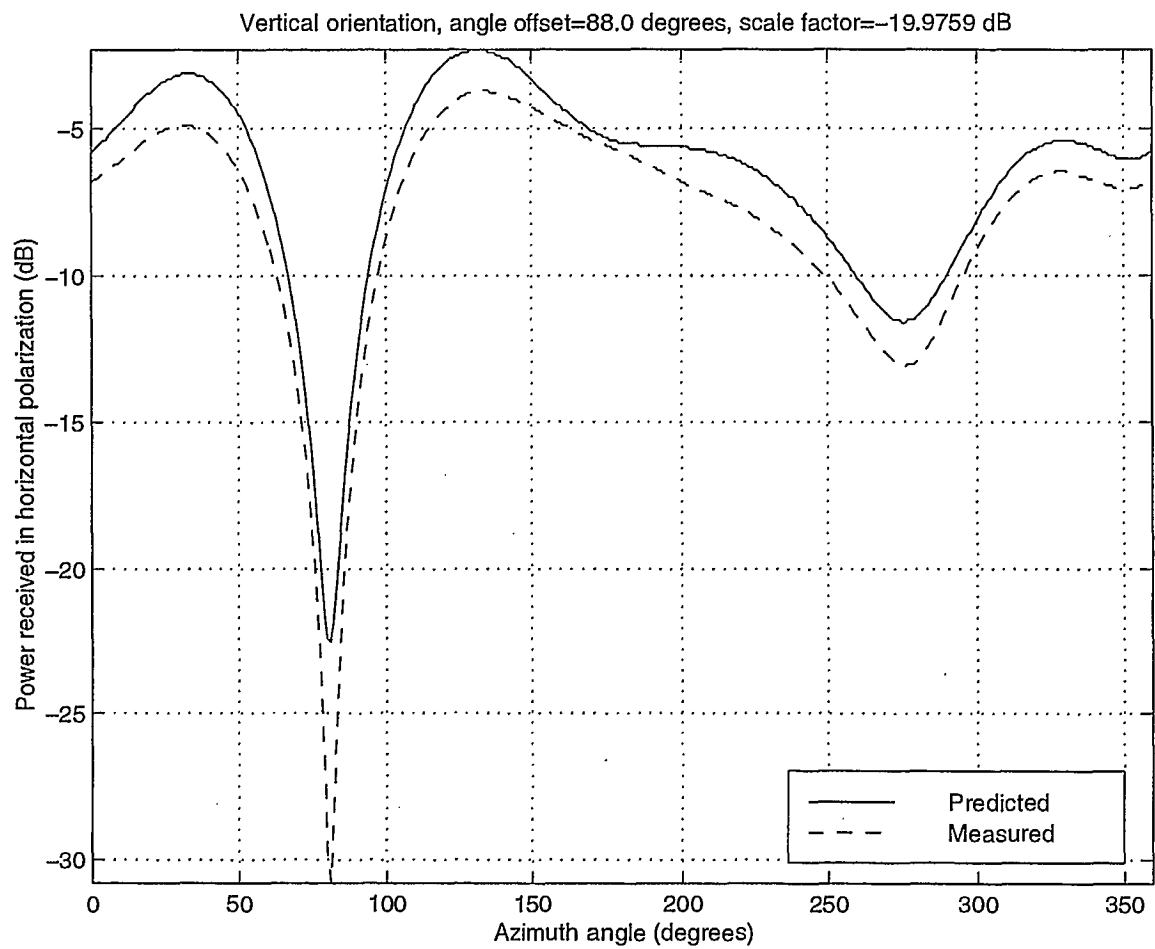


Figure 3.13: Comparison between the magnitudes of the predicted and measured horizontal polarization for the  $\theta = 90^\circ$  orientation of the second test with the sphere head.

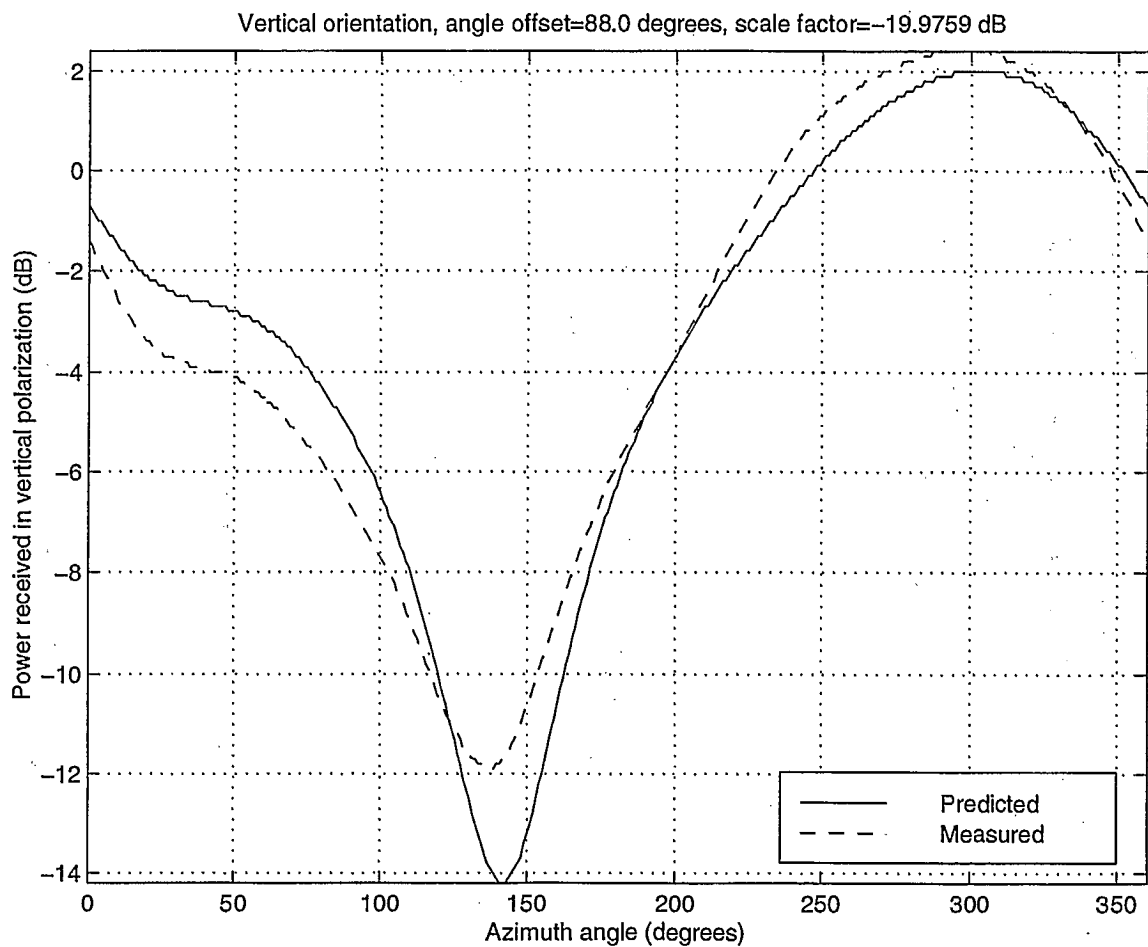


Figure 3.14: Comparison between the magnitudes of the predicted and measured vertical polarization for the  $\theta = 90^\circ$  orientation of the second test with the sphere head.

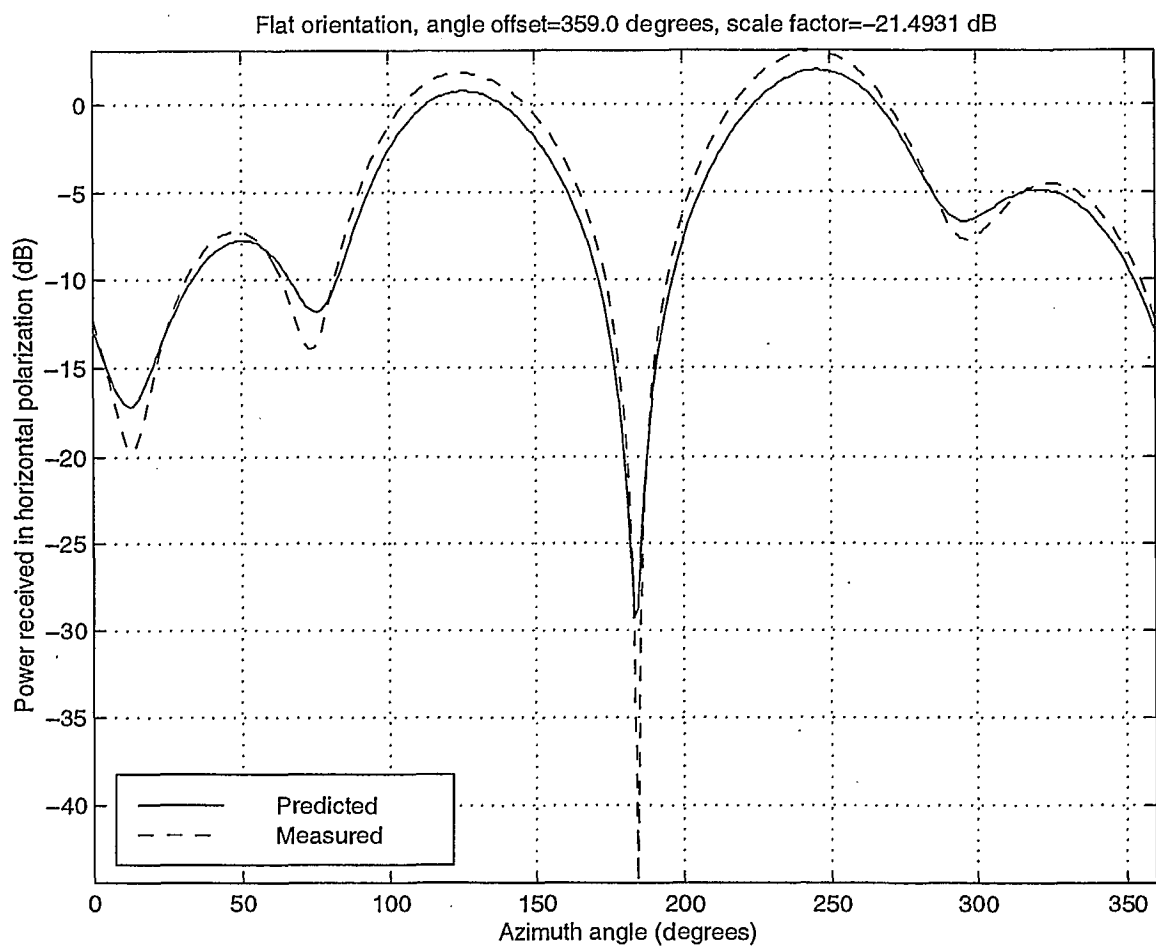


Figure 3.15: Comparison between the magnitudes of the predicted and measured horizontal polarization for the  $\phi = 0^\circ$  orientation of the second test with the sphere head.



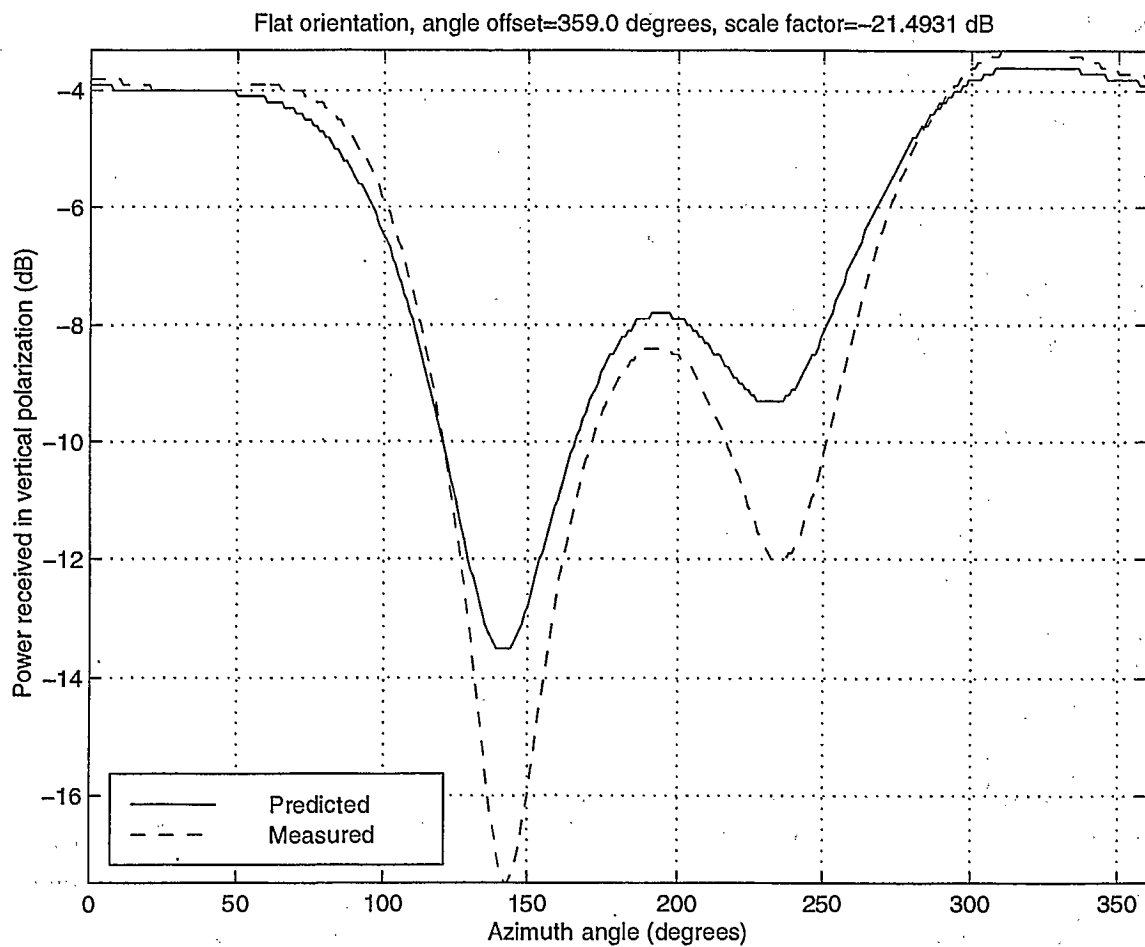


Figure 3.16: Comparison between the magnitudes of the predicted and measured vertical polarization for the  $\phi = 0^\circ$  orientation of the second test with the sphere head.

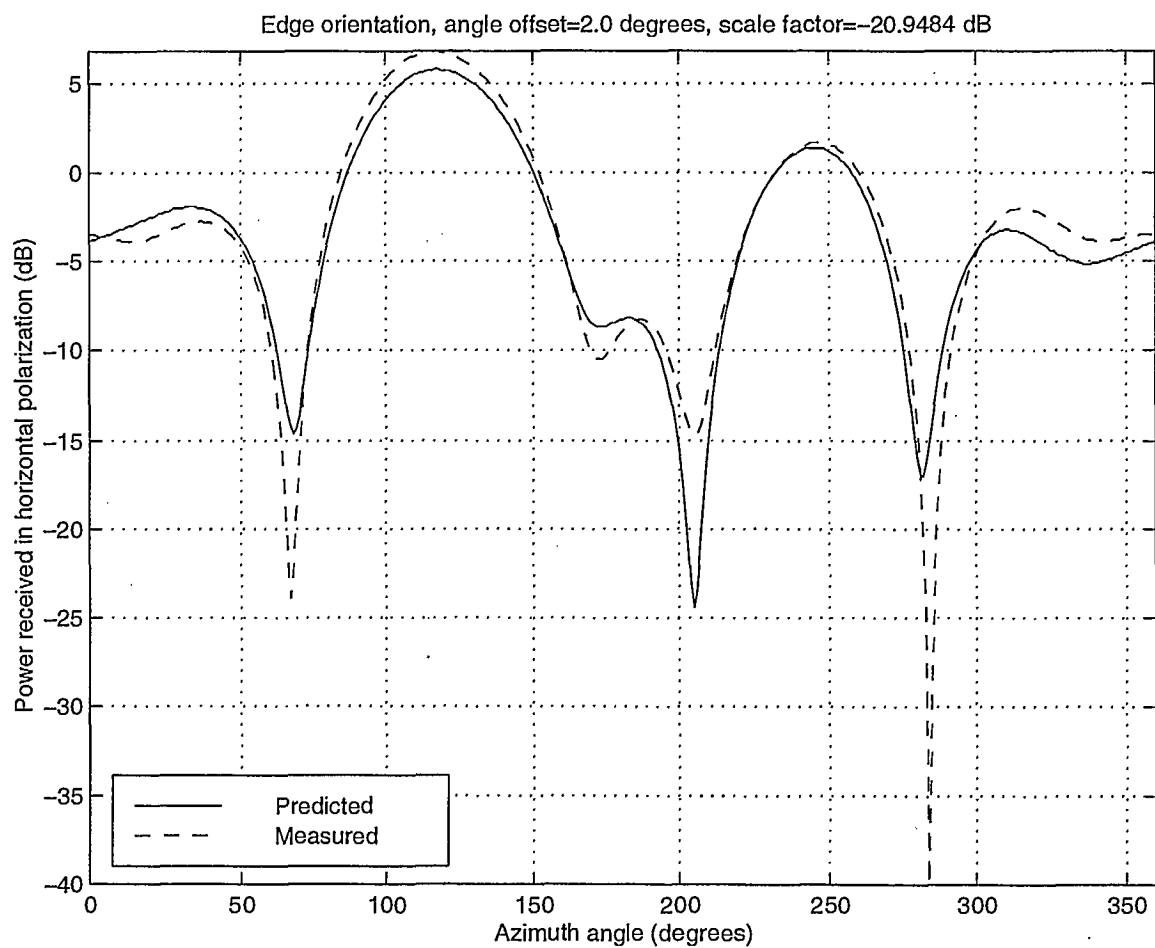


Figure 3.17: Comparison between the magnitudes of the predicted and measured horizontal polarization for the  $\phi = 90^\circ$  orientation of the second test with the sphere head.

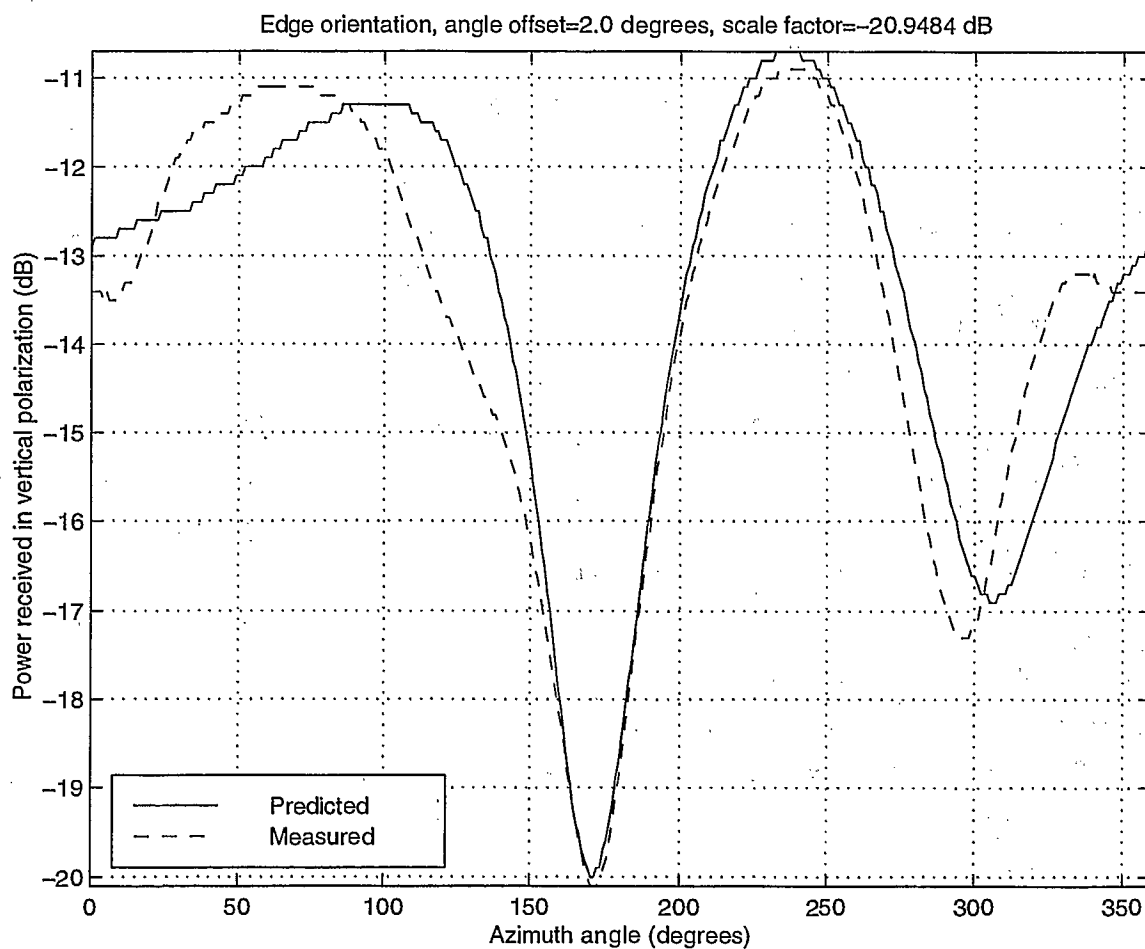


Figure 3.18: Comparison between the magnitudes of the predicted and measured vertical polarization for the  $\phi = 90^\circ$  orientation of the second test with the sphere head.

### 3.3 Discussion

For the transmitter alone, the comparison held very well for all curves except the cross-polarized result (i.e. vertical= $\phi$  direction) for the flat (i.e.  $\phi = 0^\circ$ ) orientation. For this latter case (see Figure 3.4), the measured data showed a cross-polarization level of about -30 dB while the predicted data showed about -90 dB. It is not known how much the reflections off the walls of the chamber contributed to this discrepancy. Figure 3.6 also shows some discrepancy but the scale of the plot is highly magnified.

For the transmitter with the box or the sphere heads, there was an  $87^\circ$  and  $88^\circ$  shift between the predicted and the measured plots, respectively, because in the measurement, the orientation of the transmitter was kept the same as in the test for the transmitter alone, in order to assess quickly the effect of the presence of the simulated head (see Figures 1.12 and 1.13). The simulation, however, was carried out with the operator facing the  $-x$  direction of Figure 1.13. That difference accounted for a  $90^\circ$  rotation. There was also about  $0.6^\circ$  uncertainty in aligning the styrofoam assembly on top of the pylon. The excess angular discrepancy might have come from the process of choosing the offset angle that minimized the difference between the predicted and the measured plots. All figures for the box or the sphere heads show clearly that both the predicted and the measured data followed the same trend. Hence, qualitatively, the comparison on a relative basis held very well. Quantitatively, the comparison was only slightly poorer for a simulated head than for the case of the transmitter alone.

## Chapter 4

### Conclusion

This report has presented the measurement setup and the measurement results for the far field radiated in the principal planes by a portable transmitter when the transmitter was alone or in the presence of a simulated head. The comparison between the measured data and the data predicted by FDTD or NEC simulations was seen to be good qualitatively for both the co-polarization and the cross-polarization, albeit the comparison was carried out only on a relative basis.



## REFERENCES

- [1] R.M.T. Milne, Description And Calibration of the CRC R.F. Test Facility, Unclassified Technical Memorandum, Serial No. DFL-102, 1 May 1975.
- [2] J.M. Bertrand and W.R. Lauber, CRC Model Transmitter, Technical Memorandum VPRB-05-97, CRC, Ottawa, May 1997.
- [3] G. Hartsgrove, A. Kraszewski, and A. Surowiec, "Simulated Biological Materials for Electromagnetic Radiation Absorption Studies", Bioelectromagnetics, Vol. 8, 1987, pp. 29-36.
- [4] Joseph Seregelyi, CRC, Ottawa, private communication.
- [5] C.W. Trueman, S.J. Kubina and M. Danesh, Fields of a Portable Radio Handset Near the Human Head - Phase I, Final Report, Public Works and Government Services Canada, Communications Research Centre, Contract #PWGSC/CRC 67CRC-5-0850/01-ST, Technical note TN-EMC-96-01, ECE Dept., Concordia University, March 31, 1996, 149 pages.
- [6] C.W. Trueman, EMC Laboratory, University of Concordia, private communication.

## Appendix A

### Gain Measurement of the Receive Horn

The gain for the receive horn (quad-ridged horn from Condor Systems, Model As 48450, Part #637542-001) was measured by the two antenna method. This method consists in determining the unknown gain of an antenna by measuring the power transferred between this antenna and another antenna, then computing the unknown gain from the knowledge of the gain for the second antenna while taking into account the propagation loss between the two antennas, the loss through the cables and the reflection loss from the antennas. It was assumed herein that the two antennas were perfectly linearly polarized and perfectly aligned at their respective boresight, and that the characteristic impedance of all cables and measuring equipment was 50 Ohms. Only the vertical polarization channel of the quad-ridged horn was measured since neither the horn with known gain (Scientific Atlanta standard gain horn, Model 12-0.75, 0.75-1.12 GHz) nor the quad-ridged horn could readily be rotated by 90° for measuring the horizontal polarization channel of the quad-ridged horn. However, it is safe to assume that the two channels of the quad-ridged horn have the same gain since this horn is symmetrical with respect to both the vertical and the horizontal planes. Figure A.1 depicts the diagram of the equipment setup.

The equations for the system are as follows:

$$\frac{P_R}{P_T} = \left( \frac{\lambda}{4\pi R} \right)^2 G_R G_T \implies \chi = 10 \log_{10} \left[ \frac{P_R}{P_T} \right] \quad (\text{A.1})$$

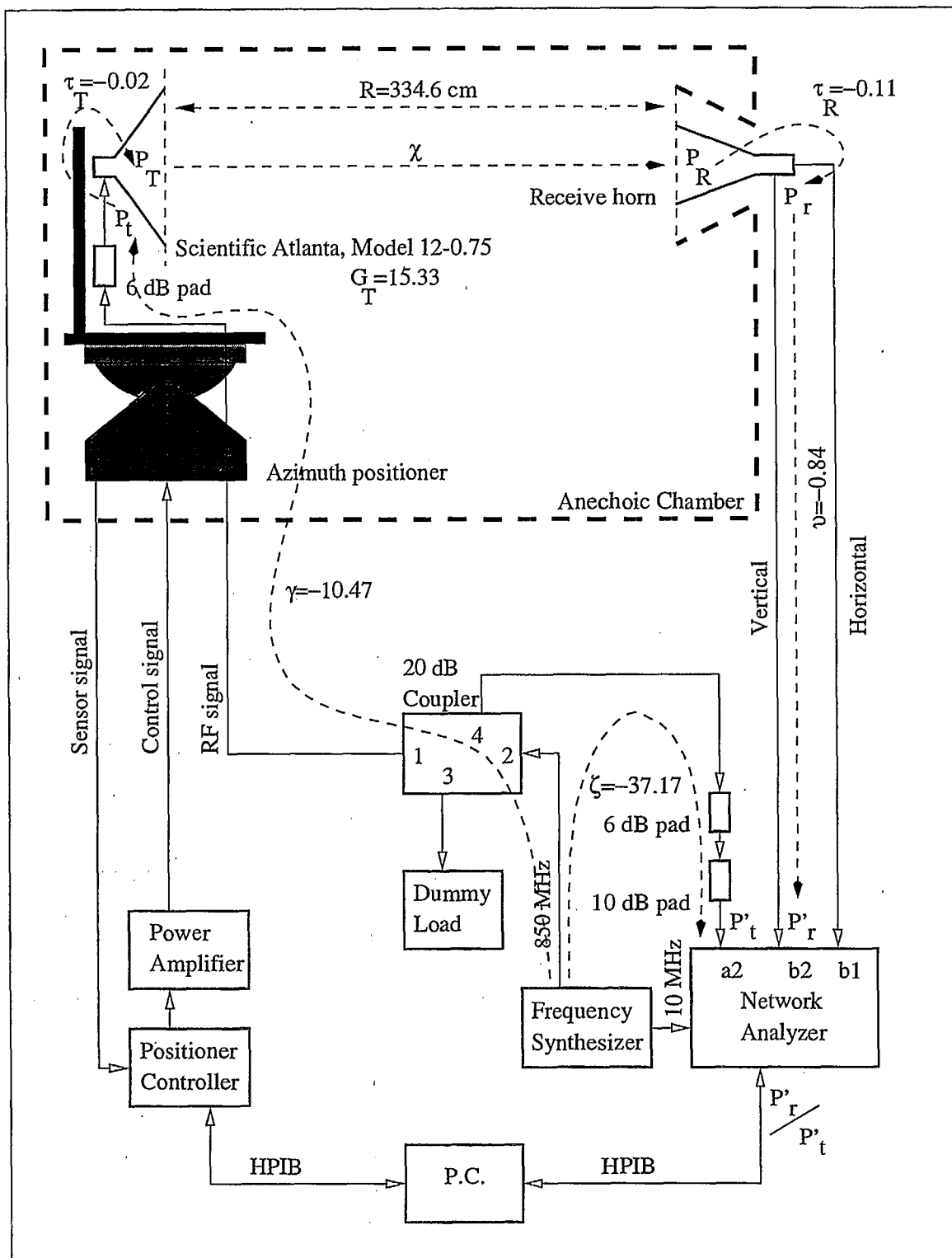


Figure A.1: The schematic diagram of the equipment setup for measuring the gain of the receive horn.

$$10 \log_{10} \left[ \frac{P'_R}{P'_T} \right] = (\gamma + \tau_T + \chi + \tau_R + \nu) - (\zeta) \quad (\text{A.2})$$

where  $P$  is the power level,  $\lambda = 0.353 \text{ m}$  is the wavelength corresponding to 850 MHz in free space,  $\tau = 1 - |\Gamma|^2$  with  $\Gamma$  being the reflection coefficient of the receive or transmit antenna as identified by the subscript, and  $\gamma$ ,  $\nu$  and  $\zeta$  are as shown on the diagram of Figure A.1.

The measured quantities were as follows:

$$R = 334.6 \text{ cm} \implies 10 \log_{10} \left[ \left( \frac{\lambda}{4\pi R} \right)^2 \right] = -41.53 \text{ dB}$$

$$10 \log_{10} \left[ \frac{P'_R}{P'_T} \right] = 8.55 \text{ dB}$$

$$20 \log_{10} [|\Gamma_T|] = -22.80 \text{ dB} \implies \tau_T = 10 \log_{10} [1 - |\Gamma_T|^2] = -0.02 \text{ dB}$$

$$\gamma = -10.47 \text{ dB}$$

$$\nu = -0.84 \text{ dB}$$

$$\zeta = -37.17 \text{ dB}$$

The measurement of the quantities  $\gamma$  and  $\Gamma_T$  required the use of a long coaxial cable that was included as part of the calibration setup of the network analyzer. This long coaxial cable was required to reach the transmit horn mounted on the positioner from the position of the network analyzer located outside the anechoic chamber.

The quantities obtained from manufacturers' data were as follows:

$$20 \log_{10} [|\Gamma_R|] \approx 15.0 \text{ dB} \implies \tau_R = 10 \log_{10} [1 - |\Gamma_R|^2] = -0.14 \text{ dB}$$

$$10 \log_{10} [G_T] = 15.33 \text{ dB}$$

Therefore, the directivity (or lossless gain) of the quad-ridged horn became:

$$10 \log_{10} [G_R] = 9.05 \text{ dB}$$

and the corresponding maximum effective aperture area became:

$$A = \frac{\lambda^2}{4\pi} G_R = 0.080 \text{ m}^2$$

This value is to be compared with the physical aperture area of  $0.192 \text{ m}^2$ .



## Appendix B

### Transmitter Gain

In order to estimate the value of the impedance mismatch between the output impedance of the oscillator and the input impedance of the monopole antenna in situ, transformed through the length of the coaxial cable connecting the oscillator to the monopole antenna, the following procedure was used. The cover of the transmitter was removed, the oscillator was disconnected from the RF path, a network analyzer HP8753D was connected at the end of the coaxial cable that would normally connect to the oscillator port, and the open surface of the box was covered with conducting adhesive copper tape in such a way as to let the cable of the network analyzer come out of the metallic case at about the center point of the surface. The network analyzer was calibrated with its cable in place.

When the antenna was not in the near vicinity of objects with high dielectric constants or losses, the impedance value was found to be  $Z_{in}=84+j44$  Ohms which corresponded to a transmission loss of 1.01 dB. Therefore, it would be possible to compute the measured gain of the transmitter in the first test as follows. From the manufacturer's data sheet that came with the receive horn, the return loss was estimated to be about 15 dB at 850 MHz which corresponded to about 0.14 dB transmission loss. The gain of the transmitter thus became:

$$G_T(\text{dB}) = [P_R(\text{dBm}) - 0.14(\text{dB})] - [P_{in}(\text{dBm}) - 1.01(\text{dB})] - 20 \log_{10} \left[ \frac{\lambda}{4\pi R} \right] - G_R(\text{dB}) \quad (\text{B.1})$$

where  $R=334.6$  cm (or 131.75") for the first test, 331.5 cm (or 130.5") for the second

test,  $G_R = 9.05$  dB (see Appendix A),  $P_{in}$  is given in Table 2.3 and  $P_R$  is the measured power level.

Similarly, the transmitter gain could also be estimated with the transmitter radiating in the presence of a simulated head, provided that the impedance mismatch loss was known when the monopole antenna radiated in the presence of each simulated head. However, the impedance mismatch loss was not measured in the presence of a lossy head.

## Appendix C

### Transformation due to a Change of Origin

It would be possible to take into account the variation of the arrival angle at the receive horn by computing the far field for values of  $\theta$  and  $\phi$  that would correspond to the actual  $\theta$  and  $\phi$  values in the measurement, thereby accounting also for the rotation of the azimuth table and the difference in the placement of the origin of the coordinate system between the simulation and the measurement setups. For instance, the equations to obtain  $\theta^s$  and  $\phi^s$  in the FDTD coordinate system, given  $\theta$  and  $\phi$  in the measurement coordinate system and the location  $r'$ ,  $\theta'$  and  $\phi'$  for the origin of the FDTD coordinate system in terms of the measurement coordinate system, are as follows:

$$\theta^s = \text{Arccos} \left( \frac{r \cos(\theta) - r' \cos(\theta')}{D} \right) \text{ where}$$

$$D = \sqrt{r^2 + r'^2 - 2rr' [\sin(\theta)\sin(\theta')\cos(\phi - \phi') + \cos(\theta)\cos(\theta')]}$$

$$\phi^s = \phi' - \text{Arccos} \left( \sqrt{\frac{V}{W}} \right) \text{ where}$$

$$V = (r' \sin(\theta'))^2 + (r \sin(\theta))^2 \cos^2(\phi - \phi') - 2(r' \sin(\theta'))(r \sin(\theta)) \cos(\phi - \phi')$$

$$W = (r' \sin(\theta'))^2 + (r \sin(\theta))^2 - 2(r' \sin(\theta'))(r \sin(\theta)) \cos(\phi - \phi')$$

and the square root operator is double valued.

Assuming a thickness of 2 cells between the handset and the outer wall of the plexiglass box and assuming a spacing of 20 white cells between the handset and the absorbing boundary, the center of the box head, which is also the center of the styrofoam assembly, would be located at  $x = 40\Delta l$ ,  $y = 43\Delta l$  and  $z = 45\Delta l$  with  $\Delta l = 0.441$  cm, thus there obtains:

$$\left. \begin{array}{l} x' = -17.64 \text{ cm} \\ y' = -18.96 \text{ cm} \\ z' = -19.85 \text{ cm} \end{array} \right\} \Rightarrow \left\{ \begin{array}{l} r' = 32.63 \text{ cm} \\ \theta' = 180^\circ - \text{Arccos} \left( \frac{19.85}{32.63} \right) = 127.46^\circ \\ \phi' = \text{Arctan} \left( \frac{-18.96}{-17.64} \right) = 227.07^\circ \end{array} \right.$$

Assuming now that the azimuth table is in a position corresponding to having:

$$\left. \begin{array}{l} r = 331.5 \text{ cm} \\ \theta = 56.0^\circ \\ \phi = 90.0^\circ \end{array} \right\} \Rightarrow \left\{ \begin{array}{l} x = 331.5 \sin(56^\circ) \cos(90^\circ) = 0 \text{ cm} \\ y = 331.5 \sin(56^\circ) \sin(90^\circ) = 274.83 \text{ cm} \\ z = 331.5 \cos(56^\circ) = 185.37 \text{ cm} \end{array} \right.$$

there obtains:

$$\left. \begin{array}{l} r^s = 358.80 \text{ cm} \\ D = 358.80 \end{array} \right\} \Rightarrow \theta^s = 55.11^\circ$$

$$\left. \begin{array}{l} V = 51584.88 \\ W = 86623.12 \end{array} \right\} \Rightarrow \phi^s = 227.07^\circ - \left\{ \begin{array}{l} 140.51^\circ \\ 39.49^\circ \end{array} \right. = \left\{ \begin{array}{l} 86.56^\circ \\ 187.58^\circ \end{array} \right.$$

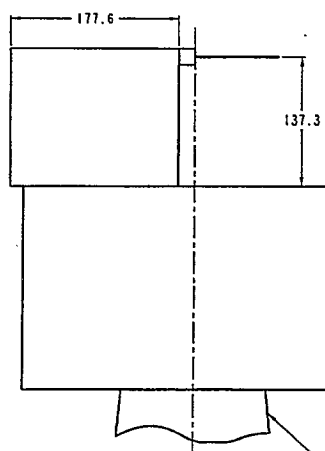
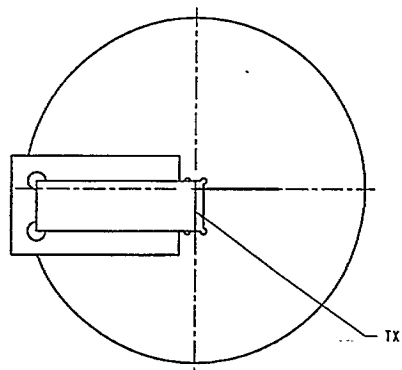
The second solution corresponds to the positive value of the square root  $\sqrt{V/W}$  but is to be rejected here. Hence  $\phi^s = 86.56^\circ$ .

So, we see that there is a significant difference between  $\theta = 56.0^\circ$  and  $\theta^s = 55.11^\circ$ , as well as between  $\phi = 90.0^\circ$  and  $\phi^s = 86.56^\circ$ . This example, which does not even correspond to the worst case, demonstrates the importance of taking into account the difference in the placement of the origin of the coordinate system between the simulation and the measurement setups.

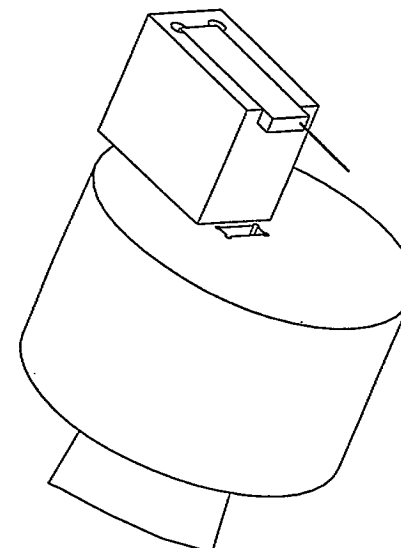
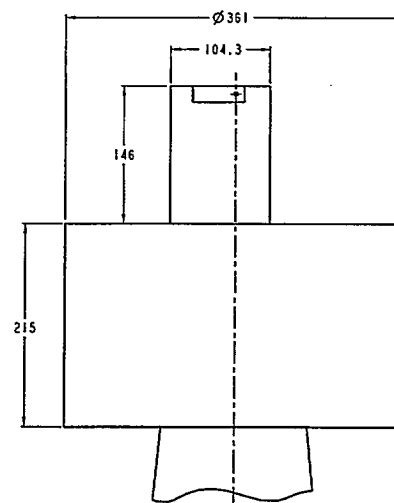
## Appendix D

### Drawings

This appendix presents the drawings for the transmitter, the simulated heads and the styrofoam assembly. Drawings FFPPM.1 to FFPPM.6 pertain to the first test whereas PP-01 to PP-17 pertain to the second test.



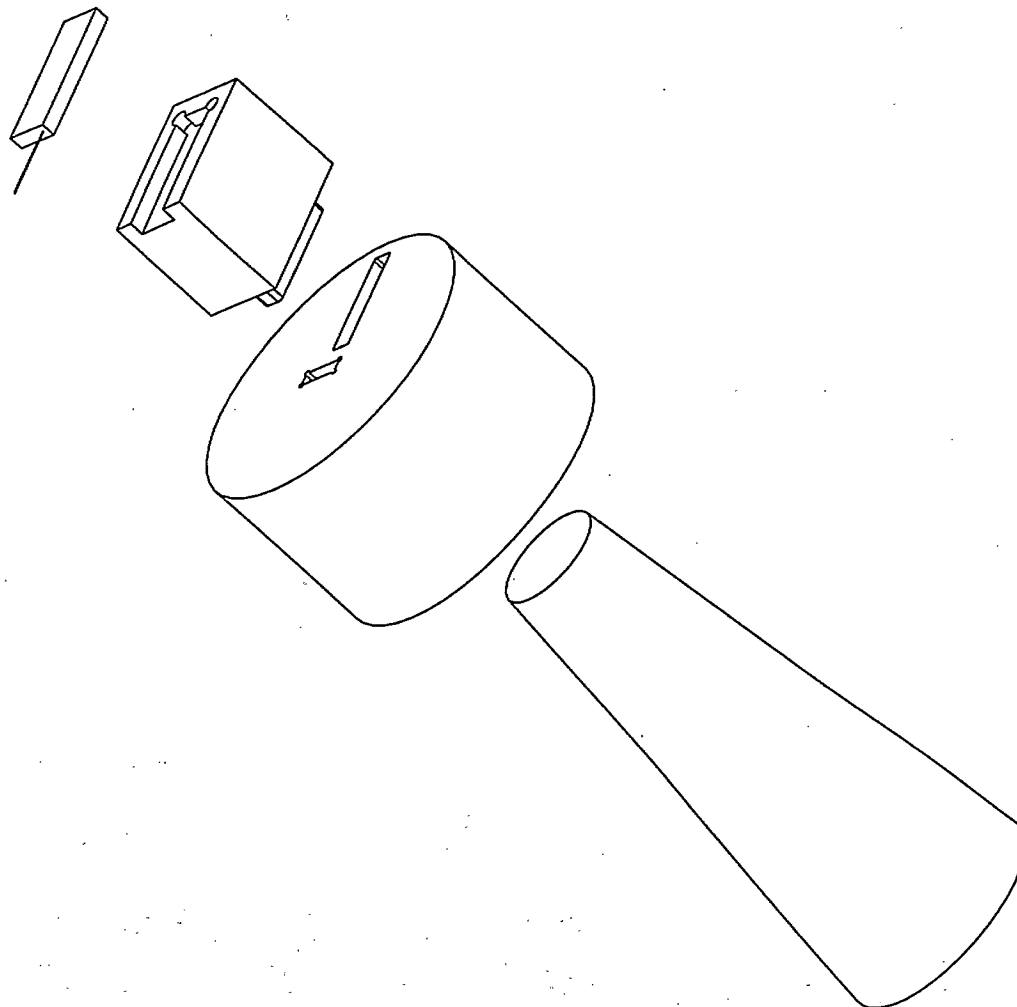
- STANO > 1000



FOR INTERNAL USE ONLY    POUR USAGE INTERNE SEULEMENT

DIMENSIONS IN MM		MATERIALS USED	
ALL TOLERANCES PER ISO 278		EN 8 - 1000	
WORK FILE		SACRIFICIAL	
WORKPIECE		90-001	
SCALE/REFERENCE	STROKE	MATERIAL	
0.500		EN 8 - 1000	
MATERIAL / MATERIAL		DATE	
STRENGTH		10-01-83	
FIGURE 2 / 10		DRAWN BY	
		9001 FILE	
		9001 FILE	





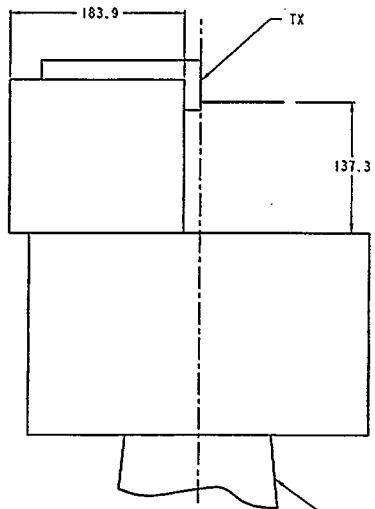
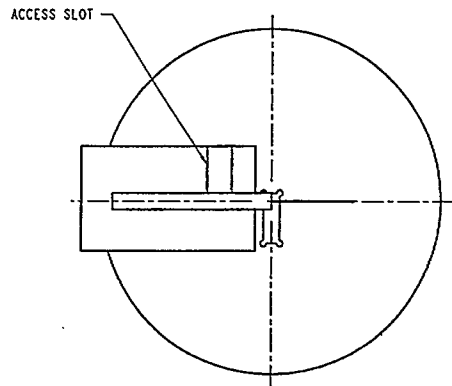
DO NOT REPRODUCE OR  
RE-TRANSMIT THIS MESSAGE

Eq.	MTT	MY. 2 3LY.	MTT LORD
-----	-----	------------	-------------

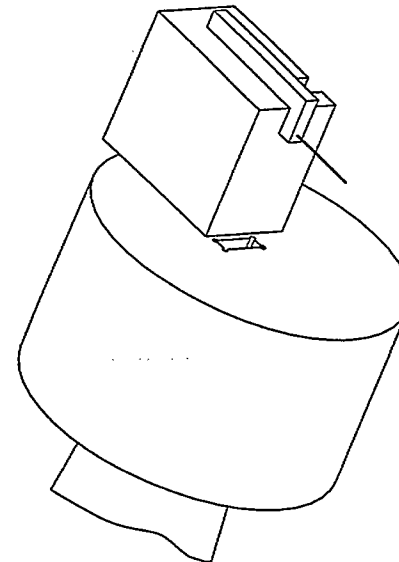
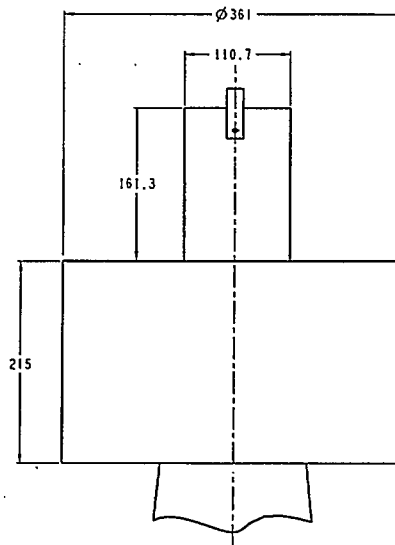
FOR INTERNAL USE ONLY POUR USAGE INTERNE SEULEMENT

DIMENSIONS IN MM ALL TOLERANCES PER CNC C10	DESIG-UNDESIG 83-000		RECD AT
WORK FILE NORTHPORT	SMOY/DAVIDS 07-000		
0.5mm/0.0001 0.01mm/0.001 0.5mm	DIM. PRECISE 1.0 CLAMP		
MATERIAL: 303 STAINLESS STEEL	10-26-97 1045 FILE		
FINISH: 320	DIM. FILE 1045 FILE		
PROTOTYPE DESIGN		CONCEPTION DE PROTOTYPE	
FILED BY: BATH		FAR FIELD PRINCIPAL PLANE MOUNT	

FFPPM.3



- STAND > 1000



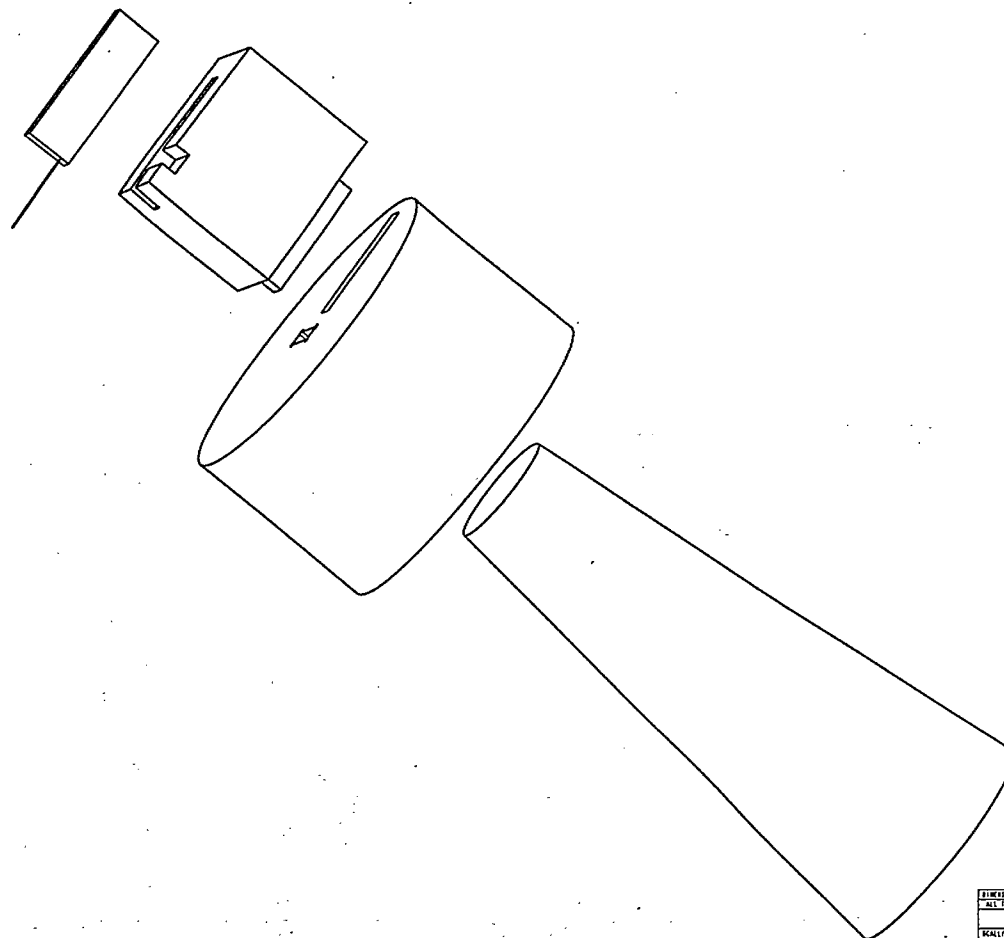
FOR INTERNAL USE ONLY    POUR USAGE INTERNE SEULEMENT

DIMENSIONS IN MM ALL DIMENSIONS PER CAD FILE	MOUNTING HOLE 37-001		PROTOTYPE DESIGN    CONCEPTION DE PROTOTYPE	STYLE / STYLE	FAR FIELD PRINCIPAL PLANE MOUNT	SERIAL 0 AT
MODEL FILE VERTICAL	ISO/PARTICLE 65-001					
SCALE/FIELD OF VIEW 0.5MM	OPT. POSITION, P-FILE					
MATERIAL / MATERIAL STYRENE	WAVE 65-001-001					
FOCUS / FOC	1MM FILE 1MM FILE					

DO NOT MEASURE PLANNING  
WE CAN MEASURE LEARNING

No.	DATE	REV. & ETC.	BY
-----	------	-------------	----

FFPPM.4




NE PAS MESURER LES MESURES  
NE PAS MESURER LES MESURES

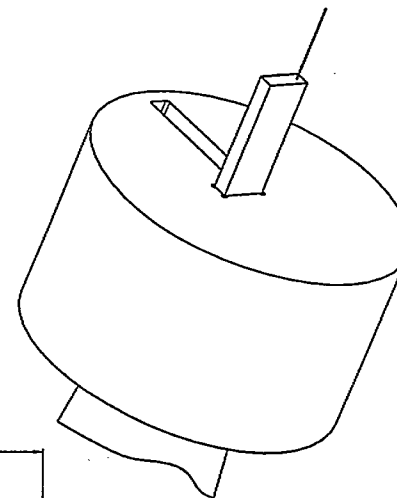
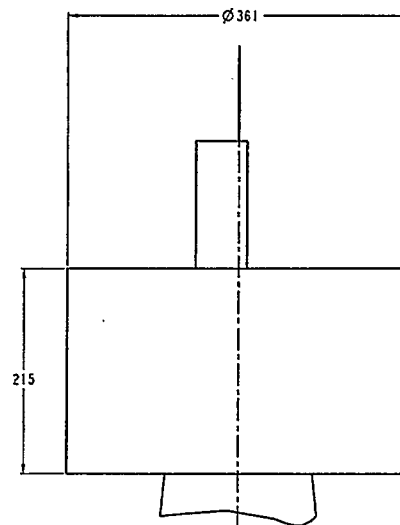
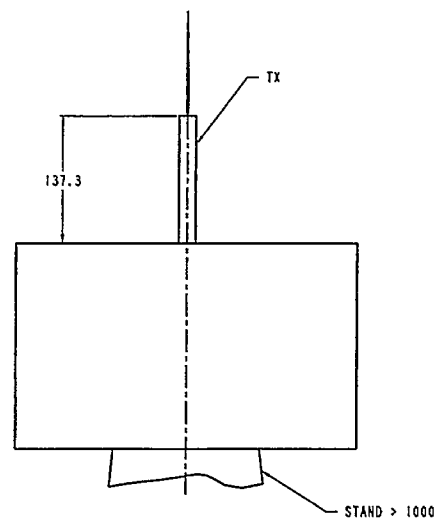
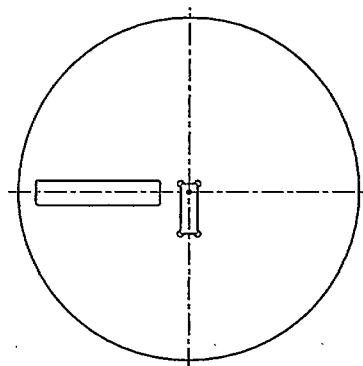
REV.	DATE	REV. / REV.	APPR. / APPROV.

DESCRIPTION IN ALL DIMENSIONS PER CMC 310	REVISIONS
MODEL FILE VERSION	NO. / NO.
SCALE/ECHELLE 1:100	DATE
MATERIAL / MATÉRIEL	DATE
	DATE
	DATE

FOR INTERNAL USE ONLY POUR USAGE INTERNE SEULEMENT

	
PROTOTYPE DESIGN	CONCEPTION DE PROTOTYPE
FAR FIELD PRINCIPAL PLANE MOUNT	
REV.	AT
0	

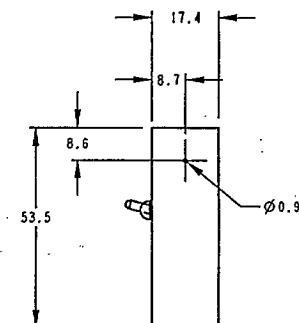
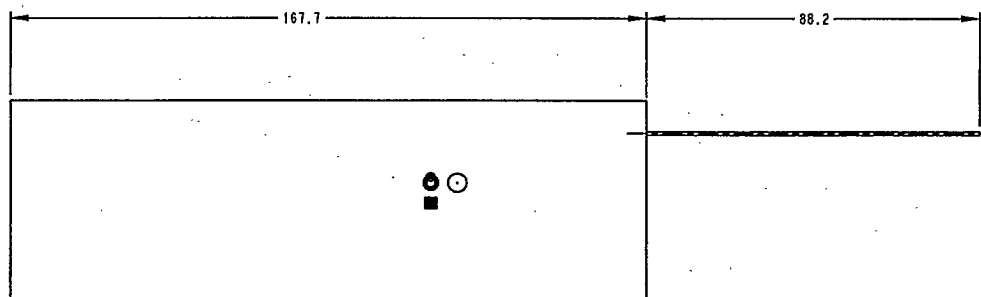
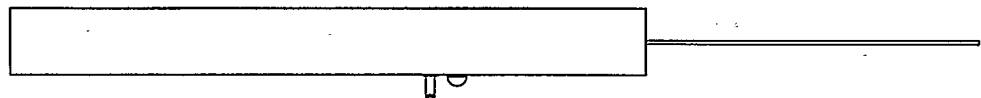
FFPPM.5



FOR INTERNAL USE ONLY    POUR USAGE INTERNE SEULEMENT

[illegible]

FFPPM.6



FOR INTERNAL USE ONLY POUR USAGE INTERNE SEULEMENT

DIMENSIONS IN	MM	DESIGN/DESSIN
ALL TOLERANCES PER CRC STD		
MODEL FILE		SHOP/ATELIER
TX		
SCALE/ECHELLE	QTY/OTE	DWN./DESSIN.
1:1	1	
MATERIAL / MATERIEL		DATE
6061-T6 ALUMINUM		
FINISH / FIN.		IGES FILE
NATURAL		DWG FILE
		97130_A301

PROTOTYPE DESIGN CONCEPTION DE PROTOTYPE

TITLE / TITRE

TX

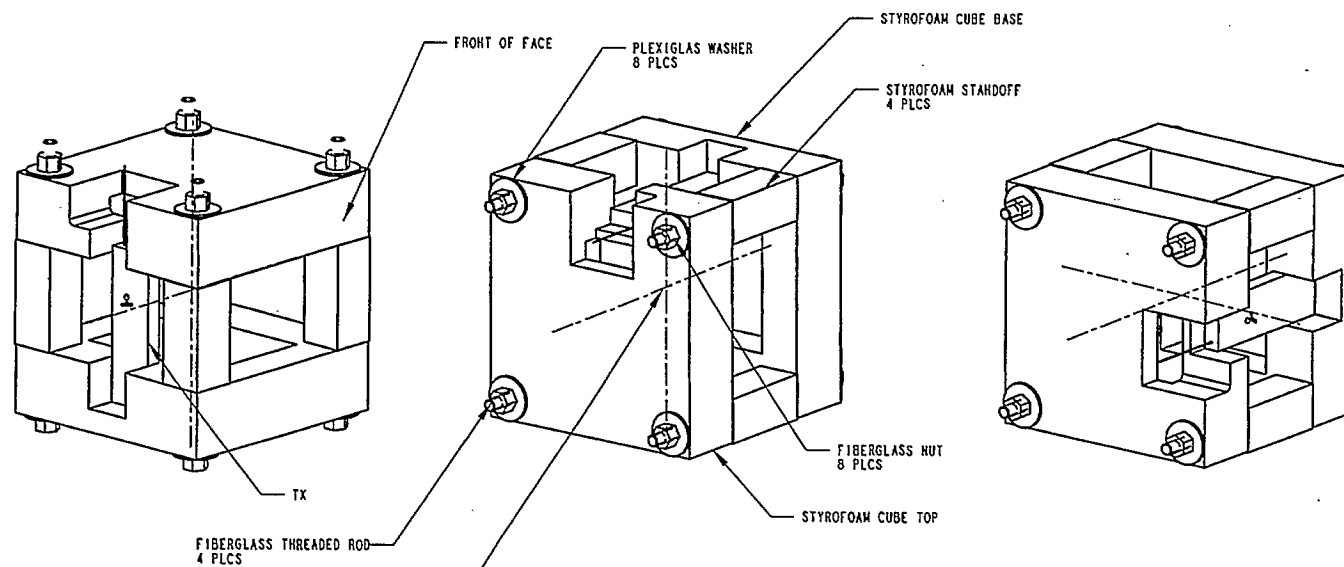
REV.
1
A3

DO NOT MEASURE DRAWING  
NE PAS MESURER LE DESSIN

I	DS/12/97	TITLE CHANGED
No.	DATE	REV. / REV.

APPVL.  
APPROB.

NATURAL



FOR INTERNAL USE ONLY POUR USAGE INTERNE SEULEMENT

DIMENSIONS IN	MM	DESIGN/DESSIN
ALL TOLERANCES PER CRC STD		97-130
MODEL FILE		SHOP/ATELIER
PP_STANDOFF		97-130
SCALE/ECHELLE	QTY/OTE	DWN./DESSIN
0.250		P. CLARK
MATERIAL / MATERIEL		DATE
		13-Aug-97
		IGES FILE
		DWG FILE
		97130_A302
FINISH / FIN.		

**CRC**

PROTOTYPE DESIGN CONCEPTION DE PROTOTYPE

TITLE / TITRE

PRINCIPAL PLANE WITH TX ONLY

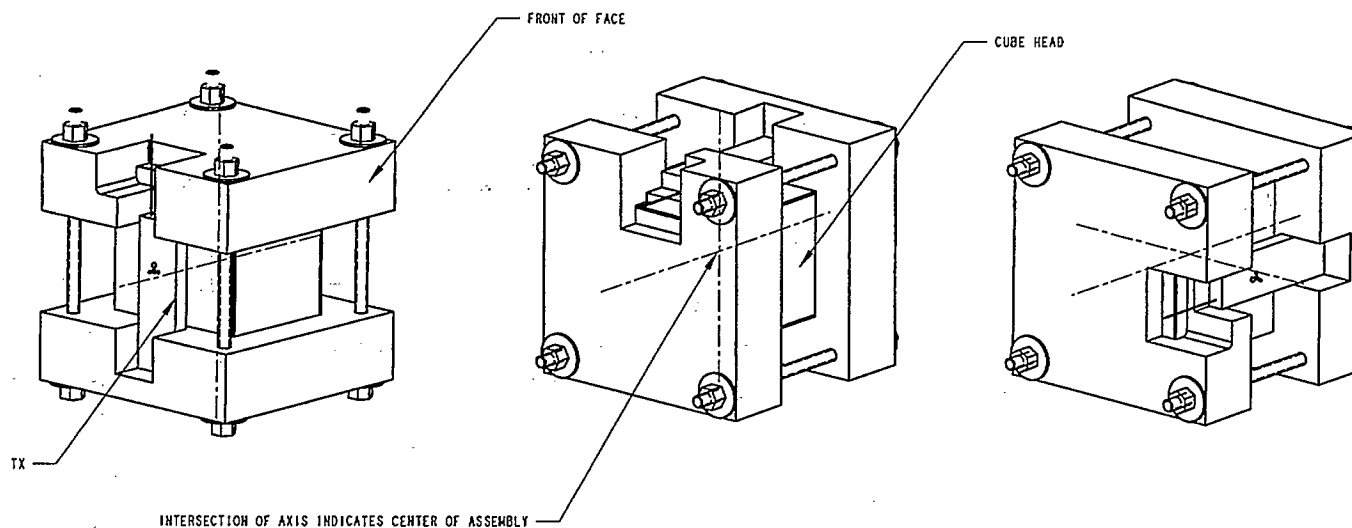
REV.	1
	A3

DO NOT MEASURE DRAWING  
NE PAS MESURER LE DESSIN

1	05/12/97	CHANGES TO NOTES	
No.	DATE	REV. / REV.	APPVL. APPROB.



PP-02



FOR INTERNAL USE ONLY    POUR USAGE INTERNE SEULEMENT

DIMENSIONS IN	MM	DESIGN/DESSIN
ALL TOLERANCES PER CRC STD		
MODEL FILE	PP_STANDOFF	SHOP/ATELIER
SCALE/ECHELLE	0.250	QTY/OTE
DWN./DESSIN		
MATERIAL / MATERIEL		DATE
		13-Aug-97
		IGES FILE
		DWG FILE
		97130_A302
FINISH / FIN.		



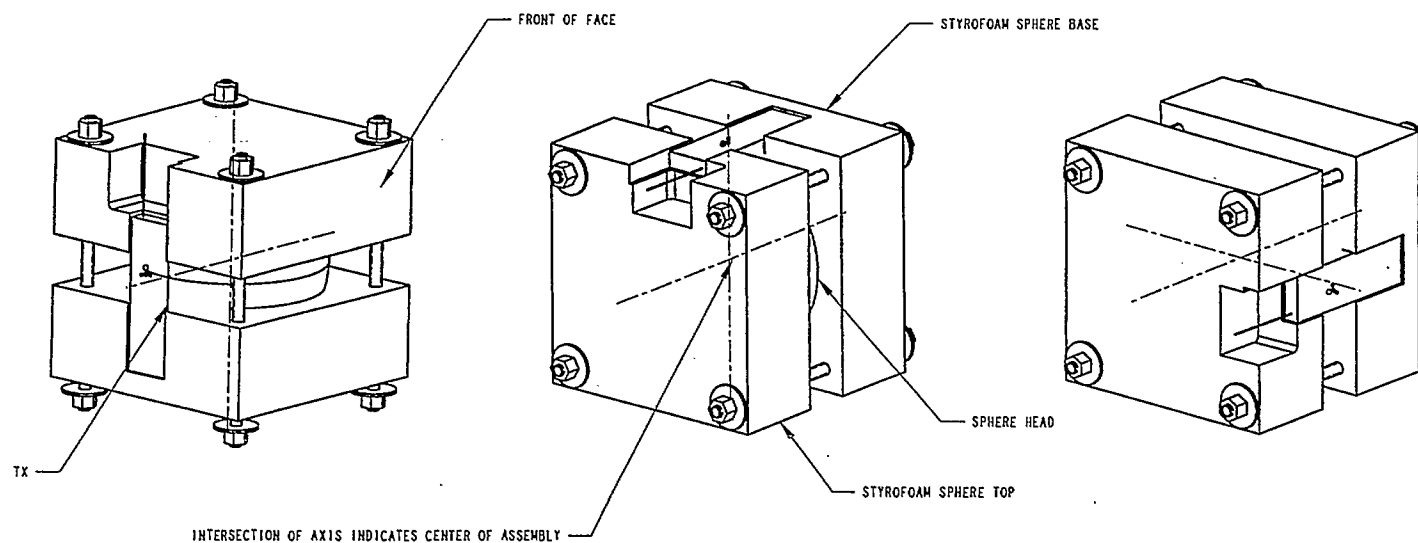
PROTOTYPE DESIGN    CONCEPTION DE PROTOTYPE

TITLE / TITRE	REV.
PRINCIPAL PLANE WITH CUBE HEAD MODEL AND TX	1
	A3

DO NOT MEASURE DRAWING  
NE PAS MESURER LE DESSIN


05/12/97	CHANGES TO NOTES	
No.	DATE	REV. / REV.
		APPVL. APPROB.

PP-03



FOR INTERNAL USE ONLY    POUR USAGE INTERNE SEULEMENT

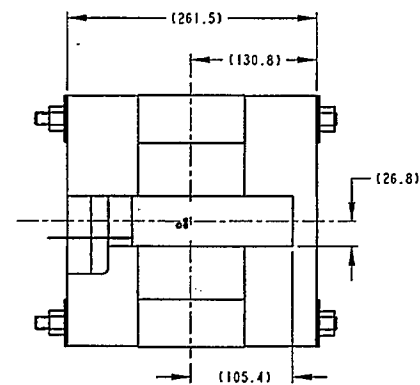
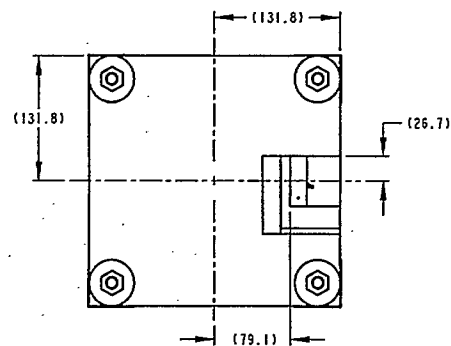
DIMENSIONS IN	MM	DESIGN/DESSIN
ALL TOLERANCES PER CRC STD		
MODEL FILE	PP_CUBE	SHOP/ATELIER
SCALE/ECHELLE	1.000	QTY/QTE
MATERIAL / MATERIEL		DATE
		13-Aug-97
		IGES FILE
		DWG FILE
		97130_A302
FINISH / FIN.		

		REV.
PROTOTYPE DESIGN    CONCEPTION DE PROTOTYPE		1
TITLE / TITRE		A3
PRINCIPAL PLANE WITH SPHERE HEAD MODEL AND TX		

DO NOT MEASURE DRAWING  
NE PAS MESURER LE DESSIN

1	05/12/97	CHANGES TO NOTES	
No.	DATE	REV. / REV.	APPVL. APPROB.

PP-04



FOR INTERNAL USE ONLY POUR USAGE INTERNE SEULEMENT

DIMENSIONS IN MM	DESIGN/DESSIN
ALL TOLERANCES PER CRC STD	MODEL FILE
PP_STANDOFF	SHOP/ATELIER
SCALE/ECHELLE	QTY/OTE
0.250	DWN./DESSIN
MATERIAL / MATERIEL	DATE
	14-Aug-97
	IGES FILE
FINISH / FIN.	DWG FILE
	97130_A3D2

PROTOTYPE DESIGN CONCEPTION DE PROTOTYPE

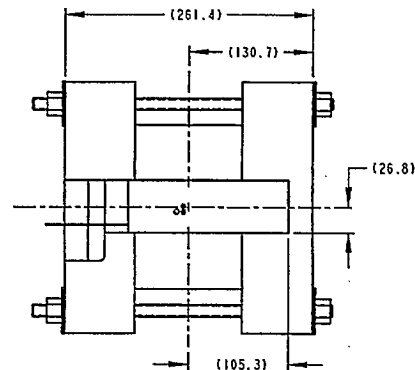
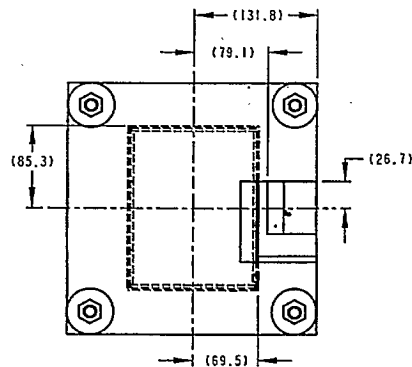
TITLE / TITRE

PRINCIPAL PLANE WITH TX ONLY  
CENTER LOCATION


REV.	1
	A3

DO NOT MEASURE DRAWING  
NE PAS MESURER LE DESSIN

No.	DATE	REV. / REV.	APPVL. APPROB.

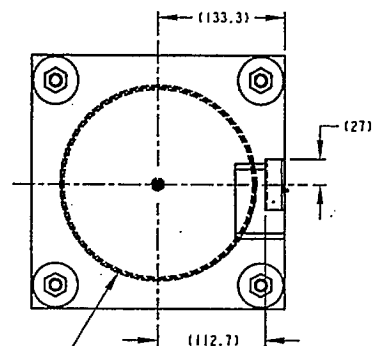


FOR INTERNAL USE ONLY POUR USAGE INTERNE SEULEMENT

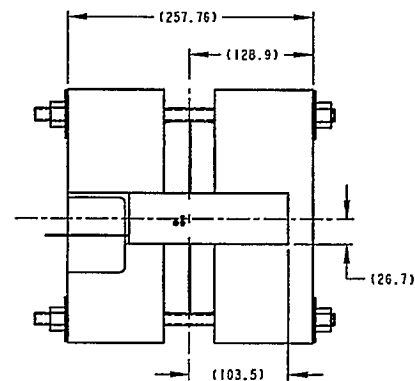
DIMENSIONS IN MM		DESIGN/DESSIN	
ALL TOLERANCES PER CRC STD		SHOP/ATELIER	
MODEL FILE PP_SPHERE		DWN./DESSIN.	
SCALE/ECHELLE 1.000	QTY/QTE	DATE 14-Aug-97	
MATERIAL / MATERIEL		IGES FILE	TITLE / TITRE
FINISH / FIN.		DWG FILE 9713D_A302	PROTOTYPE DESIGN CONCEPTION DE PROTOTYPE PRINCIPAL PLANE WITH CUBE HEAD MODEL AND TX, CENTER LOCATION
No.	DATE	REV. / REV.	REV. 1 A3

DO NOT MEASURE DRAWING  
NE PAS MESURER LE DESSIN

PP-06



SPHERE HEAD WITH OUTSIDE RADIUS OF 103.4  
IS CENTERED IN ASSEMBLY



FOR INTERNAL USE ONLY POUR USAGE INTERNE SEULEMENT

DIMENSIONS IN MM	DESIGN/DESSIN
ALL TOLERANCES PER CRC STD	SHOP/ATELIER
MODEL FILE PP_CUBE	
SCALE/ECHELLE 1.000	QTY/OTE
MATERIAL / MATERIEL	DWN./DESSIN.
	DATE 14-Aug-97
	IGES FILE
FINISH / FIN.	DWG FILE 97130_A302



PROTOTYPE DESIGN CONCEPTION DE PROTOTYPE

TITLE / TITRE

PRINCIPAL PLANE WITH SPHERE HEAD  
MODEL AND TX, CENTER LOCATION

REV.

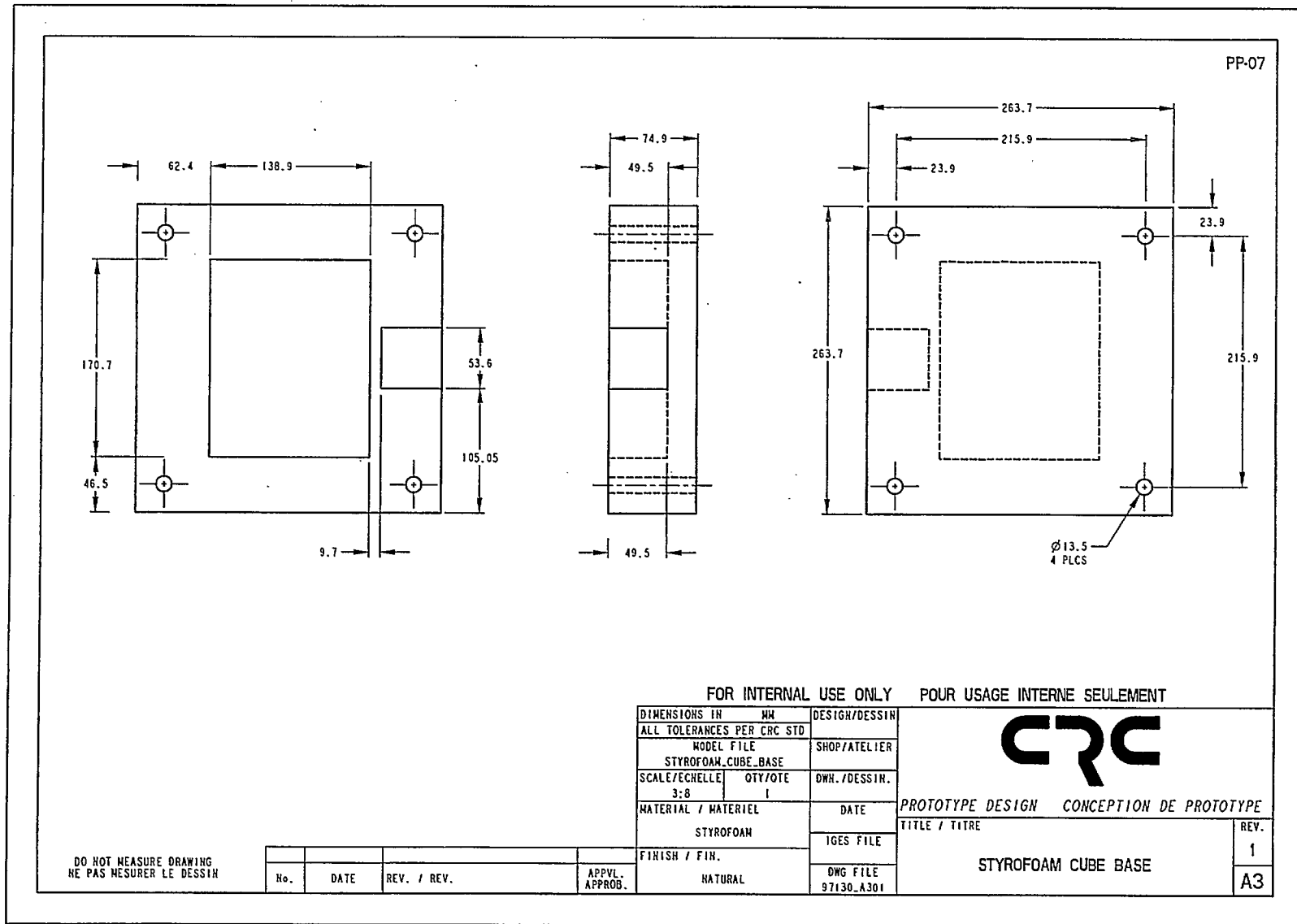
1

A3

DO NOT MEASURE DRAWING  
NE PAS MESURER LE DESSIN

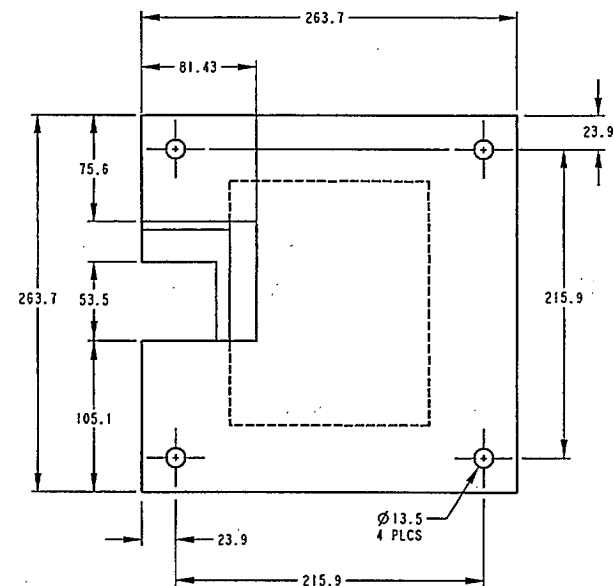
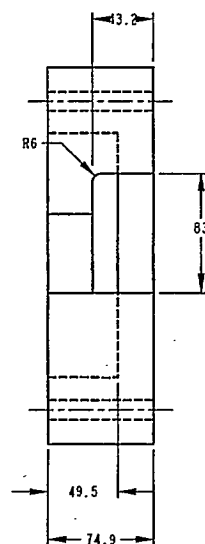
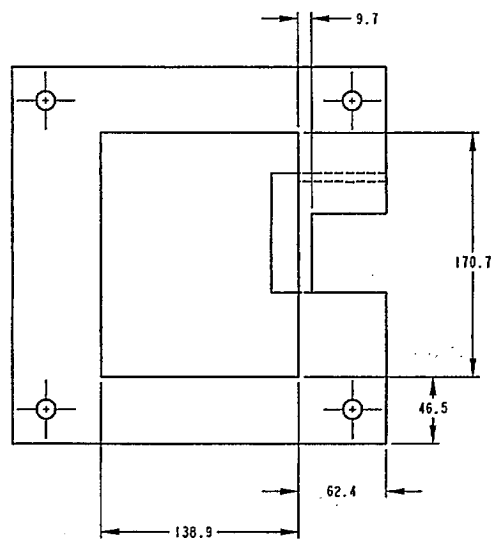
I	05/12/97	CHANGES TO NOTES
No.	DATE	REV. / REV.

APPVL.  
APPROB.





PP-08



DO NOT MEASURE DRAWING  
NE PAS MESURER LE DESSIN

No.	DATE	REV. / REV.	APPVL. APPROB.

FOR INTERNAL USE ONLY POUR USAGE INTERNE SEULEMENT

DIMENSIONS IN MM	DESIGN/DESSIN
ALL TOLERANCES PER CRC STD	SHOP/ATELIER
MODEL FILE STYROFOAM_CUBE.TOP	DWN./DESSIN.
SCALE/ECHELLE 3:8	DATE
QTY/OTE 1	IGES FILE
MATERIAL / MATERIEL STYROFOAM	DWG FILE 97130_A301
FINISH / FIN. NATURAL	

**CRC**

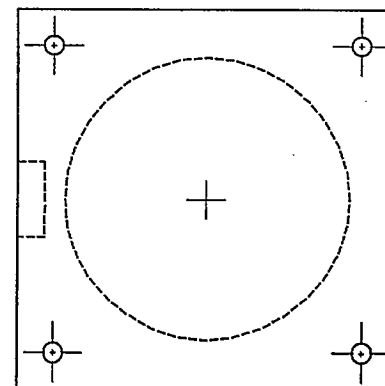
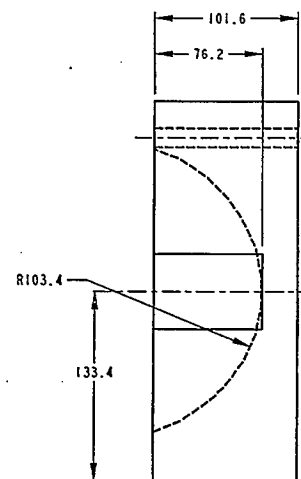
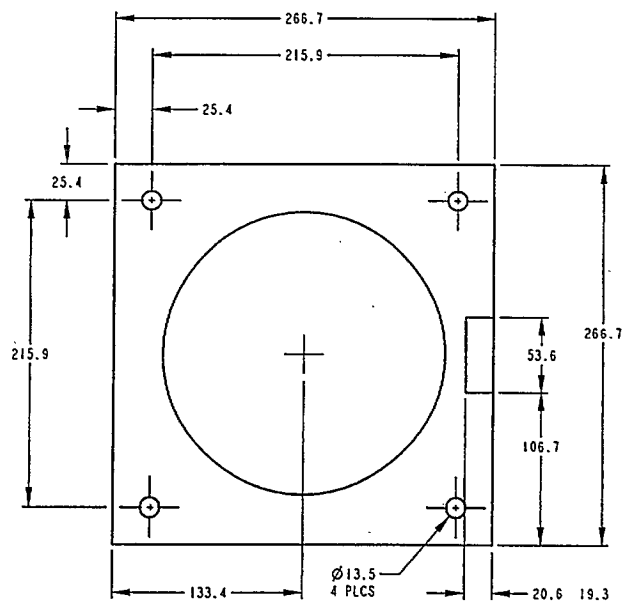
PROTOTYPE DESIGN CONCEPTION DE PROTOTYPE

TITLE / TITRE

STYROFOAM CUBE TOP

REV.  
1  
A3

PP-09



FOR INTERNAL USE ONLY POUR USAGE INTERNE SEULEMENT

DIMENSIONS IN	MM	DESIGN/DESSIN
ALL TOLERANCES PER CRC STD		SHOP/ATELIER
MODEL FILE		DWN./DESSIN.
STYROFOAM_SPHERE_BASE		
SCALE/ECHELLE	QTY/OTE	DATE
3:8	1	
MATERIAL / MATERIEL		IGES FILE
STYROFOAM		
FINISH / FIN.		DWG FILE
NATURAL		96364-03A3

PROTOTYPE DESIGN CONCEPTION DE PROTOTYPE

TITLE / TITRE

STYROFOAM SPHERE BASE

REV.

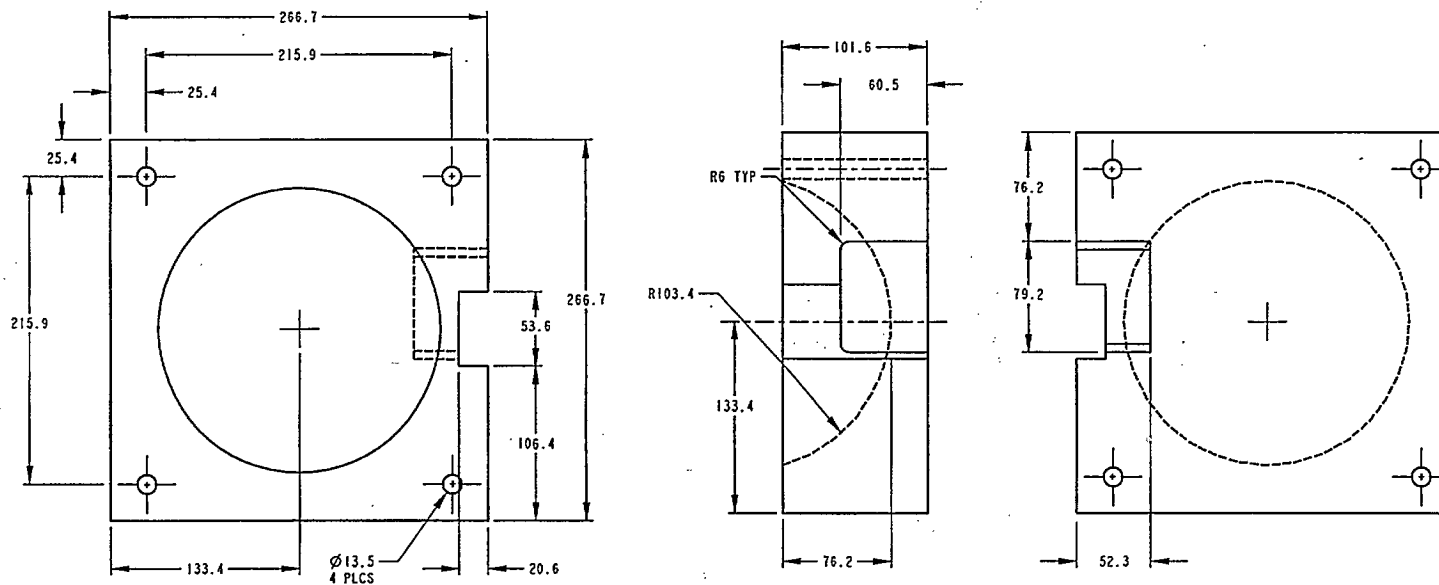
1

A3

DO NOT MEASURE DRAWING  
NE PAS MESURER LE DESSIN


No.	DATE	REV. / REV.	APPVL. APPROB.

PP-10



FOR INTERNAL USE ONLY POUR USAGE INTERNE SEULEMENT

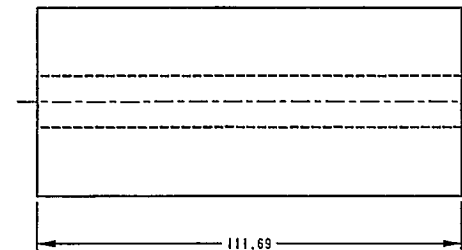
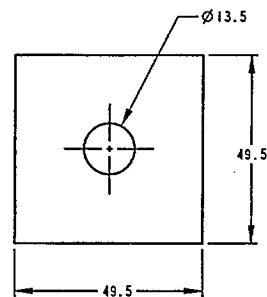
DIMENSIONS IN MM		DESIGN/DESSIN
ALL TOLERANCES PER CRC STD		
MODEL FILE		SHOP/ATELIER
STYROFOAM_SPHERE_TOP		
SCALE/ECHELLE	QTY/QTE	DWN./DESSIN
3:8	1	
MATERIAL / MATERIEL		DATE
STYROFOAM		
FINISH / FIN.		IGES FILE
NATURAL		
		DWG FILE
		96364-03A3

		<b>PROTOTYPE DESIGN CONCEPTION DE PROTOTYPE</b>	
		TITLE / TITRE	REV.
STYROFOAM SPHERE TOP			1
			A3

DO NOT MEASURE DRAWING  
NE PAS MESURER LE DESSIN

No.	DATE	REV. / REV.	APPR. / APPROB.

PP-11



FOR INTERNAL USE ONLY POUR USAGE INTERNE SEULEMENT

DIMENSIONS IN	MM	DESIGN/DESSIN
ALL TOLERANCES PER CRC STD		
MODEL FILE		SNOP/ATELIER
STYROFOAM_CUBE_STANDOFF		
SCALE/ECHELLE	QTY/OTE	DWN./DESSIN.
1:1	4	
MATERIAL / MATERIEL		DATE
STYROFOAM		
FINISH / FIN.		IGES FILE
NATURAL		
		DWG FILE
		97130_A301



PROTOTYPE DESIGN CONCEPTION DE PROTOTYPE

TITLE / TITRE

STYROFOAM CUBE STANDOFF

REV.

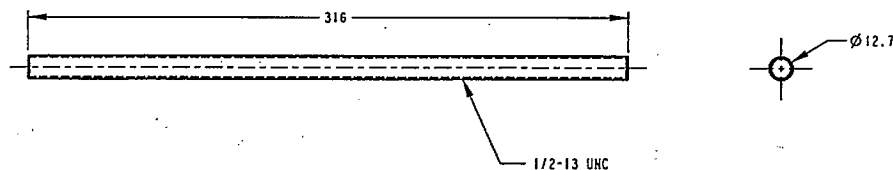
1

A3

DO NOT MEASURE DRAWING  
NE PAS MESURER LE DESSIN

1	05/12/97	PP-12 CHANGED TO PP-11	
No.	DATE	REV. / REV.	APPVL. APPROB.

PP-12



FOR INTERNAL USE ONLY · POUR USAGE INTERNE SEULEMENT

DIMENSIONS IN	MM	DESIGN/DESSIN
ALL TOLERANCES PER CRC STD		
MODEL FILE		SHOP/ATELIER
FIBREBOLT_STUD_300		
SCALE/ECHELLE	QTY/QTE	DWN./DESSIN
1:2		
MATERIAL / MATERIEL	DATE	
FIBERGLASS AND VINYL ESTER RESIN	13-Aug-97	
	IGES FILE	
FINISH / FIN.	OWG FILE	
	97130_A301	

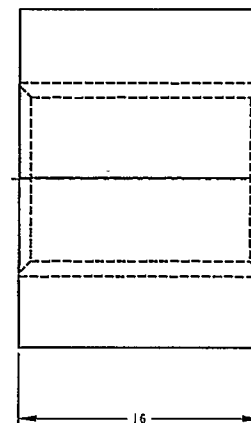
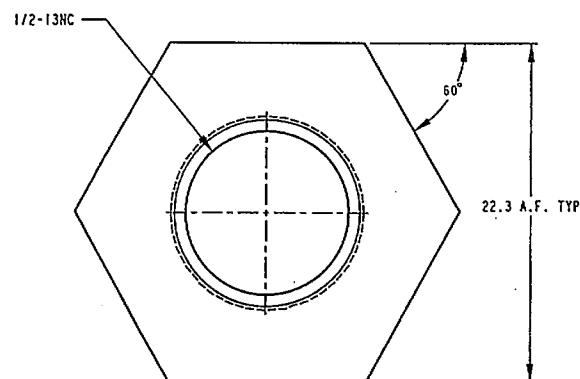
PROTOTYPE DESIGN · CONCEPTION DE PROTOTYPE

TITLE / TITRE	REV.
FIBERGLASS THREADED ROD	1
	A3

DO NOT MEASURE DRAWING  
NE PAS MESURER LE DESSIN

I	05/12/97	PP-11 CHANGED TO PP-12
No.	DATE	REV. / REV.

APPVL.  
APPROB.



FOR INTERNAL USE ONLY POUR USAGE INTERNE SEULEMENT

DIMENSIONS IN MM	DESIGN/DESSIN
ALL TOLERANCES PER CRC STD	SNOP/ATELIER
MODEL FILE FIBREBOLT_NUT	DWN./DESSIN.
SCALE/ECHELLE 4:1	DATE
QTY/OTE 8	IGES FILE
MATERIAL / MATERIEL FIBERGLASS AND VINYL ESTER RESIN	DWG FILE 97130_A301
FINISH / FIN. NATURAL	

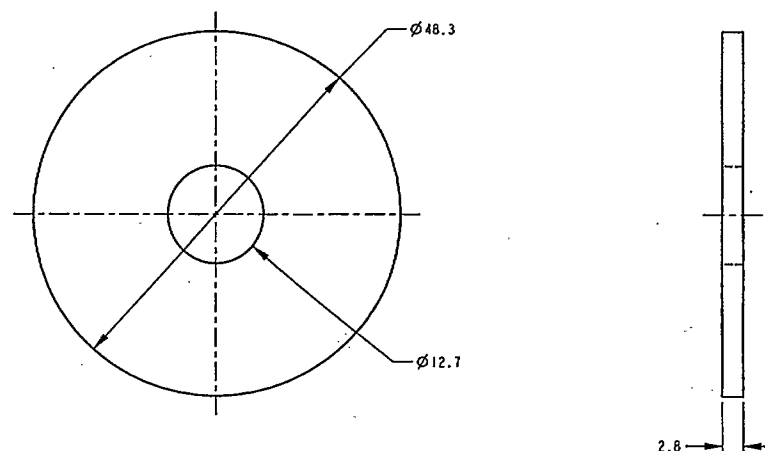


PROTOTYPE DESIGN	CONCEPTION DE PROTOTYPE	REV. 1
TITLE / TITRE FIBERGLASS NUT		A3

DO NOT MEASURE DRAWING  
NE PAS MESURER LE DESSIN

1	05/12/97	TITLE CHANGED	
No.	DATE	REV. / REV.	APPVL. APPROB.

PP-14



FOR INTERNAL USE ONLY POUR USAGE INTERNE SEULEMENT

DIMENSIONS IN	MM	DESIGN/DESSIN
ALL TOLERANCES PER CRC STD		
MODEL FILE		SHOP/ATELIER
PLEXIGLASS WASHER		
SCALE/ECHELLE	QTY/OTE	DWN./DESSIN.
2:1	4	
MATERIAL / MATERIEL		DATE
WHITE ACRYLIC SHEET "PLEXIGLASS MC"		
FINISH / FIN.		IGES FILE
NATURAL		
		DWG FILE
		97130_A301

PROTOTYPE DESIGN CONCEPTION DE PROTOTYPE

TITLE / TITRE

REV.

1

PLEXIGLAS WASHER

A3

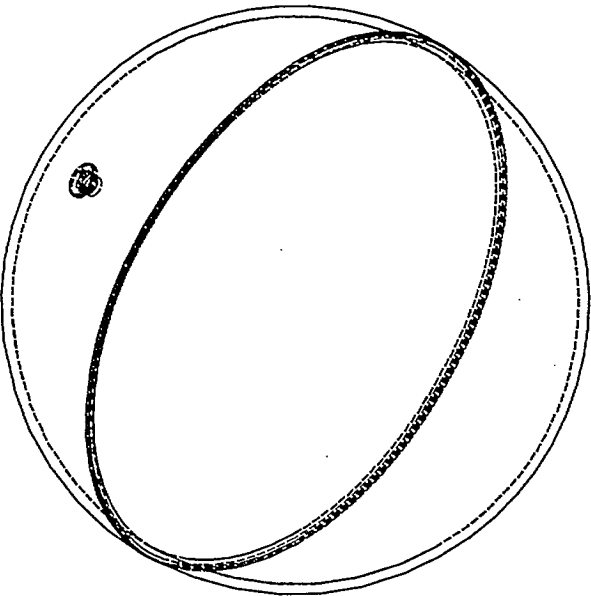
DO NOT MEASURE DRAWING  
NE PAS MESURER LE DESSIN

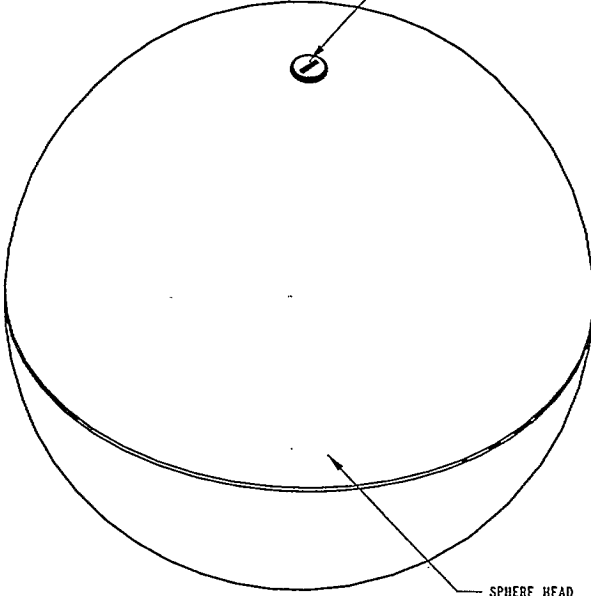
1"	DS/12/97	TITLE CHANGED
No.	DATE	REV. / REV.

APPVL.  
APPROB.

NATURAL








SPHERE PLUG  
MATL: ACETAL (1" DELRIN\*)

SPHERE HEAD  
206.8 O.D. x 199.5 I.D.

DO NOT MEASURE DRAWING  
NE PAS MESURER LE DESSIN

FOR INTERNAL USE ONLY    POUR USAGE INTERNE SEULEMENT

DIMENSIONS IN MM		DESIGN/DESSIN	
ALL TOLERANCES PER CRC STD		SHOP/ATELIER	
MODEL FILE SPHERE		DWN./DESSIN.	
SCALE/ECHELLE 3:4	QTY/OTE 1	DATE	
MATERIAL / MATERIEL CLEAR ACRYLIC SHEET "PLEXIGLASS FF"		IGES FILE	
FINISH / FIN. NATURAL		DWG FILE 96364-03A3	



PROTOTYPE DESIGN    CONCEPTION DE PROTOTYPE

TITLE / TITRE

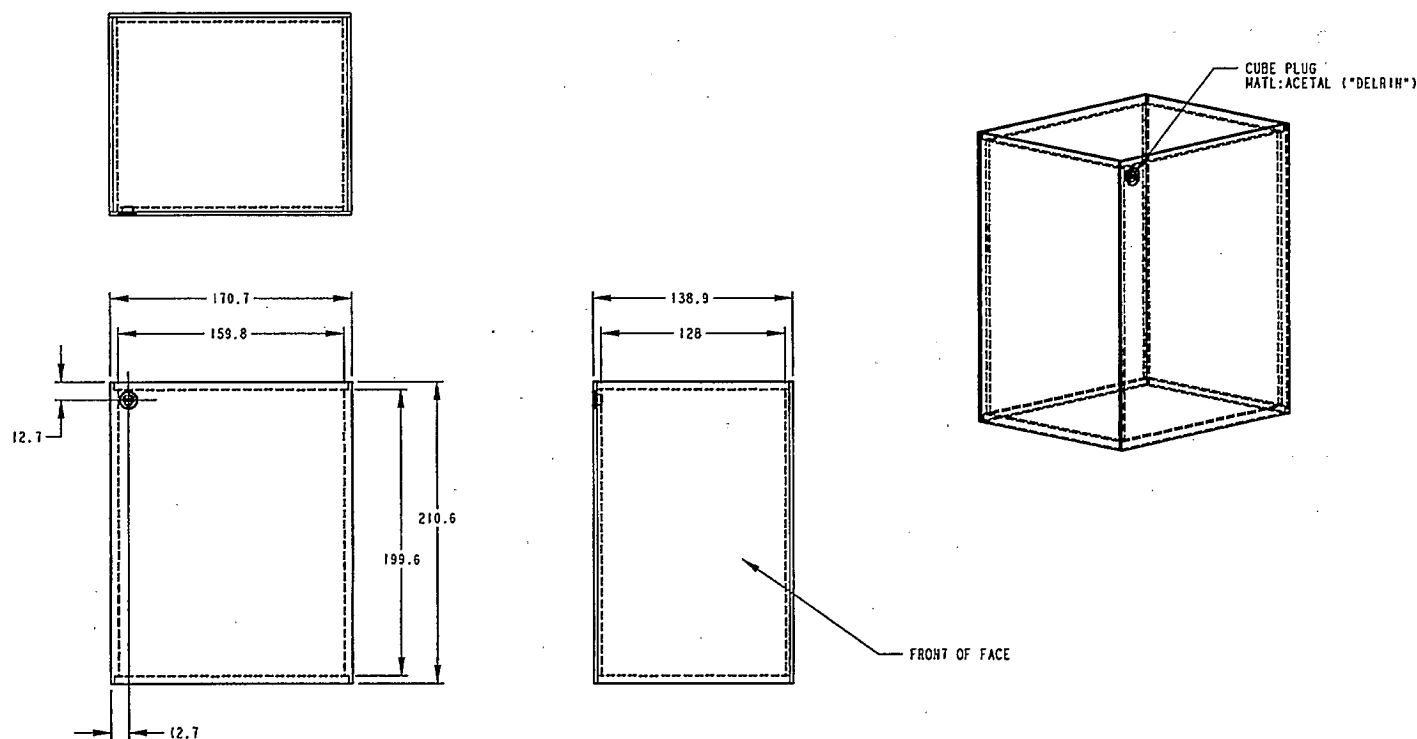
SPHERE HEAD

1	05/12/97	NOTE AND TITLE CHANGED	
No.	DATE	REV. / REV.	APPVL. APPROB.

A3

REV. 1

PP-16



FOR INTERNAL USE ONLY POUR USAGE INTERNE SEULEMENT

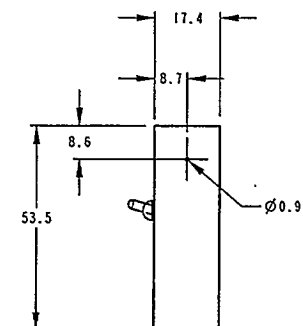
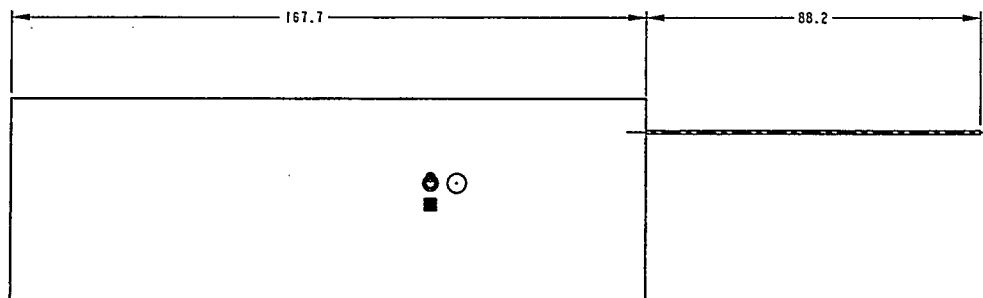
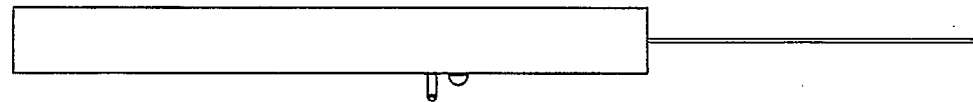
DIMENSIONS IN	MM	DESIGN/DESSIN
ALL TOLERANCES PER CRC STD		
MODEL FILE	CUBE	SHOP/ATELIER
SCALE/ECHELLE	QTY/OTE	DWN./DESSIN.
3:8	1	
MATERIAL / MATERIEL		DATE
CLEAR ACRYLIC SHEET		
"PLEXIGLASS 6"		
FINISH / FIN.		IGES FILE
NATURAL		
		DWG FILE
		96364-02A3

DO NOT MEASURE DRAWING  
NE PAS MESURER LE DESSIN

No.	DATE	REV. / REV.	APPVL. APPROB.
1	05/12/97	NOTE ADDED, TITLE CHANGED	

<b>CRC</b>		REV.
PROTOTYPE DESIGN CONCEPTION DE PROTOTYPE		1
TITLE / TITRE		A3
CUBE HEAD		

PP-17



FOR INTERNAL USE ONLY POUR USAGE INTERNE SEULEMENT

DIMENSIONS IN	MM	DESIGN/DESSIN
ALL TOLERANCES PER CRC STD		
MODEL FILE		SHOP/ATELIER
TX		
SCALE/ECHELLE	QTY/OTE	DWN./DESSIN.
1:1	1	
MATERIAL / MATERIEL		DATE
6061-T6 ALUMINUM		
FINISH / FIN.		IGES FILE
NATURAL		
		DWG FILE
		97130_A301

PROTOTYPE DESIGN	CONCEPTION DE PROTOTYPE
TITLE / TITRE	
TX	
REV.	1
	A3

DO NOT MEASURE DRAWING  
NE PAS MESURER LE DESSIN

I	05/12/97	TITLE CHANGED	
No.	DATE	REV. / REV.	APPVL. APPROB.

Measurements of the  
electromagnetic far-fields  
produced by a portable  
transmitter (principal  
planes)

CARR M <sup>O</sup> LEAN	38-296

INDUSTRY CANADA / INDUSTRIE CANADA

208886

00035 0150

